Design and Physics of VCSELs for Emerging Applications

Jonas Horst Kapraun

Electrical Engineering and Computer Sciences
University of California, Berkeley

May 1, 2021

Acknowledgement

Design and Physics of VCSELs for Emerging Applications

By

Jonas Horst Kapraun

A dissertation submitted in partial satisfaction of the

requirements for the degree of

Doctor of Philosophy

in

Engineering – Electrical Engineering and Computer Sciences

in the

Graduate Division

of the

University of California, Berkeley

Committee in charge:

Professor Constance Chang-Hasnain
Professor Eli Yablonovitch
Professor Liwei Lin

Spring 2019

Design and Physics of VCSELs for Emerging Applications

By

Jonas Kapraun

Abstract

Design and Physics of VCSELs for Emerging Applications

by

Jonas Horst Kapraun

Doctor of Philosophy in Electrical Engineering and Computer Sciences

University of California, Berkeley

Professor Constance Chang-Hasnain, Chair

Vertical cavity surface emitting lasers (VCSELs) have been widely employed in short distance optical interconnects. Recently however a series of emerging applications are creating a rapidly growing demand for compact, low cost and high-performance light sources. 3D imaging and proximity sensing capabilities based on time of flight and structured light schemes are currently being deployed in a vast amount of consumer hand held devices, in particular in cell phones. Here VCSEL arrays of various sizes, densities and powers are being employed in volumes of multiple hundreds of millions per year. At the same time, wavelength tunable VCSELs with wide tuning range, fast tuning speed and single mode continues wavelength tuning are of tremendous interest for swept source optical coherence tomography (SS-OCT).

This work investigates a series of VCSEL architectures that specifically address the requirements of the above-mentioned applications. Inhouse epitaxial growth by metal organic chemical vapor deposition was developed (chapter 2) to supply the wide variety of VCSEL structures investigated and in particular to enable the realization of devices that depend on regrowth steps. Optical pumping of high contrast grating (HCG) enabled devices was tested (chapter 3) as this method has proven successful in DBR based devices. Wavelength tunable VCSELs with a MEMS actuated HCG as sole top reflector where demonstrated (chapter 4 & 5). These devices showed single mode emission and continues electrostatic tuning covering a wide wavelength range. Thus, proving their concepts promising for application as sources in SS-OCT. Two different VCSEL architectures with lithographically defined current apertures have been investigated, one based on a buried InGaP heterostructure (chapter 5) and one based on a buried tunnel junction (chapter 6). Substituting the native oxide confined current aperture by a lithographic aperture of such kind enables a wealth of potential performance improvements. Improvements in reliability, thermal resistance, emitter uniformity, array density, high-power single mode emission and coherently coupled arrays can be reasonably expected of such devices. In combination with the HCG reflector lasing in a stable, single polarization can be achieved. At last, VCSEL arrays were fabricated at 850 nm and 940 nm wavelength in chapter 7.

1

To my family

and my colleagues

for the tremendous support

and the countless opportunities to learn.

Table of Contents

Table of Figures

5

8

9

Acknowledgements

1 Introduction to VCSELs

Vertical cavity surface emitting lasers (VCSELs) are semiconductor lasers with surface normal lasing emission of a few milliwatts to tens of milliwatts of optical power for a single emitter and watts of optical power for 2-dimensional arrays of devices with many hundreds to thousands of emitter elements. Devices have been realized in the UV and visible wavelength ranges and are widely commercialized in the near and mid IR wavelength range for a variety of applications. III-V Semiconductor materials used to realize VCSELs include the nitride and antimonide material systems, but devices based on indium phosphide and gallium arsenide dominate the market space. This work follows the trend and focuses on devices based on the gallium arsenide material system emitting at wavelength around 850 nm, 940 nm, 980 nm and 1060 nm. This chapter provides a brief and general introduction to the VCSEL. The first section will describe the structure of a device, discuss the processes to realize a VCSEL and some unique properties. The second section mentions a number of important applications in which NIR IR VCSELs are applied.

1.1 Principle

The process to realize VCSEL devices can be divided in three main parts: (1) Growth of epitaxial layers by metal organic chemical vapor deposition (MOCVD) which defines the vertical structure of the devices, (2) Microfabrication processes including lithography, etching, metal evaporation and other steps which define the lateral structure and contacts of the devices and (3) packaging procedures, such as wafer dicing, die attach and wire bonding which integrate the VCSEL chips electrically, optically, mechanically and thermally with a system. Fig. 1.1 (a) shows a cross sectional schematic of the epitaxial structure of a generic oxide confined VCSEL device. The growth of VCSEL starts with a n-doped GaAs wafer. First a n-doped bottom reflector is grown which consists out of many pairs of $\lambda/4$ thick layers of materials with alternating refractive index referred to as distributed Bragg reflector (DBR). GaAs or low aluminum content AlGaAs and AlAs or high aluminum content AlGaAs are commonly used as layers with high and low refractive index respectively. An active region with several quantum wells embedded in AlGaAs cladding layers forms the center of the VCSEL structure. Within the quantum wells electrons and holes recombine radiatively and optical gain is provided to the laser at sufficiently high carrier densities. Close to the active region (here on top) a high aluminum AlGaAs layer (typically $Al_{98}GaAs$) is located. This layer is designed for selective oxidation in order to provide lateral confinement for electrical current and optical modes. The VCSEL structure is terminated by the p-doped top DBR and a highly p-doped contact layer, so that the entire structure resembles a p-i-n diode. After the MOCVD growth microfabrication is performed as shown for the generic VCSEL structure in Fig. 1.1 (b-d). First, mesas or trenches are defined by photolithography and subsequent etch as shown in (b). The purpose here is to expose the oxidizable high aluminum AlGaAs layer. This layer is transformed by a selective oxidation process with water vapor into a porous aluminum

oxide to define the laser aperture as shown in Fig. 1.1 (c). Finally, ohmic contacts are created. This is commonly done by evaporation of metal onto the p- and n-doped side of the VCSEL structure in combination with a lift-off process. The result is shown in Fig. 1.1 (d).
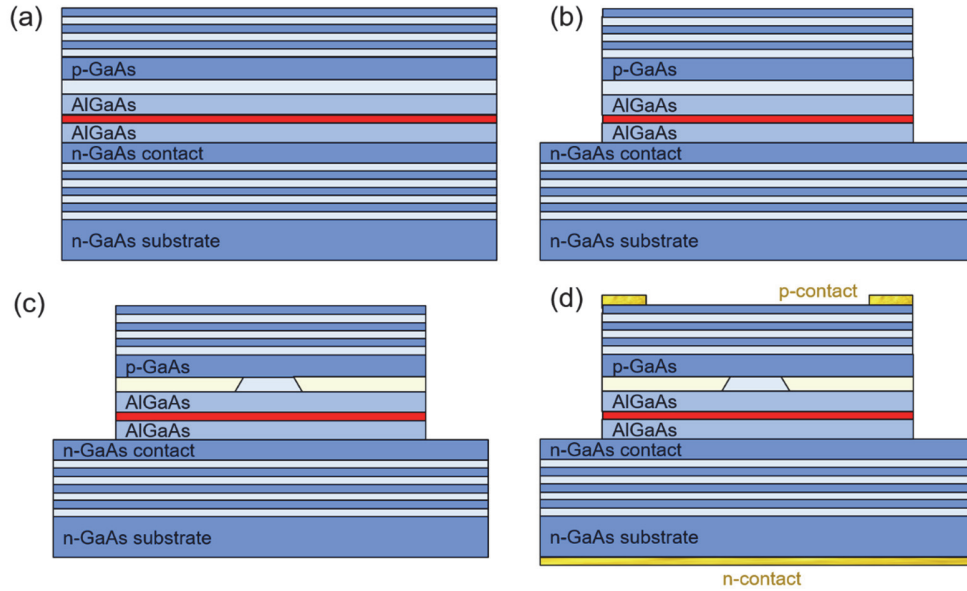
Fig. 1.1 Generic DBR VCSEL process. (a) Bottom DBR, MQW active region (red) and top reflector are grown by MOCVD. (b) Mesas are defined by photolithography and etch to insulate separate devices. (c) A high aluminum content AlGaAs layer is selectively oxidize to form the current confining aperture. (d) Finally, p- and n-metal contacts are evaporated.

After the microfabrication process is completed, the VCSEL devices can be tested on a wafer scale before they are packaged to integrate with a system. The processes involved depend on the application and system requirements, but common steps include dicing of the wafer into dies of individual VCSEL devices or groups of devices, attachment of these dies to heat sinking substrates, wire bonding to provide electrical connection and heat transfer between VCSEL chip and package and precision alignment of optical elements such as lenses, prisms and optical fibers with respect to the laser aperture for the optical integration of the device.

The described vertical emitting structure of the VCSEL presents several advantages compared to other semiconductor light sources such as LEDs and edge emitter lasers. Firstly, the optical cavity of the VCSEL is only a few multiple of the wavelength long. Therefore, a VCSEL typically emits in a single longitudinal mode that defines the lasing wavelength and the wavelength shift with changing temperatures. In contrast, the cavity length of a typical edge emitter laser is greater than 100 μm, thus its lasing emission is comprised of a multitude of closely spaced longitudinal modes and the temperature dependence of the emission wavelength is governed by the wavelength shift of the gain spectrum with temperature. As a result, the VCSEL has a superior stability of emission wavelength with changing temperature

[1]. The second advantage of the VCSEL is the circular beam shape and narrow divergence angle that results from a well-defined round shape of the current aperture. Employing a suitable design of current confining aperture and cavity structure single, transverse mode emission can be achieved. This results in a circular gaussian far field, ideal for both fiber coupling and free space applications. The far field of edge emitters is elliptical in shape, while the far field of LEDs is circular, but highly divergent. As a third advantage, the surface emitting geometry enables the monolithic integration of individual emitters to large 2-dimensional arrays to scale the output power while preserving a narrow emission spectrum and favorable beam characteristics. Finally, several economic considerations have contributed to the commercial success of VCSEL technology. Compared to the typical edge emitter lasers a VCSEL die requires a smaller footprint on the wafer. Additionally, vertical emitters can be tested on wafer scale after fabrication is complete, while edge emitting devices have to be diced before they can be tested. As a result, VCSELs have a clear cost advantage for applications requiring high device volumes.

1.2   Applications of VCSELs

This section will provide a brief exemplary overview of applications of VCSELs. As shown in Fig. 1.2 the majority of the application space of VCSELs is divided in two domains: (1) fiber based optical data communication and (2) optical sensing. In optical data communication directly modulated VCSELs are used for short distance optical communication predominantly in data centers. In wavelength division multiplexing (WDM) the signals of multiple emitters are coupled into a single fiber and wavelength tunable VCSELs are employed in a similar concept called dense wavelength division multiplexing. In response to the demand for ever higher data rates and volumes short wavelength division multiplexing (SWDM) in the wavelength range 840-950 nm is being developed recently [2].

For optical sensing single (transverse) mode and later polarization stabilized VCSELs have been employed in computer mice for several years. Recently however, the integration of VCSELs as light sources in 3D depth sensing schemes such as time of flight (TOF) and structured light have led to an explosion of the demand for VCSEL arrays consisting of a few to a few hundreds of emitters. While this market is currently focused on 3D sensing in cellphones, great prospects are seen in the application of VCSELs in similar sensing schemes for autonomous vehicles. Beyond this, widely wavelength tunable VCSELs are being developed as sources for swept source optical coherence tomography (SS-OCT) [3], gas sensing [4] and diffuse optical spectroscopic imaging (DOSI) [5].
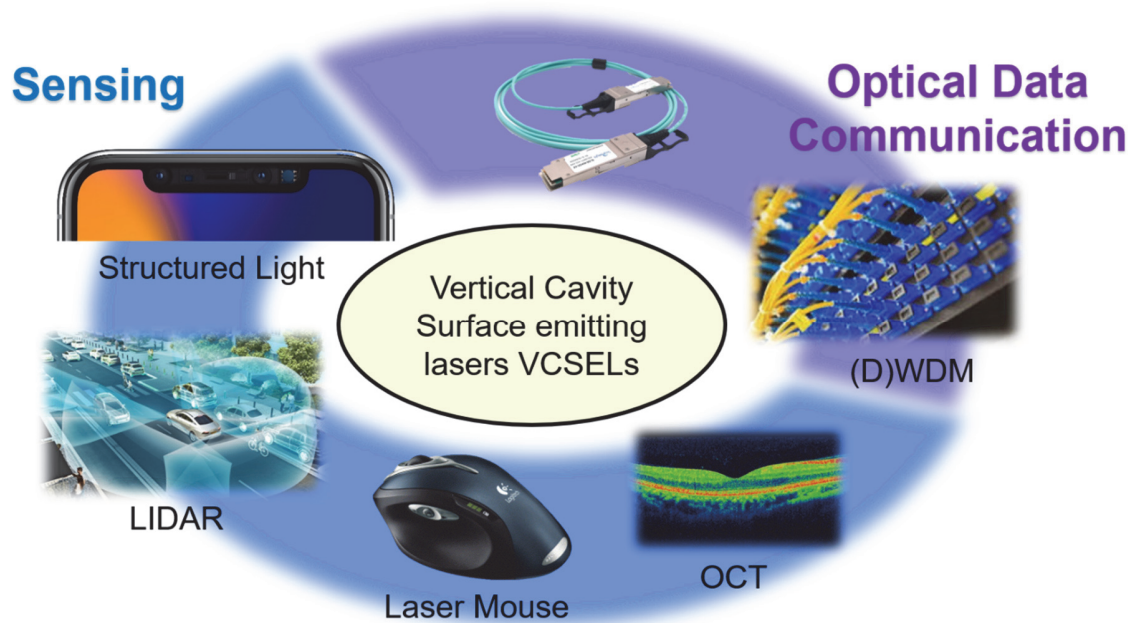
Fig. 1.2 Applications of VCSELs: Traditional applications include optical communication, including (dense) wavelength division multiplexing (D)WDM and laser mice. In the area of optical sensing VCSELs have recently found new applications as illumination sources for structured light, time of flight light detection and ranging (LIDAR) and as tunable light sources for optical coherent tomography (OCT)

15

2 Development of Epitaxial Material

As outlines in section 1.1 quality epitaxial material builds the foundation of every VCSEL. This chapter illustrates the major milestones in the development of the epitaxial material for GaAs VCSEL devices. The first section describes the development of an InGaAs multi quantum well (MQW) structure with strain compensating GaAsP barriers. Section 2.2 presents the calibration of dopant density for GaAs and AlGaAs material and the demonstration of a light emitting diode (LED) to test the electroluminescence of the MWQs. To measure gain of the quantum wells and material edge emitter lasers are fabricated and characterized. Finally, a complete VCSEL structure was realized and lasing emission was observed.

2.1 Strain Compensated InGaAs/GaAsP Multi Quantum Well

When crystalline semiconductors of different lattice constants are epitaxially gown on a substrate the deposited layer assumes the lattice constant of the substrate in lateral direction and changes is vertical lattice constant accordingly. This behavior is called pseudomorphic growth and it continues until a critical thickness of the strained layer is reached. Beyond the critical thickness the strained layer relaxes and the material assumes its own lattice constant under formation of defects. Fig. 1.1 depicts schematics of tensile and compressively strained layers, pseudomorphically grown on a substrate. As one result of the strain the electronic band structure of the alloy is changed. In the unstrained material the conduction band (CB) is separated by the band gap from the energy levels of the valence band that contains the degenerated heavy hole (HH) and light hole (LH) states as well as the split-off band (SO). The isotropic component of the material strain enlarges the band gap by the value H in the case of compressive strain and shrinks it for tensile strain respectively. The parameter H' denotes the corresponding change in the conduction band energy. The biaxial component of the strain lifts the degeneracy of heavy hole and light hole states, which is governed by the parameter S. Additionally, light hole and split-off states are shifted by $\delta = 2S^2/\Delta$, where Δ is the energy gap between the HH/LH and SO bands. For detailed treatment of this matter the reader be referred to chapter 4 of SL Chuang's book [6]. Two different single quantum well structures on GaAs substrate where simulated using the nextnano software [7]. The first structure is a compressively strained 6 nm wide $In_{31}Ga_{69}As$ QW with unstrained GaAs barriers. The second structure contains the same $In_{31}GaAs$ QW, but features tensile strained $GaAs_{75}P_{25}$ barriers. First material strain was calculated, then Poisson and single band Schrodinger equations where solved self constantly for Dirichlet boundary conditions. The resulting band structures and quantum states are plotted in Fig. 2.2.
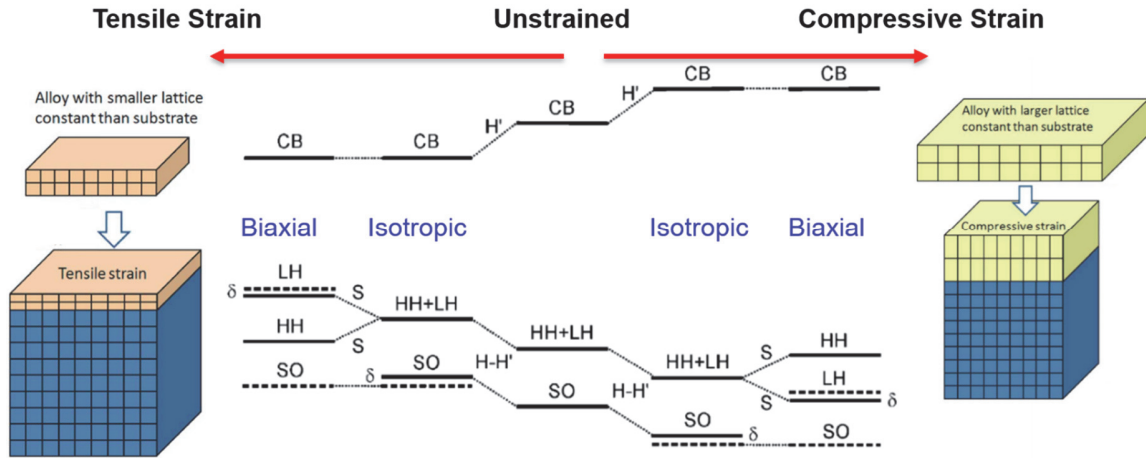
Fig. 2.1 Strain in a crystalline semiconductor. The strain changes the electronic band structure of the semiconductor. Graphic modified from [8][9]

From the comparison of the band structures the two QWs in Fig. 2.2 (a) one can see that the use of GaAsP barriers leads to a higher confinement potential in both the conduction band (CB) and the two valence bands (HH/LH), which aids the carrier confinement of the QW structure. In Fig. 2.2 (b) the relevant states are quantum wells are plotted. The calculated wavelength of the optical transition between the ground state of the electrons (ee1) and the ground state of the heavy holes (hh1) is 1065 nm. The result of the simulation agrees very well with the photoluminescence spectrum of a corresponding 10 MQW structure with similar alloy compositions and QW width, which emits at a wavelength of 1054 nm.
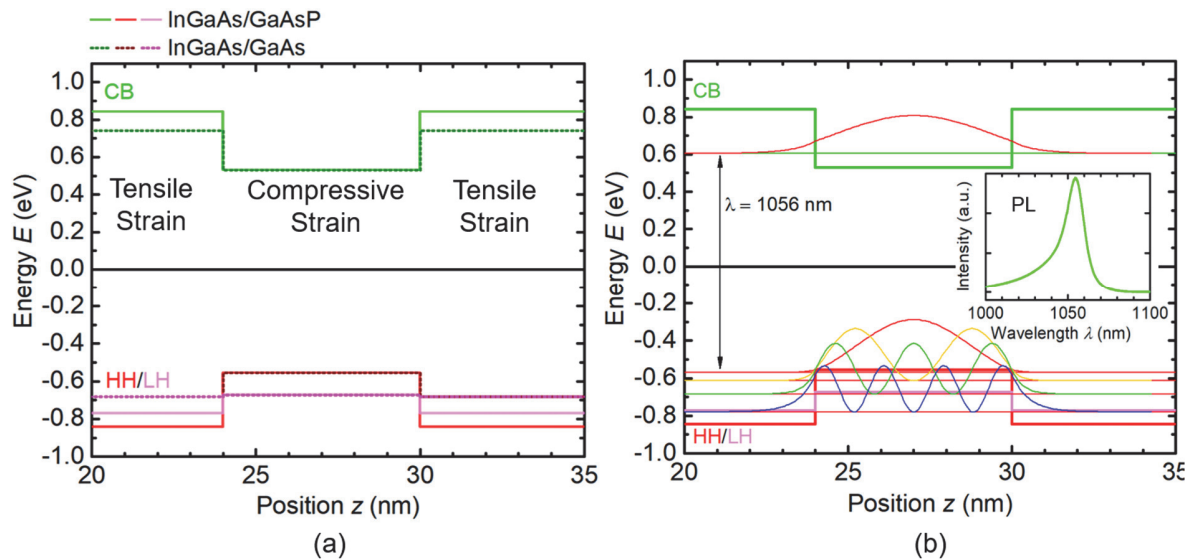
Fig. 2.2 Single band Schrödinger simulation of the band structure of a QW. (a) Comparison of band structure of InGaAs single QW with GaAs cladding and GaAsP cladding. (b) Simulation of bound

quantum states in the InGaAs/GaAsP QW and photoluminescence spectrum of a corresponding 10 MQW sample.

This example illustrates another advantage of the strain compensated quantum well. By carefully designing thickness and phosphorus composition of the GaAsP barriers a strain balance can be obtained. While each individual layer of InGaAs and GaAsP is strained by itself, the opposite polarities of strain neutralize each other. As a result, the number of quantum wells is not limited via a critical thickness. A further benefit of the strain balanced structure is of practical nature. As industry moves to larger wafer sizes to satisfy high device volumes demanded by emerging applications of VCSELs in consumer products, residual strain manifests itself in a larger wafer warpage that leads to manufacturing problems. A strain balanced QW structure elevates this challenge. Fig. 2.3 shows experimental results related to the optimization of the strain compensated InGaAs/GaAaP MQWs. In Fig. 2.3 (a) a transmission electron microscope (TEM) image of such structure with 10 MQWs is shown. Part (b) of the graphic presents the photoluminescence spectra of InGaAs/GaAsP MQWs with 10, 20 and 40 wells respectively. For the structure with 40 wells the barrier width was reduced from 7 nm to 6 nm to fine tune the strain balance. As result the photoluminescence intensity is maintained for an increasing number of quantum wells, indicating relaxation free pseudomorphic growth. Since the ratio of barrier and well material changes with the number of quantum wells, the strain compensation in each structure has to be separately optimized. Fig. 2.3 (c) shows the optimization of phosphorous content of the barrier alloy for a structure with 3 wells as example. Based on the photoluminescence intensity the optimum strain balance was obtained by reducing the phosphorous content of the barriers by 37.5%.
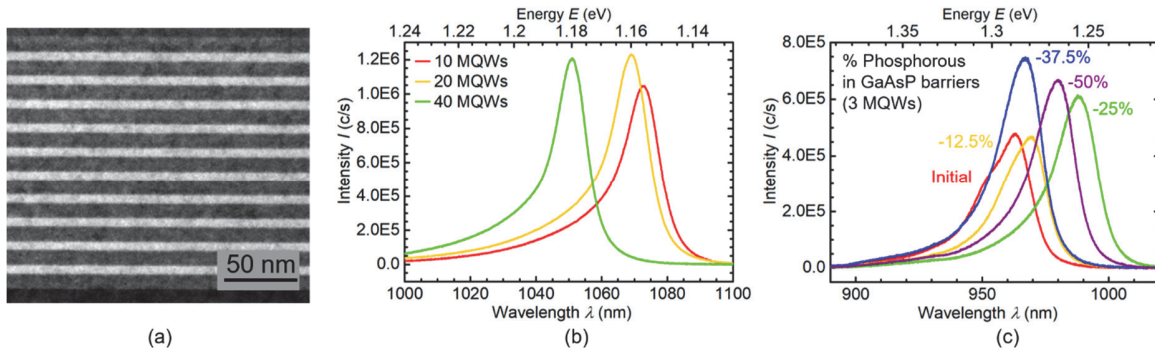
Fig. 2.3 Strain compensated MQW. (a) TEM of a MQW with 10 InGaAs QWs and GaAsP barriers. (b) Room temperature photoluminescence of samples with 10, 20, 40 MQWs. (c) Optimization of the strain balance in a 3 MQW structure, by adjusting the phosphorous content of the barriers.

To verify the material quality low temperature photoluminescence of a sample with 10 MQWs (R17088) was measured. A liquid helium cooled cryostat was used to reach temperatures down to 4.4 K and a thermoelectric element was used to heat the sample in steps to 300 K. photoluminescence (PL) spectra are shown for the different temperatures in Fig. 2.4 (a). At 4.4 K the integrated PL intensity is highest as the internal quantum efficiency is close

to 100%. This is confirmed by the power dependent PL study at the end of this section. With raising temperature, the PL intensity declines as thermally activated recombination centers lead to an increased share of non-radiative recombination. From the ratio of integrated PL counts at the respective temperature and 4.4 K, the internal quantum efficiency (IQE) can be calculated. As plotted in Fig. 2.4 (b) the IQE drops below 50% at room temperature. The temperature dependence of the IQE was fitted with an Arrhenius fit. The experimental errors were obtained from the standard deviation of 5 PL measurements at each temperature and a temperature uncertainty of the controller of 0.2 K. As expected with rising temperatures the linewidth of the PL spectra broadens. This is shown in Fig. 2.4 (c). At the same time the wavelength shifts red as the bandgap shrinks with rising temperature.
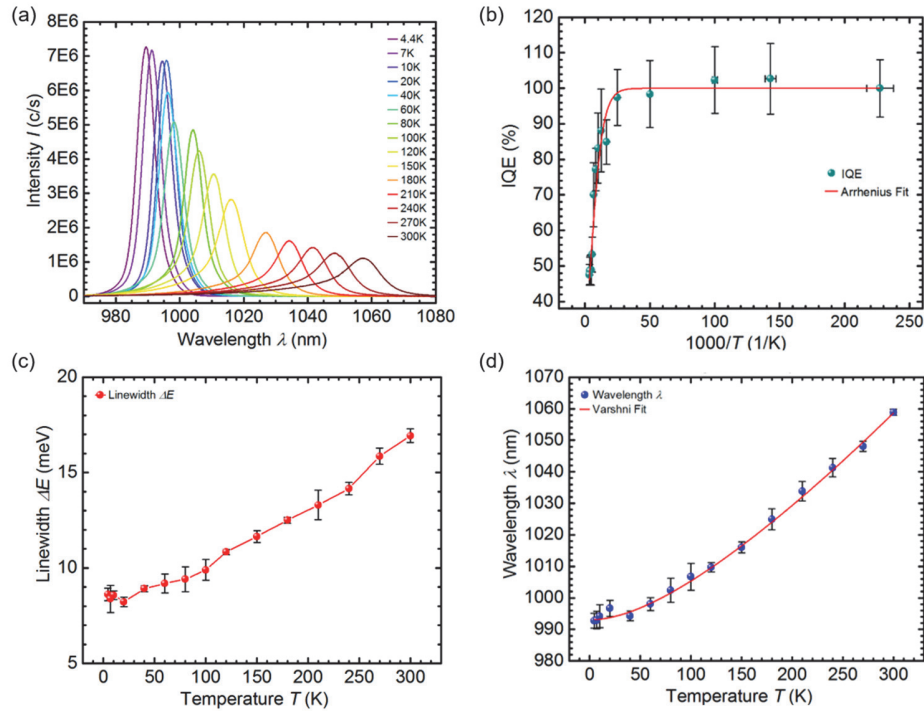
Fig. 2.4 Low Temperature photoluminescence. (a) Spectrum as function of temperature. (b) IQE as function of temperature follows an Arrhenius law. (c) Linewidth increases as a function of temperature as expected. (d) Emission wavelength of the MQW increases with temperature as the bandgap narrows following the empirical Varshni-equation.

Fig. 2.4 (c) shows this behavior, which can be described with the empirical Varshni-equation, where the bandgap is given as $E_g = E_0 - \alpha T^2/(T + \beta)$ [10]. E_0 describes the energy bandgap at 0 K and the two constants α and β are called Varshni-parameters. Since the IQE of the quantum wells was only 50% at room temperature, the strain balance was optimized in the 10 MQW structure. The optimized structure (R17116) was again analyzed by PL and the results are shown in Fig. 2.5. Part (a) shows a double logarithmic plot of the power dependence of the PL intensity as function of the excitation power for 300 K as well as 4.4 K.

19

The dependence follows a power law and the measured exponent (ideality factor) of $n = 1$ indicates a radiatively dominated recombination process [11]. In Fig. 2.5 (b) the IQE of the two 10 MQW samples and of a single QW structure are compared as function of the optical excitation power. While all three samples reach an IQE between 70 – 90 % above 1 mW. At low excitation power <100 µW the IQE of the optimized sample R17116 drops only weakly, while the IQE of the samples R17088 and the SQW R17065 drops sharply. The reason is that at low excitation powers non-radiative combination on defects dominates in those samples. In contrast the results of the optimized structure (R17116) indicate a low defect density. Fig. 2.5 (c) and (d) concludes the power dependent PL study. In (c) the linewidth of the PL emission peak is compared at 4.4 K and 300 K s function of the excitation power. The linewidth increases both with temperature as well as excitation power reflecting the energy distribution of the recombining carriers in the conduction and valence band states. Part (d) illustrates the influence of the excitation power on the PL spectrum in case of a room temperature measurement. For higher powers spectral broadening predominantly on the blue side of the spectrum is observed, which can be attributed to band filling of carriers.
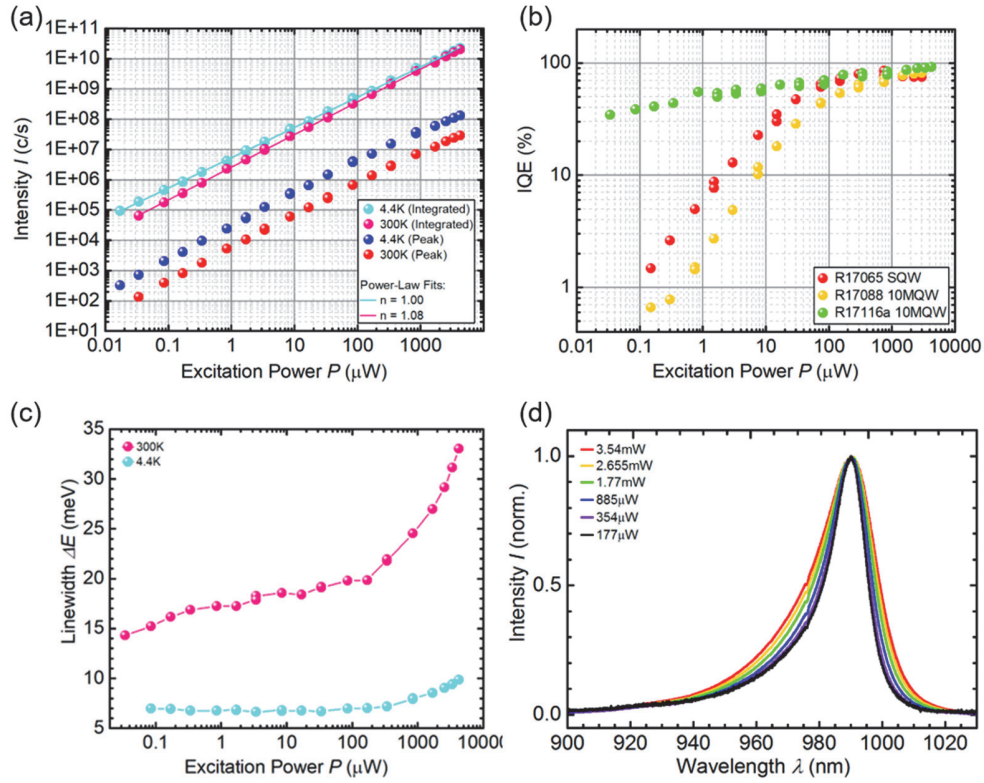
Fig. 2.5 Power dependent photoluminescence spectroscopy. (a) Integrated and peak counts of PL as function of excitation power at room temperature and at 4.4K. (b) Calculated internal quantum efficiency of 3 samples: single QW (red), 10 MQWs (yellow), optimized 10MQWs green. (c) Linewidth of PL emission as function of excitation power at RT and 4.4K. (d) Spectral broadening due to band filling at higher excitation powers.

20

2.2 Doping Calibration and Electrical Injection

Just as important as the optimization of the MQW structure in the previous section is the realization of electrical injection of carriers into the active region by doped GaAs and AlGaAs. This section describes a series of Hall measurements used to calibrate doping densities in GaAs and AlGaAs alloys of various compositions. Carbon is used as a p-dopant and Tellurium is used as a n-dopant. For each data point a separate sample was grown. Unintendedly doped (intrinsic) GaAs was used as a substrate and for the buffer layer. For the doping calibration of GaAs several 100 nm of doped material where grown as top layer, for the AlGaAs doping calibrations first 100 nm undoped AlGaAs was grown on top of the GaAs buffer and then 200 nm of doped AlGaAs was grown as concluding layer. In each corner of the 1x1 cm sized samples indium flakes where applied as contacts for the Hall measurement. Fig. 2.6 shows the results of the doping calibration for tellurium n-doped GaAs. Part (a) shows the carrier concentration and mobility as a function of the diethyl-tellurium (DETe) mole fraction during growth. The obtained carrier concentrations span a range from $5 \cdot 10^{17} \text{cm}^{-3}$ to $> 1 \cdot 10^{19} \text{cm}^{-3}$. As expected, the higher impurity concentrations decrease the measured mobility. The resulting material conductivities and resistivities are plotted in Fig. 2.6 (b). Conductivity increases for higher doping densities, but saturates above a DETe mole fraction of 0.04. Part (c) of the figure compares the obtained results with literature [12][13]. The solid lines indicate electron drift and the dashed lines Hall mobilities. The curves are plotted for compensation ratios $(N^+ + N^-)/n$ and can be used to determine the acceptor concentration.
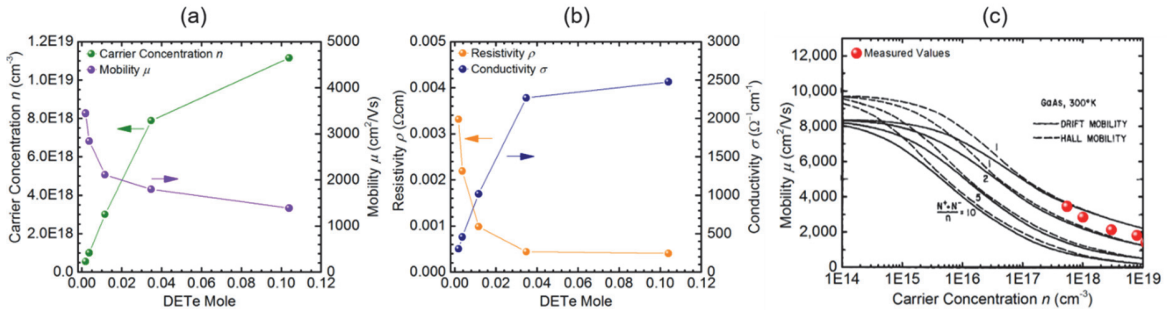
Fig. 2.6 Hall measurements for the calibrations of n-doped GaAs. (a) Carrier concentration and mobility of n-doped GaAs as function of DETe mole fraction during MOCVD growth. (b) Corresponding resistivity and conductivity. (c) Comparison of measured carrier concentrations and mobilities with literature [13].

• The incorporation of tellurium dopants depends on the alloy composition of AlGaAs. Thus, aluminum mole ratio was varied from 0 – 45% to calibrate n-doping in AlGaAs. Fig. 2.7 shows the measurement of the carrier concentration as a function of aluminum mole ratio. At constant DETe mole ratio the free carrier concentration drops over more than an order of magnitude. This is rooted in a corresponding increase of the activation energy of the dopants

as described by Houng et al. in [14]. In (b) the activation energies were calculated in a simplified way by $E_A(X_{Al}) = \left(\ln(n_{GaAs}) - \ln(n_{X_{Al}}) \right) \cdot k_B T$ from our measurements assuming the activation energy of tellurium in GaAs to be zero. Both carrier concentration and activation energy of our samples (Fig. 2.7 (a, b)) show good agreement with the results obtained by Houng et. al. presented in Fig. 2.7 (c, d).
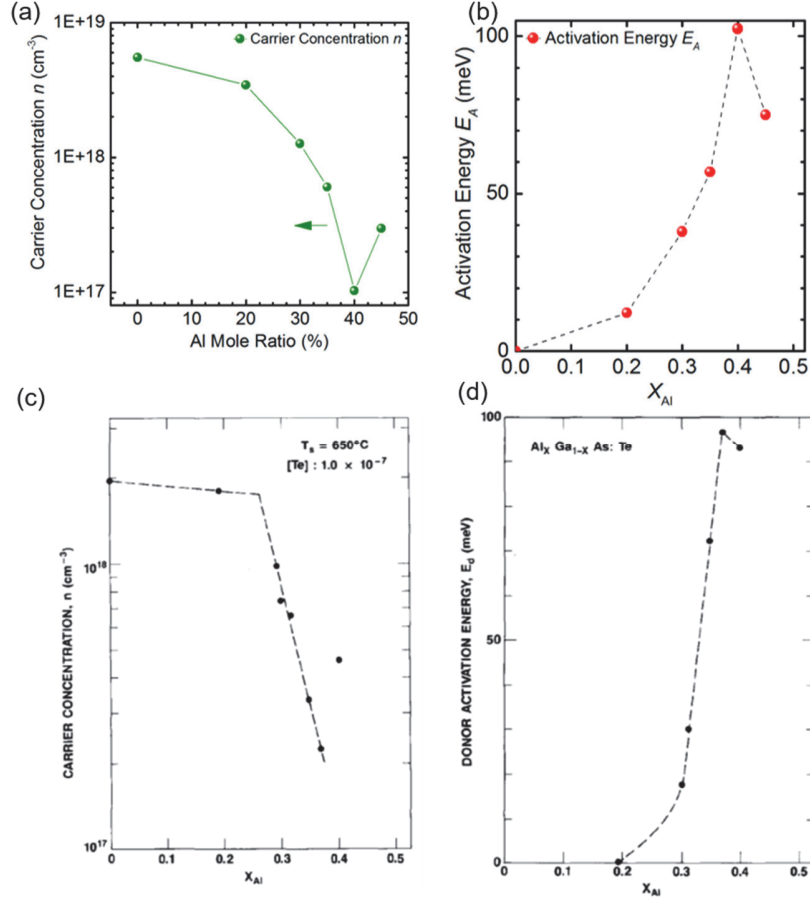
Fig. 2.7 Hall measurements for the calibration of n-doped AlGaAs. (a) Carrier concentration as function of aluminum mole fraction in the AlGaAs compound. (b) Dopant activation energy as function of the aluminum mole fraction. (c-d) Results of Houng et al. [14] are in good agreement with the measurements in this work.

In similar fashion to the n-doped material, p-doping densities were analyzed. 4 samples doped with different carbon tetrabromide (CBr4) mole fractions achieved Hall carrier densities from $3 \cdot 10^{17} \text{cm}^{-3}$ to $1 \cdot 10^{19} \text{cm}^{-3}$ as shown in Fig. 2.8 (a). The obtained hole mobilities are expectedly lower compared with the electron mobilities determined earlier and mobility drop for higher doping densities, too. Resulting conductivities and resistivities for the p-GaAs material are plotted in Fig. 2.8 (b).
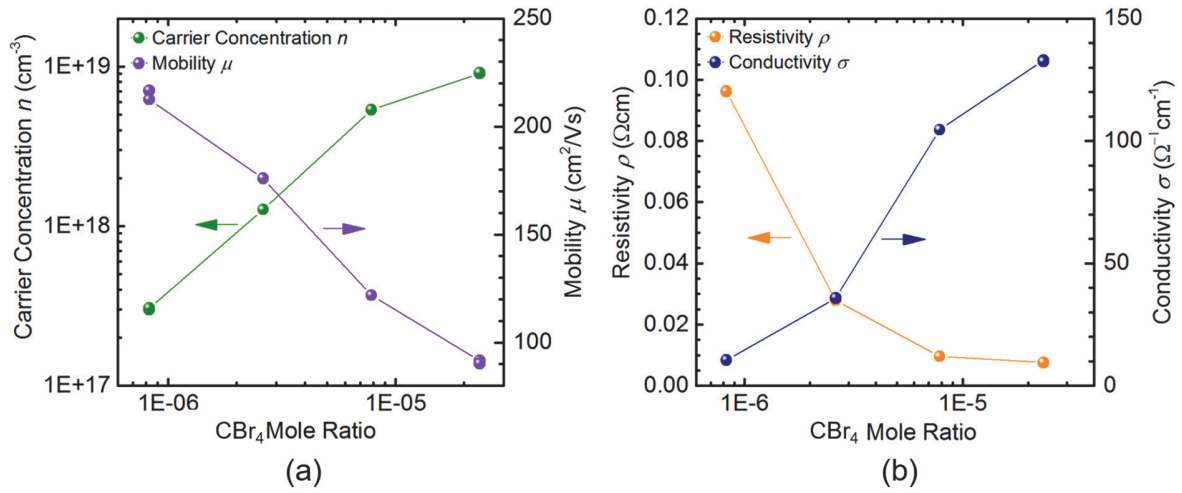
Fig. 2.8 Hall measurements for the calibrations of p-doped GaAs. (a) Carrier concentration and mobility of p-doped GaAs as function of CBr_4 mole fraction during MOCVD growth. (b) Corresponding resistivity and conductivity.

P-doped AlGaAs alloys were investigated for aluminum fractions from 0-90%. Fig. 2.9 (a) shows once again the carrier concentration and mobility for samples of varying AlGaAs alloys, part (b) of the graphic the resistivity and conductivity of the materials. The solid and dashed lines with circles and squares as symbols correspond to the two different CBr_4 flows of 110 and 25 sccm respectively. For rising Al contents, the carrier concentration rises at constant doping flow, as the dopant incorporation efficiency increases. Mobility drops for alloys with medium Al content by rises sharply from $Al_{60}GaAs$ to $Al_{90}GaAs$. This leads to an increase in conductivity for the $Al_{90}GaAs$ alloy compared to the lower aluminum content alloys.

To test the electrical injection into the active region a light emitting diode (LED) structure was realized. N-doped GaAs substrate was used. After growth of the n-doped GaAs buffer layer the active region with 10 pairs of InGaAs/GaAsP strain balanced QW was grown surrounded by a 50 nm thick undoped AlGaAs cladding layer on either side serving as carrier confinement. A 200 nm thick p-doped GaAs layer and a 20 nm highly p-doped contact layer formed the top of the epitaxy. LED devices were fabricated in a simple microfabrication process. First, titanium and gold layers were evaporated on both the back and front of the epitaxy to form ohmic contacts, where the p-contacts on the front side of the chip where patterned by a lift-off process. After the metallization steps, diamond shaped mesas where patterned with a second lithography step using a Piranha based etch. The result of the fabrication is shown in the 3D confocal microscope image of Fig. 2.10 (a). One can see the c-shaped p-contact aligned on top of the diamond shaped mesa. An InGaAs CCD camera was used to observe the electroluminescence of the LED (part (b) of the figure) and voltage and optical power of the LED was measured as a function of injected current (LIV curve) by

placing a Ge photodiode above the LED chip. The experiment in summary, demonstrates successful electrical carrier injection in to the active region and radiative recombination of carriers.

(a)

(b)
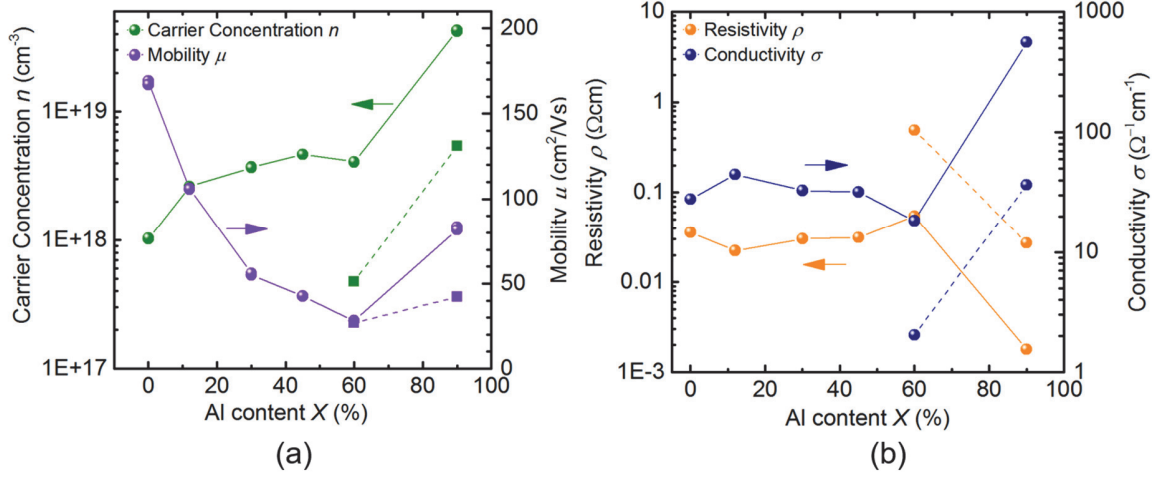
Fig. 2.9 Hall measurements for the calibrations of p-doped AlGaAs. (a) Carrier concentration and mobility as function of aluminum mole fraction in the AlGaAs compound. (b) Corresponding resistivity and conductivity. Solid lines and circles indicate 110 sccm CBr_4 flow, dashed lines and squares 25 sccm CBr_4 flow.
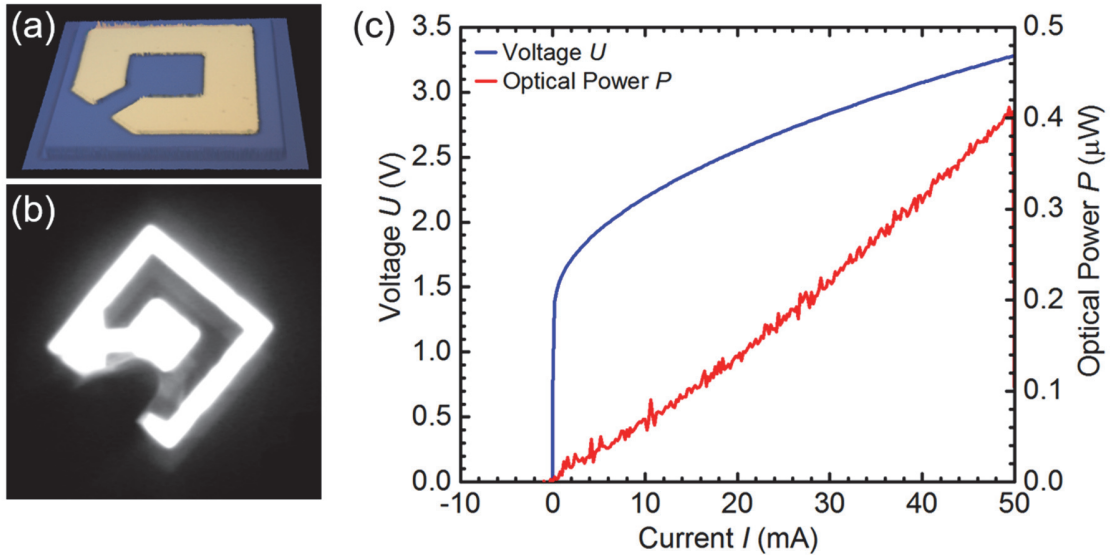
Fig. 2.10 Demonstration of a light emitting diode (LED). (a) Confocal microscope 3D image of a device showing mesa and metal pad. (b) Image of the electroluminescence of the LED taken with an InGaAs CCD camera. (c) LIV curve of the LED.

24

2.3 Material Gain and Loss

While electroluminescence was demonstrated in the previous section. A quantitative analysis of QW gain and material loss is useful before attempting to realize a full VCSEL structure. Compared to the VCSEL, the growth of edge emitter lasers is less demanding, as both, the number of epitaxial layers is lower and their thickness requirements are less stringent. Additionally, the edge emitter laser (EEL) structure allows for a systematic variation of the cavity length by fabricating bars of different length based one epitaxy, which allows to determine QW gain and loss in experiment. Details of the following method and the corresponding derivations are described by L. Coldren [15]. In essence the material loss α_i and internal quantum efficiency η_i can be determined from the slope and offset of a linear fit, when the measured external slope efficiency η_e is plotted inverted as function of the device length L. This can be seen from Eq. 2.1:

$$\frac{1}{\eta_e} = \frac{1}{\eta_i}\left(1 + \frac{\alpha_i L}{\log\left(\frac{1}{R}\right)}\right) \qquad \text{Eq. 2.1}$$

Here the parameter R refers to the product of the reflectivities of the two individual laser facets $R = R_1 R_2$, which can be calculated for a known facet material. To determine the optical gain of the active material at the laser threshold g_0, the logarithm of the measured threshold current densities j_{th} is plotted as a function of the inverse laser length L. As can be seen from Eq. 2.2, by performing a linear fit, transparency current density j_{tr} can be determined for the limit of infinite laser length and the threshold gain g_0 can be found from the slope of the fit.

$$\log(j_{th}) = \log(j_{tr}) + \frac{\log\left(\frac{1}{R}\right)}{L\Gamma g_0} \qquad \text{Eq. 2.2}$$

Both confinement factor Γ and the reflectivity product are obtainable by calculation.

The following epitaxial structure was used for the edge emitter laser in the described experiment. N-doped GaAs was used as substrate. The active region with 3 pairs of InGaAs/GaAsP strain balanced QWs forms the center of the EEL. It is surrounded on top and bottom by 100 nm thick carbon and tellurium doped waveguiding layers respectively. The waveguiding layers have a compositional gradient from Al$_{60}$GaAs to Al$_{30}$GaAs towards the QWs. This is structure is commonly called graded index separate confinement heterostructure (GRINSCH) [16][17]. Active region and waveguiding layers are surrounded by 1.5µm thick, respectively doped Al$_{60}$GaAs layers which form the cladding of the laser. The very top of the structure is again formed by a 20 nm thick highly p-doped GaAs contact layer. Consecutively, laser bars where fabricated. First, 200 nm thick PECVD SiO2 was deposited and stripes of 5 - 50 µm width were etched to expose areas for subsequent p-contact evaporation. For the p-contacts Ti, Au was evaporated and patterned, so that 50 µm metal strips cover the previously exposed contact areas. The result is shown in Fig. 2.11 (a), which presents a 3D confocal

microscope image of several laser bars of varying width. The substrate side of the chip was lapped to a thickness of 150 – 200 µm before the Ti-Au n-contact was evaporated to aid the cleaving process. Finally, the chip was cleaved to obtain laser bars with 1000 – 1750 µm length. CCD images of the laser facet show electroluminescence of a device. Spontaneous emission is observed below threshold (10 mA) in Fig. 2.11 (b) and stimulated emission was achieved above threshold at 120 mA current in part (c) of the graphic. The image shows a speckle pattern characteristic for coherent light of a laser. The far field of the EEL has the characteristically elliptical shape as observed with an IR card in part (d) of the graphic. The spectrum of the laser bar was measured at different currents close to and above the threshold as shown in Fig. 2.11 (f). Each spectrum features closely spaced Fabry-Perot modes defined by the cavity length. The lasing modes are determined by the wavelength of the gain peak of the MQW. With rising current the temperature in the lase increases, the gain peak shifts to lower energy and as a result the lasing modes of the spectrum shift red.
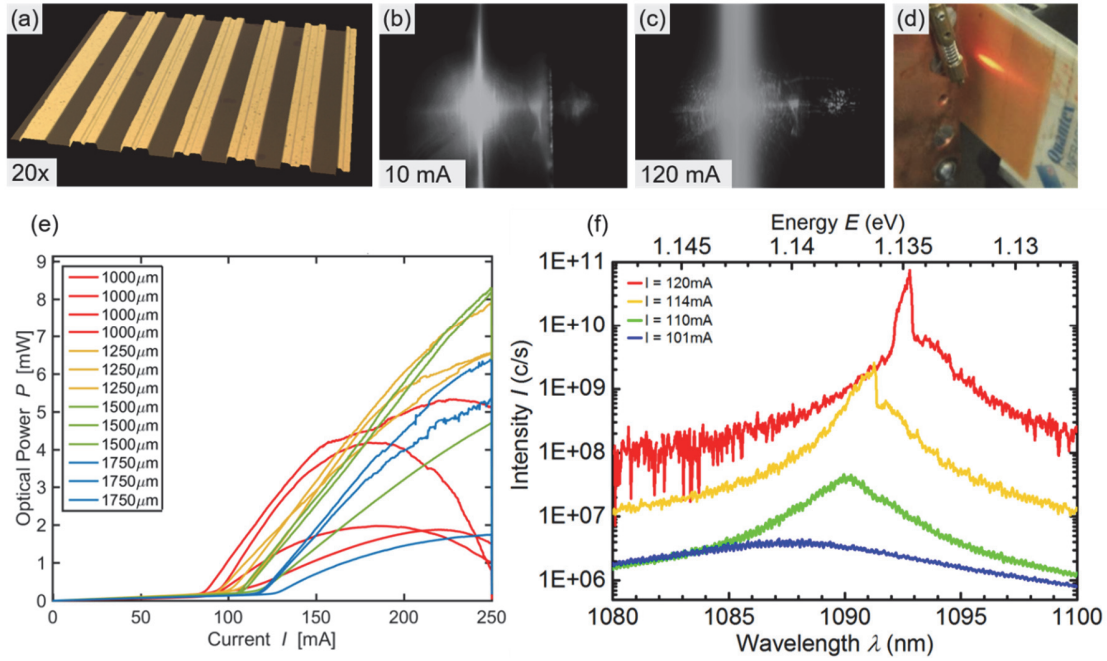
Fig. 2.11 Demonstration of an edge emitting laser. (a) Confocal microscope 3D image of laser bars of various widths. (b, c) Silicon CCD image of the optical emission below (10 mA) and above (120 mA) lasing threshold. (d) Photograph of the elliptical far field of the edge emitter laser detected with an IR card. (e) LIV curves of a selection of laser bars with a width of 15 µm and length of 1000 - 1750 µm. (f) Spectra below and above lasing threshold of a 20 µm wide and 1000 µm long.

Fig. 2.11 (e) shows the LI curves of multiple devices with different cavity lengths and a width of 15 µm. All curves follow the typical L-shape for a laser. At low currents the optical emission rises slowly and is dominated by spontaneous emission. Above the threshold of 90 – 125 mA the devices start to lase and the optical power increases rapidly and linear with the supplied current. At even higher currents slope efficiency and finally optical power decrease

26

as consequence of the strong internal heating that lowers the internal quantum efficiency of the device. Threshold current densities and differential (external) quantum efficiency closely above threshold where extracted from the LI curves and plotted as a function of laser bar length as described at the beginning of the section. The results are shown in Fig. 2.12. Linear fitting was used to find the following values for the internal parameters of the laser. From part (a) of the graphic IQE was determined to be $\eta_i = 17.1\%$ and intrinsic (material) loss to be $\alpha_i = 5.5 \text{ cm}^{-1}$. The scattered data points in the graph which belong to devices of low external quantum efficiency are believed to be caused by imperfect cleaving of the laser facets. From plot (b) a transparency current density of $j_{tr} = 311 \text{ A cm}^{-2}$ and a material gain of the 3 QW active region of $g_0 = 476 \text{ cm}^{-1}$ was obtained. Although these numbers clearly underperform compared to reported results in literature [18], the obtained values for the internal laser parameters are in the correct order of magnitude.
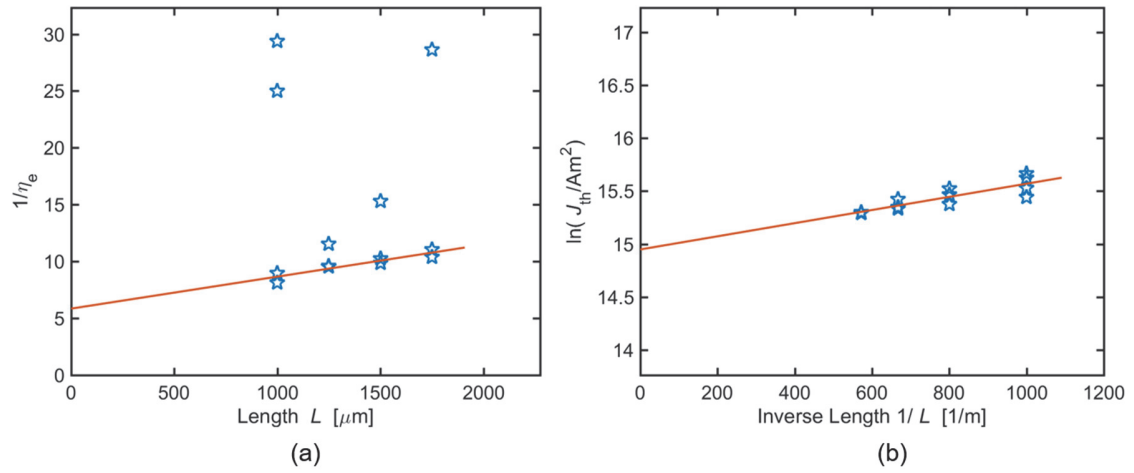
Fig. 2.12 Determination of gain and loss. (a) Inverse of the differential external quantum efficiency (EQE) η_e as function of the length L of the laser bars, to extract internal quantum efficiency (IQE) η_i and material loss α_i. (b) Logarithm of threshold current density j_{th} as function of inverse length of the laser bars, to extract transparency current density j_{tr} and material gain g_0.

2.4 Conventional DBR VCSEL

In this section the results of the first successful VCSEL growth and fabrication are presented. Compared to the edge emitter laser structure the growth of a VCSEL cavity is challenging, since the short cavity requires very high reflectivity of both the bottom (>99.9%) and the top DBR (~98%). In order to reach such high reflectivities the bottom DBR was designed with 33 pairs of alternating $\lambda/4$ thick n-doped GaAs and $Al_{90}GaAs$ layers. The bottom DBR was commercially grown and cantered around 980 nm wavelength. The DBR substrate featured an additional 1λ thick GaAs cap layer and a terminating protective layer of GaAsP. At the beginning of the inhouse MOCVD growth the GaAsP layer was selectively desorbed at high temperature under tertiarybutylarsine (TBA) atmosphere to obtain a clean GaAs surface for high quality growth of the active region. The detailed method is described by Wang et. al. [19]. As described earlier p-doping and MQW structure of the active region were optimized independently, as was the reflectivity of the $\lambda/4$ top DBR layers. Layer thicknesses were calibrated by utilizing scanning electron microscope images of the cross sections of the individual layers and reflectivity spectra in the case of the DBR pairs. After these calibrations the full VCSEL structure was grown onto the commercial DBR substrate. First, the active region with 3 pairs of InGaAs/GaAsP strain compensated QWs surrounded by $Al_{30}GaAs$ cladding layers forming the 1λ cavity where grown on a $\lambda/4$ $Al_{60}GaAs$ phase matching layer on top of the 1λ GaAs buffer. On top of the cavity the p- doped oxidation layer was grown and 22 pairs of p-doped, graded $GaAs/Al_{90}GaAs$ DBR. The top of the VCSEL structure was capped by GaAs material with a 20 nm highly p-doped GaAs contact layer. An SEM cross section of this full VCSEL epitaxy is shown in Fig. 2.13 (a). After growth the reflectivity of the entire VCSEL structure was measured and a range of high reflectivity (920 -1080 nm) is clearly visible. In the center of this wavelength range a dip in reflectivity indicates the position of the cavity resonance. Photoluminescence spectroscopy confirms the presence of the resonance, as it shows a strong emission peak at the same wavelength. Both measurements are shown in part (b) of the graphic. After confirmation of the resonance wavelength and alignment of the reflection bands VCSEL devices were fabricated in similar steps as the LED process described in section 2.2. Additionally, after contact deposition and mesa etch the VCSEL sample was oxidized with water vapor in nitrogen atmosphere. In this process the high aluminum content AlGaAs alloy of the oxidation layer is converted into a porous oxide, which forms a current and optical mode confining aperture in the center of each mesa. The pattern used featured a range of different sizes of diamond shaped mesas leading in turn to a distribution of different sizes of current apertures. As a result, single as well as multimode VCSELs were realized. Fig. 2.13 Demonstration of a VCSEL. Cross-sectional SEM image (a) and reflectivity and photoluminescence spectrum (b) of the DBR VCSEL epitaxy. (c) LIV curve and micrograph a fabricated DBR VCSEL. (d) Single mode lasing spectrum of a DBR VCSEL device showing 35 dB side mode suppression ratio. (e) Spectrum of the device from c, showing multi-mode lasing. (c) shows the LIV curve obtained from a multimode VCSEL. A micrograph of the lasing device is shown in the upper left corner of the diagram. Part (e) of

the graphic shows the multimoded spectrum of the same device. The spectrum in part (d) of the graphic demonstrates single mode lasing with ~35 dB side mode suppression ratio (SMSR) obtained from a different VCSEL device on the same chip with smaller oxide aperture. Although voltage and output power of this device can certainly be improved the successful demonstration of a VCSEL constituted an important milestone for the development of our inhouse MOCVD routine and at the same time serves as an example of the steps necessary to develop GaAs VCSEL epitaxy and fabrication capability.
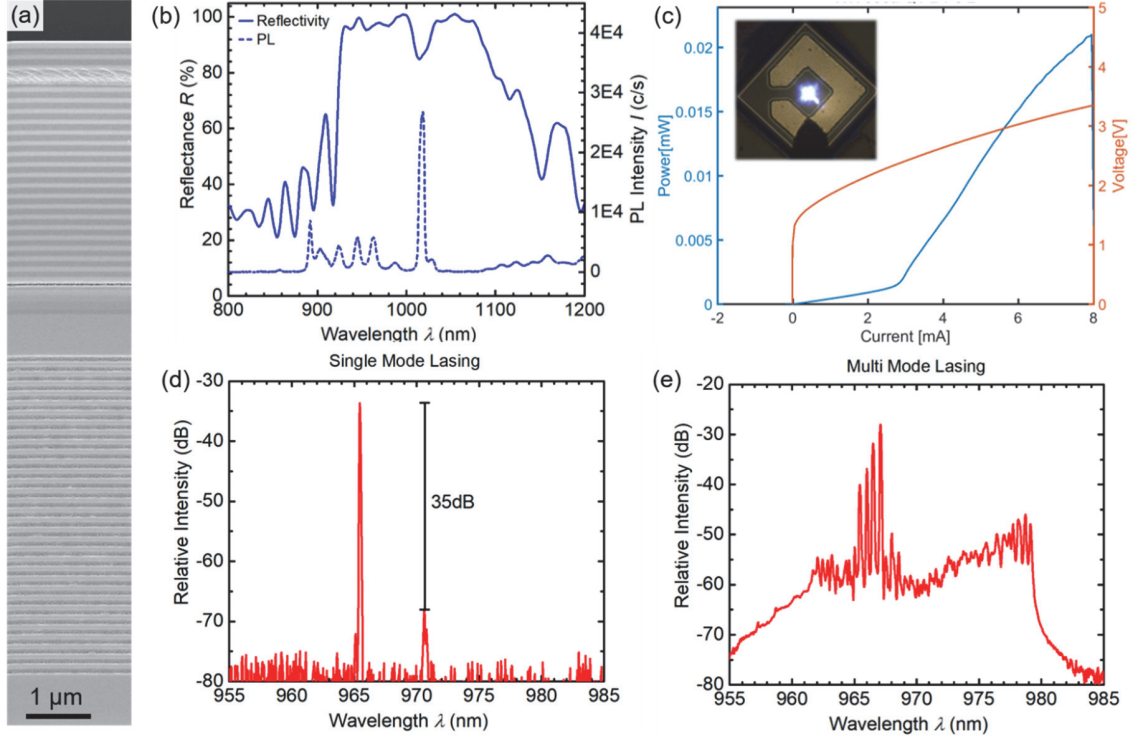
Fig. 2.13 Demonstration of a VCSEL. Cross-sectional SEM image (a) and reflectivity and photoluminescence spectrum (b) of the DBR VCSEL epitaxy. (c) LIV curve and micrograph a fabricated DBR VCSEL. (d) Single mode lasing spectrum of a DBR VCSEL device showing 35 dB side mode suppression ratio. (e) Spectrum of the device from c, showing multi-mode lasing.

3 Optically pumped HCG VCSEL

One of the emerging applications of VCSELs is their use as widely wavelength tunable source for high resolution optical coherence tomography (OCT) systems. Single transverse mode VCSELs as result of their short cavity length promise mode hop free tuning over the available free spectral range (FSR), the spacing between two consecutive longitudinal modes. Since the FSR is inversely related to the effective cavity length, a shorter cavity length allows for a larger mode hop free tuning range in an FSR limited device. Optically pumped VCSEL, since they do not need layers for electrical injection can have shorter cavities and can make use of dielectric or oxidized DBRs which have broader reflectivity bands. Unsurprisingly optically pumped VCSELs with wide wavelength tuning have been demonstrated using these technologies [20][21]. An additional advantage of optically pumped VCSELs are the simplified fabrication and epitaxy requirements compared to a similar electrically pumped device. In particular doping and the fabrication of contacts can be omitted. Thus, in the following section optical pumping for VCSELs with high contrast grating (HCG) top reflector has been investigated. An extensive review of the properties and applications of HCG (including as reflector for VCSELs) is presented in the publication by C. J. Chang-Hasnain [22]. The primary intend in this work was to test the suitability of optical pumping in combination with an HCG top mirror. Besides that, the possibility was evaluated to use optically pumped test structures with low fabrication complexity instead of fully fabricated electrically driven devices to obtain feedback on the quality of different epitaxy and HCG designs. The results obtained on full VCSEL structures in the following sections 3.1 and 3.2 used devices similar to the ones published by K. Li et al. [23].

3.1 Experimental Setup

The optical pumping experiments conducted here utilized a setup similar to the one used for the photoluminescence (PL) measurements in section 2.1 earlier. A schematic of this setup is presented in Fig. 3.1. A femtosecond pulsed Ti-sapphire laser is used as a pump. This laser is wavelength tunable over a range of 680 - 1080 nm and pulses of 120 fs length are provided at an 80 MHz repetition rate. The power of the pump laser is adjusted via a variable attenuator and its polarization fixed by a linear polarizer thereafter. To obtain a power measurement of the pump light the beam passes through a splitter which directs a known minority fraction of its light to a photodiode based calibrated power meter. The majority of the pump beam transmits through this beam splitter and passes through a $\lambda/2$ wave plate, which is used to rotate the polarization of the pump beam with respect to the sample. A dichroic beam splitter reflects the pump light towards a 50x objective which focuses the light on the sample, where it enters the VCSEL cavity though the high contrast grating top mirror. Here the pump light gets absorbed, the generated charge carriers thermally relax to the band minimum, (ideally) recombine in the quantum wells of the device and emit photoluminescence light (ordinarily in form of spontaneous emission). At sufficiently high pump power the device reaches its lasing

threshold and simulated emission becomes the dominant recombination mechanism. In either case emitted light leaves the VCSEL, is collected by the 50x objective and transmits through the dichroic mirror. A mirror on a flip mount allows the PL light to pass through a linear polarizer and finally get detected by a grating spectrometer with Silicon CCD detector. When the flip mirror is moved into the beam path the sample is illuminated and imaged by a lamp and camera setup.
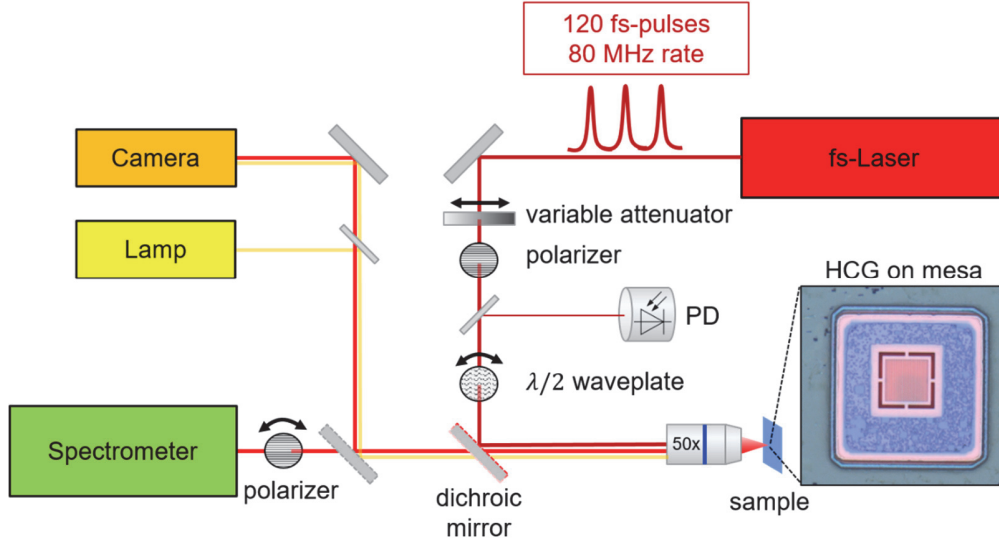
Fig. 3.1 Setup for the optical pumping experiments. Pump is a Ti-sapphire fs-laser. A variable attenuator and photodiode control power and a polarizer and lambda half wave plate control the polarization of the pump. The emitted photoluminescence (PL) light is transmitted by the dichroic mirror analyzed by a spectrometer, polarizer and camera. Lamb and camera help navigation on the sample.

As the reflectivity spectrum of the HCG mirror is expected to be highly polarization selective, it must be the first task to optimize wavelength and polarization of the pump light to effectively enter the laser cavity without being reflected by the HCG. Further, the wavelength of the pump light must be chosen, to minimize optical absorption in any of the layers above the laser cavity. Finally, the energy of the photons of the pump laser shall be reasonably close to that of the remitted photons as the resulting carrier relaxation leads to the generation of heat in the device. In Fig. 3.2 one can see the results of the optimization of pump polarization and wavelength. Part (a) of the graphic shows the detected PL spectra for TM (red) polarized pump light and TE (blue) polarized pump light of 825 nm wavelength. The expression TE is used here to describe linear polarized light with an electric field parallel to the grating bars and TM is used for light with electric field perpendicular to the grating bars. The detected PL intensity resulting from optical pumping with TE polarized light is 10 dB higher compared to the PL intensity obtained under TM pump. The wavelength of 825 nm further was found to yield the highest PL intensity at comparable power. This observation fits very well

31

considering the reflection spectrum of the HCG mirror obtained from rigorous coupled-wave analysis (RCWA) simulation as shown in Fig. 3.2 (b) based on the HCG dimensions of the device as observed under SEM. One can see that the reflectivity of the HCG for TE light has a minimum at 825 nm wavelength that allows the pump light to effectively enter the device. In contrast TM light of the same wavelength is reflected almost entirely. This finding is further confirmed by the pictures of the device under optical excitation as presented in part (c) of the figure. In the case of a TM polarized pump a bright spot of reflected light is visible on the device, where in case of the TE pump of the same wavelength no spot is observed, as nearly all of the pump light is absorbed by the device. To obtain the images a short pass filter was installed in front of the camera to block the PL light. Although based on the properties of the HCG mirror 825 nm was identified as an excellent choice for the wavelength of the pump laser for this experiment the VCSEL devices used here were designed to be electrically pumped. As a result, the structure of the laser not only featured doped layers that introduce unnecessary absorption, but even worse contained two pairs of DBR on top of the active region. While the pump wavelength of 825 nm was outside of the main reflection band of these two DBR pairs, the remaining reflectivity of these layers at 825 nm wavelength can be significant. Thus, the pump light is expected to suffer both, absorption as well as reflection before reaching the center of the cavity.
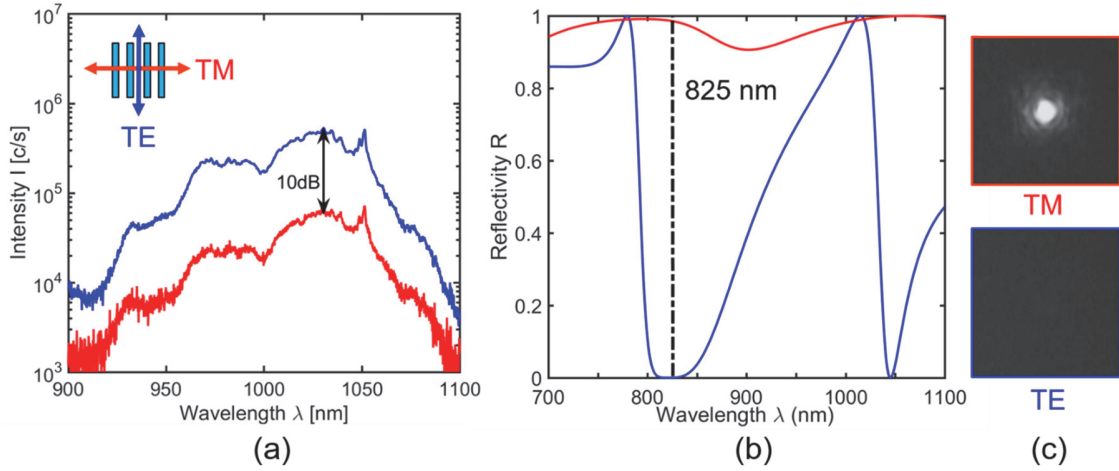
Fig. 3.2 Choice of polarization and wavelength of pump light. (a) Photoluminescence spectra of a HCG VCSEL under optical excitation with 825 nm wavelength light with TE and TM polarization with respect to the grating bars. (b) Simulation of HCG reflectivity for TE and TM light. (c) Camera image of the light of the pump laser. TM polarized pump light is strongly reflected, while TE polarized light is absorbed.

3.2   Optical pumping of HCG VCSELs

In this section results on the optically pumped lasing of HCG VCSELs are presented. First a comparison shall be made between the electrically driven and optically pumped lasing of the same device. In

Fig. 3.3 (a) the LIV characteristic of an HCG VCSEL is presented. The inset of the graph shows the lasing emission of the device. Though the voltage is quite high, the laser reaches threshold at ~2.3 mA. The same device was tested under optical excitation, with the result shown in part (b) of the graphic. Here the peak intensity of the photoluminescence spectrum is plotted as function of the (time averaged) excitation power (LL-curve). Below threshold the graph is linear in the double logarithmic plot and thus obeys the expected power law with ideality factor of $n \approx 1.3$. At ~4 mW optical pump power the device reaches threshold and the graph displays an S-shape increase in PL intensity characteristic for the threshold of an optically pumped laser, where the PL intensity increases by ~20 dB. From the observed current threshold I_{th} under electrical pumping an expected threshold for the optical pumping power P_{opt} can be estimated via the following relationship:

$$P_{opt} = I_{th}\tau R_{pulse}\frac{hc}{\lambda}\frac{A_{spot}}{A_{aperture}} \qquad \text{Eq. 3.1}$$

The equation is obtained by equating the threshold carrier densities in the quantum wells for both excitation mechanisms. Size of the focused spot of the pump light A_{spot} was estimated to be similar to the size of the oxide current aperture $A_{aperture}$ of the laser. The carrier live time τ was estimated to be on the order of 1 ns. Pulse repetition rate of the laser was given by the pump laser as 80 MHz and the wavelength λ used for the experiment was 780 nm.

(a)

(b)
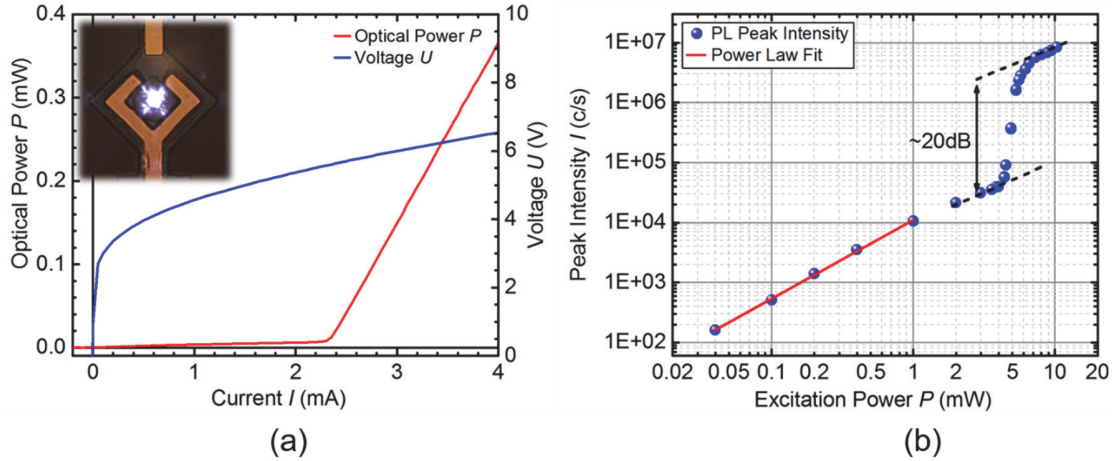
Fig. 3.3 Electrical and optical pumped lasing of the same HCG VCSEL device. (a) LIV curve and micrograph of the laser. (b) LL curve showing a characteristic s-shape, indicative for the threshold of an optically pumped laser. Below threshold the rise of the PL intensity with the power of the optical pump follows a power law with an ideality factor of 1.3.

33

The difference from the ideal wavelength found in the prior chapter may result from the presence of different HCG designs on the same chip in combination with fabrication nonuniformity of the HCG dimensions. The calculated expected optical power to reach threshold based on the above assumptions was 300 μW. This value is about 1 order of magnitude smaller than the observed threshold, but considering the strong absorption of the 780 nm pump light in the two $\lambda/4$ $Al_{12}GaAs$ layers of the top DBR, it is expected to find a significantly lower calculated value.

After having successfully demonstrated optically pumped lasing on a VCSEL with HCG top reflector. Electrically dysfunctional devices of the same wafer were tested. In Fig. 3.4 we present optically pumped lasing results of a device that suffered from an electrically open circuit. This experiment demonstrates how optical pumping can be used to close the feedback loop in research and to obtain information about their lasing characteristic from devices in cases were electrical operation is not possible due to challenges in fabrication. In part (a) of the graphic, spectra closely below (yellow), at (red) and above lasing threshold (green) are shown. The intensity of the spectra below and at threshold have been multiplied by a factor of 100x for clarity. Below threshold the spectrum is dominated by spontaneous emission centered at ~1050 nm wavelength. When the threshold is reached a lasing mode arises at 1067 nm. For higher excitation powers the intensity of the lasing mode rises quickly and dominates the spectrum taken at 1.9 P_{th}. In part (b) of the graphic the corresponding LL-curve is presented. It again follows a power law below threshold, where spontaneous emission dominates and shows the characteristic S-shaped ~20 dB increase of PL intensity at the transition to the lasing regime. The polarization of the lasing emission was analyzed by rotating the polarizer in front of the spectrometer. The result can be seen in Fig. 3.4 (c). As result of the polarization dependent reflection spectrum of the HCG reflector the lasing light is strongly polarized in TM direction. The stable linearly polarized emission in the designed direction observed here by optical pumping is in excellent agreement with the published work on electrically pumped 1550 nm devices with HCG reflector designed for TE emission [24].
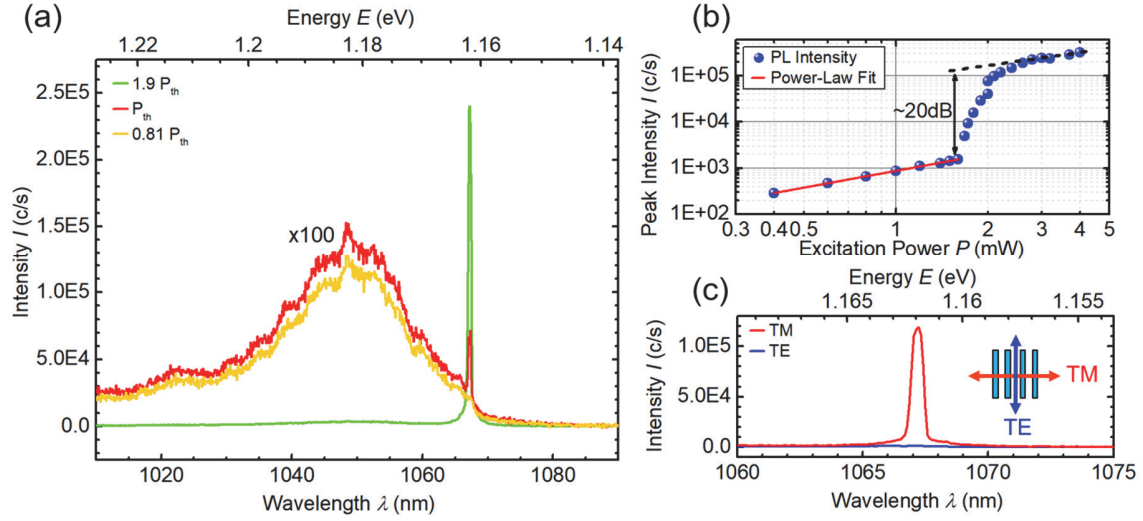
Fig. 3.4 Optically pumped lasing of an overoxidized HCG VCSEL. (a) Spectra below, at and above the lasing threshold. (b) LL curve showing the characteristic s-shape at the lasing threshold. (c) Spectra of TM and TE polarized photoluminescence light, showing the TM polarized nature of the lasing light.

As the devices in this work where designed with the top HCG mirror suspended by a micro-electro-mechanical systems (MEMS) Their cavity length can be changed electrostatically by application of an external voltage [23]. Accordingly, electrostatic wavelength tuning of the deices under optically pumped lasing operation was attempted. Fig. 3.5 (a) shows a series of lasing spectra obtained for MEMS voltages of 0 to -7 V resulting in systematic wavelength tuning over a range of 1 nm. As can be seen from part (b) of the graphic the shift in peak wavelength as function of the applied MEMS bias accelerates strongly for higher voltages. This is observation is very well in agreement with the results on the electrically operated lasers [23] and the main reason for the small tuning range observed in this experiment. Additionally, due to the lack of a dedicated experimental setup for optical pumping including satisfactory micro positioning of two electrical probes it was difficult to conduct this experiment and very few devices could be tested in the available time. Never the less, the results of the experiment prove the possibility to operate wavelength tunable HCG VCSELs optically pumped.
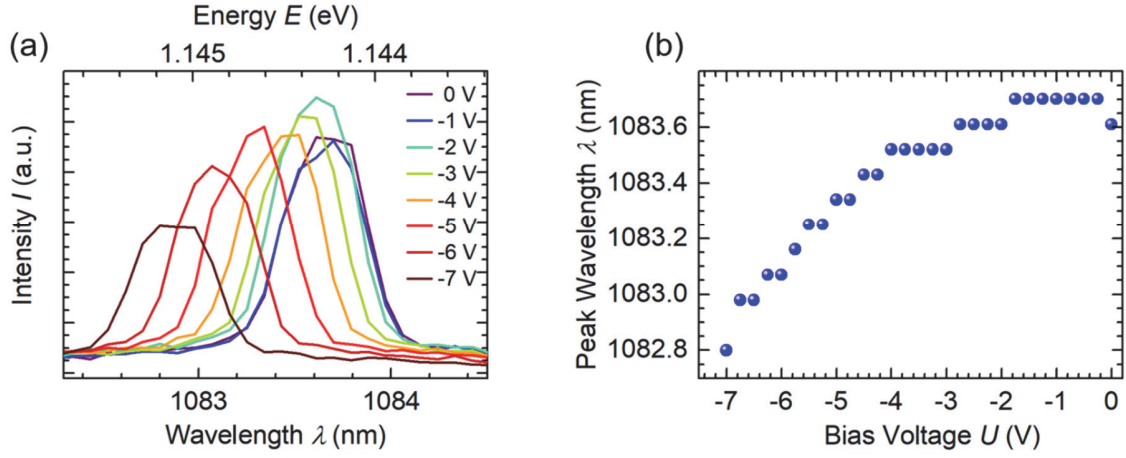
Fig. 3.5 Wavelength tuning of an optically pumped HCG VCSEL. (a) Lasing spectra showing wavelength tuning for the corresponding voltage applied to the MEMS HCG mirror. (b) Lasing wavelength as function of the applied tuning voltage.

3.3 Test structures for optical pumping

Finally, optical pumping was evaluated as a method to obtain lasing parameters from HCG VCSEL test structures with greatly reduced fabrication effort in order to shorten the turnaround time of the research cycle of epitaxy, microfabrication a testing. The application of this method could be to rapidly test different designs for the active region, the cavity and the HCG reflector of a VCSEL. Three different test structures where investigated as presented in Fig. 3.6.. Structure (a) required the fabrication of the HCG mirror, definition of mesas and oxidation of the aperture layer. In structure (b) the oxidation layer was left unoxidized. Structure (c) has the HCG mirror only. Below each structure the PL spectra of TM and TE polarized light are shown. As mentioned earlier the HCG reflector was designed for high reflectivity in TM direction, thus TM polarized lasing modes are expected to be observed. The spectra obtained from devices with structure (b) and (c) shown only weak polarization, due to the lack of lateral optical confinement. Structure (a) that includes the oxide aperture shows a strongly TM polarized mode close to lasing threshold, indicating that it is advantages to include the fabrication of the oxide aperture to evaluate the epitaxial design under optical pump. While optically pumped lasing was demonstrated on VCSELs with HCG reflector as shown in the sections before, the HCG nanostructure is sensitive to damage under high excitation powers of the pump laser. This limits the optical experiments described here severely and lead to destruction of many devices.
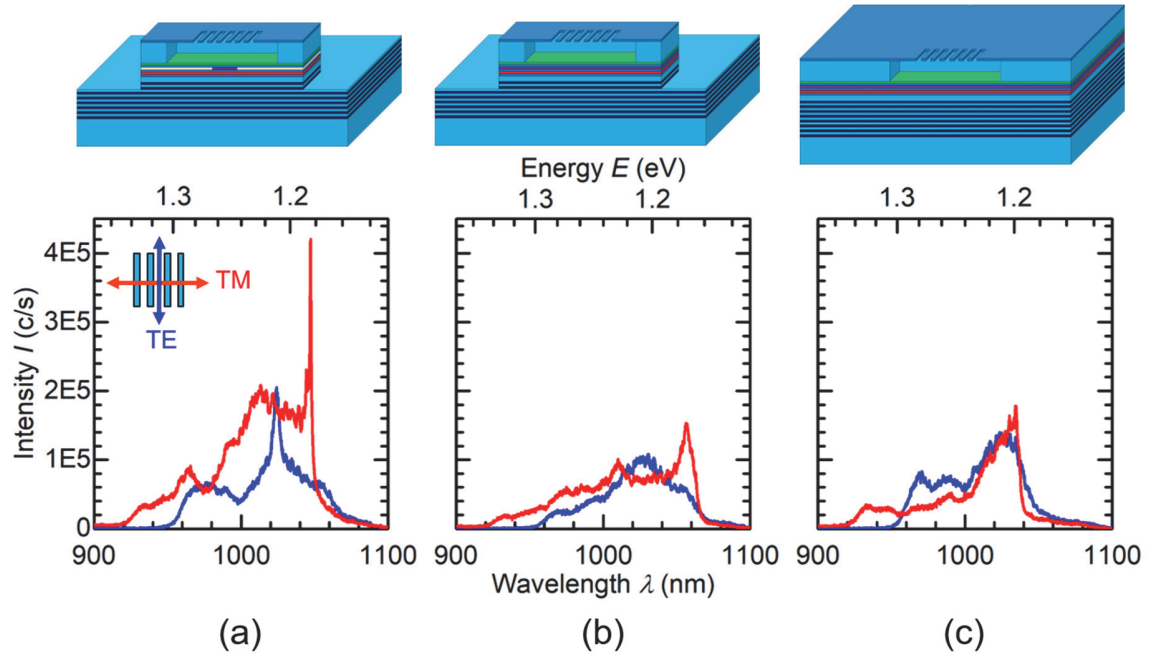
Fig. 3.6 Comparison of simplistic test structures for the short loop optical evaluation of HCG VCSEL epitaxy. (a) A VCSEL with mesa, oxidized aperture and HCG top mirror. (b) Structure without oxidized aperture. (c) Structure with HCG mirror only. The structure with mesa and oxidation aperture is necessary to observe strongly polarized modes with the potential to show lasing action.

4 Widely wavelength tunable HCG VCSEL

Wavelength tunable lasers are applied in optical coherence tomography (OCT), frequency modulated continues wave (FMCW) light detection and ranging (LIDAR) and dense wavelength division multiplexing (DWDM) systems. Realizing wavelength tunable VCSELs is particularly attractive because of their small size, low cost and their ability to be manufactured in high volume. Because of their short cavity length and the ability to integrate the top reflector with a micro-electro-mechanical system (MEMS), wavelength tuning over large ranges at kilo to megahertz sweep rates has been demonstrated [25]. The combination of a fast sweep rate with a large wavelength tuning range makes VCSELs particularly interesting for the application as swept source in OCT, where a large tuning range increases the possible depth resolution. In the following chapter a new VCSEL design with HCG as sole top reflector will be introduced and electrostatic tuning characteristic and thermal properties investigated.

4.1 Introduction to MEMS Tunable VCSELs

The concept of a MEMS-VCSEL to achieve wavelength tuning was first reported in 1995 [26]. In this type of VCSEL the MEMS actuated top mirror is separated from the cavity and bottom mirror by an air gap as shown in Fig. 4.1. As the top mirror moves up and down the length of the air cavity changes and accordingly the wavelengths of the Fabry-Perot modes. Movement of the top mirror is achieved by applying an electrical bias between top mirror and cavity top contact resulting in an electrostatic attractive force across the air gap.
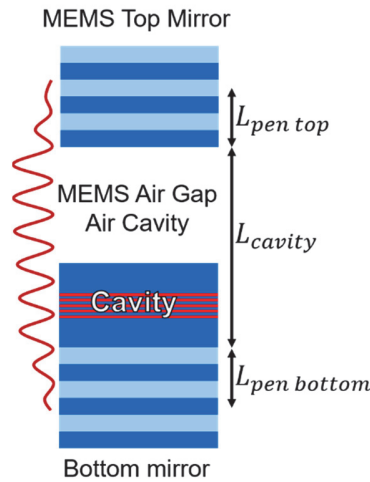
Fig. 4.1 Schematic of a wavelength tunable DBR VCSEL with MEMS actuated top mirror. The physical cavity is composed out of the semiconductor cavity with the MQWs and the air cavity. The effective length of optical cavity extends into the top and bottom mirror.

The tuning range of such a VCSEL is limited by the smallest of the ranges permitted by the following three mechanisms: (1) The limit of the mechanical movement of the MEMS mirror, which is typically about 1/3 of the air gap before pull-in happens. (2) The ability of the VCSEL to reach lasing threshold across the tuning range, which depends on the gain spectrum, mirror bandwidth and confinement factor at each wavelength. (3) The free spectral range (FSR) defined by the spacing of two adjacent Fabry-Perot modes, which defines the maximum range the wavelength can be changed before a mode hop happens. The FSR is directly related to the inverse of the effective cavity length L_{eff} which in turn is given by the sum of the length of the cavity L_{cavity} and the penetration depth of the decaying fields in the top and bottom mirrors L_{top} and L_{bottom} [27][28]. Thus, a larger FSR can be achieved by shortening the VCSEL cavity and the reducing field penetration into the mirrors. Several different architectures of MEMS VCSELs with large tuning ranges limited by FSR have been reported in literature. Devices emitting at 1550 nm based on a dielectric top DBR have been demonstrated by Gierl et al. with a thermal [29] as well as electrostatic tuning mechanism [30]. John et al. have reported a device based on a dielectric top and oxidized bottom DBR at 1050 nm [3]. Our group has investigated MEMS-VCSELs with HCG top reflector as displayed in Fig. 4.2. Here the MEMS mirror is a grating with high refractive index contrast. A variable air cavity separates the MEMS-HCG mirror from the semiconductor cavity with the active region. Our group has specifically examined the coupling between the air cavity and the semiconductor cavity which in this structure is provided by a small number of DBR pairs and the semiconductor air coupling (SAC) layer [25].
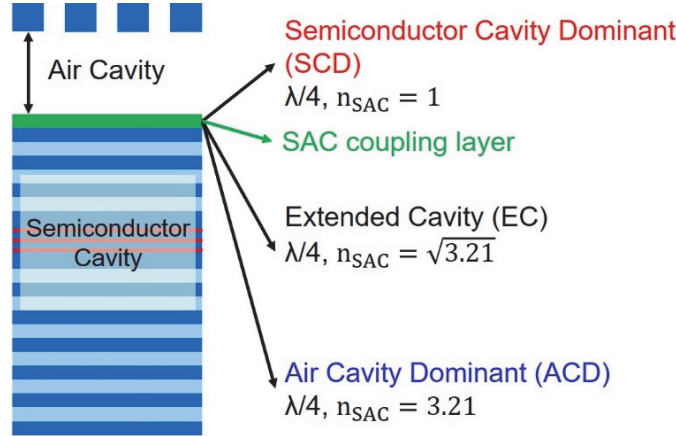
Fig. 4.2 Schematic of a wavelength tunable VCSEL with MEMS actuated HCG top mirror. Semiconductor and air cavity are connected by the semiconductor-air coupling (SAC) layer (green). Depending on thickness and refractive index of the SAC layer n_{SAC} the VCSEL design is called semiconductor cavity dominant (SCD), air cavity dominant (ACD) or extended cavity (EC) design [20].

Depending on the refractive index of a $\lambda/4$ thick SAC layer different coupling regimes can be realized. If this layer is designed to be air with refractive index of n=1 the field will be

confined strongly to the semiconductor part of the cavity. This design is called semiconductor cavity dominant (SCD) and has a low wavelength tuning efficiency as response to a given shift in the length of the air cavity as well as the lowest over all tuning range. If the SAC layer is designed as an anti-reflective coating, semiconductor and air cavity become effectively one, the tuning curve becomes linear and a larger tuning range is achieved. This is called the extended cavity (EC) design. Finally, if the SAC layer is designed with the refractive index of the semiconductor (n=3.21) an air cavity dominant (ACD) coupling regime is achieved. In this regime the tuning efficiency and over all tuning range is highest. Both SCD [23] and ACD [25] and EC [31][32] devices with HCG top reflector have been reported.

4.2   Epitaxial structure and Design

The devices reported on in this work in sections 4.2-4.6 are designed with and air cavity dominant tuning characteristic (ACD) and the entire reflectivity on the top of the device is provided by the HCG top reflector [33]. In particular, no additional DBR pairs were placed in the coupling region between the air cavity and the semiconductor cavity. The entire epitaxial structure is shown in Fig. 4.3 (a). Commercial DBR substrate centered at 980 nm wavelength was used and inhouse MOCVD growth was performed on this substrate using the GaAsP selective desorption technique referenced in section 2.4 [19]. After a 1λ thick GaAs buffer layer the active region with 5 InGaAs/GaAsP strain compensated QWs surrounded by AlGaAs claddings is grown to form a 1λ cavity. Oxidation layer, an intra cavity p-contact and a thin InGaP etch stop are grown on top of cavity. A sacrificial GaAs layer takes the place, where later the air cavity will be created. The AlGaAs HCG layer with thickness t_g concludes the structure. This layer will be patterned as a grating with the period Λ and a defined air gap. The inhouse growth effort of the HCG VCSEL structure (excluding the commercial bottom n-doped DBR) is less than 2.5 μm, enabling the growth of multiple device runs per day.
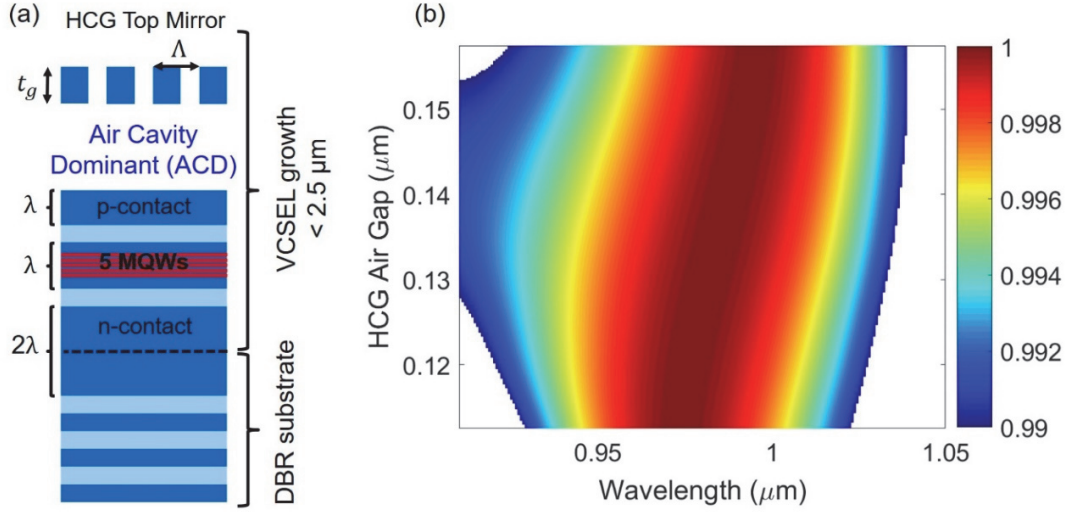
Fig. 4.3 Design of the ACD wavelength tunable VCSEL with HCG as sole top mirror. (a) Epitaxial structure. (b) Design map of the HCG top reflector demonstrating >99% reflectivity over a broad wavelength range with sufficient fabrication tolerance for the width of the air gap of the HCG.

In Fig. 4.3 (b) the reflectivity of the HCG was simulated by RCWA as a function of wavelength and air gap of the grating mirror. The plot confirms that the HCG alone is expected to provide sufficiently high reflectivity (>99%) over a bandwidth greater than 70 nm around the center wavelength of 980 nm. The width of the lithographically defined air gap of the grating has a large fabrication tolerance covering a range larger then 120 - 150 nm. The described design explicitly omits any top DRB pair, thus shortening the cavity length and thereby improving the free spectral rang. Additionally, growth time and simulation complexity of the device are reduced.

4.3   Device Fabrication

The described epitaxy was fabricated into MEMS-HCG VCSEL devices. First, the HCG was defined by e-beam lithography and SiCl$_4$ and Ar based reactive ion etch (RIE) etch. The dimensions of the HCGs where checked by SEM after the etch was completed. Hereafter a serious of photolithography steps where used with patterns as shown in Fig. 4.4. First the HCG mesa (a) was aligned to the HCG (located in the center of the design but not shown here) and etched by a piranha based wet chemical etch, which terminated on the InGaP etch stop. The InGaP etch stop itself was removed by a dip in HCL. In the second lithography step the oxidation mesa (b) was defined and a second Piranha based etch was timed to stop inside the n-doped buffer layer on top of the bottom DBR. After this step the oxidation layer was oxidized with water vapor to form current apertures with 3-5 µm target diameter. After oxidation bilayer lift-off resist was used to pattern the laser p-contact (b), the laser n-contact and the n-contact for the MEMS tuning on top of the HCG mesa (d). The named contacts as well as a n-backside contact (as backup) were evaporated of Ti and Au by electron beam

41

evaporation. Lastly, a protective layer of photoresist was applied and an opening in the HCG area was patterned to expose the HCG region for the release etch as shown in (part e). For the release of the HCG the sacrificial GaAs layer was selectively removed by a citric acid based wet chemical etch to form the air cavity. After dissolving the photoresist, the sample was dried in a critical point dryer to avoid the collapse of the MEMS-HCG mirror.
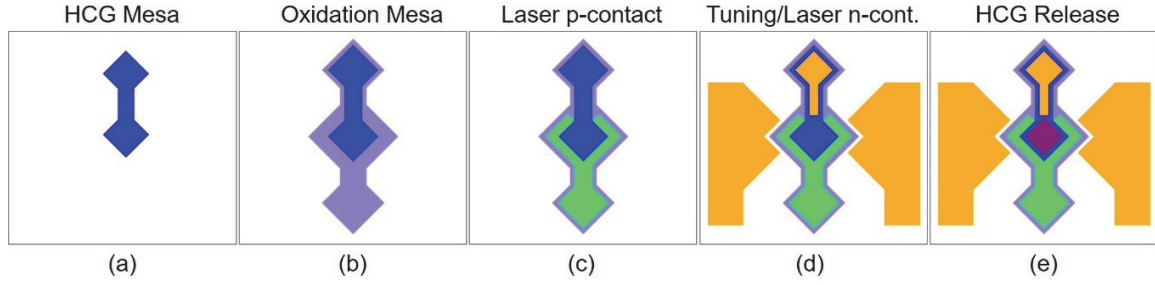
Fig. 4.4 Photolithography steps of the tunable VCSEL. After the HCG is defined by electron beam lithography in the center of the device, the HCG mesa (a) and the oxidation mesa (b) are created. The p-contact of the laser diode (c) and the n-contacts of laser and tuning diode (d) are patterned by evaporation and lift off. (e) A citric acid based etch is used to create the air cavity underneath the HCG top reflector, while the remaining parts of the device are covered by resist.

A cross section of the device after the described fabrication procedure is shown in Fig. 4.5 (a). During operation of the laser a current stimulus I_{laser} will be applied across the laser diode from the p-laser contact to the n-contact on the backside of the device. The tuning voltage V_t is applied onto the MEMS HCG mirror via the n-tuning contact and the p-laser contact. The resulting electrostatic force pulls the HCG mirror downwards, shortens the air cavity and shifts the wavelength blue. A micrograph of the real device after completed is shown in Fig. 4.5 (b), where the green dotted line indicates the position of the cross section and the MEMS HCG mirror with folded beam spring design is in the center of the device.
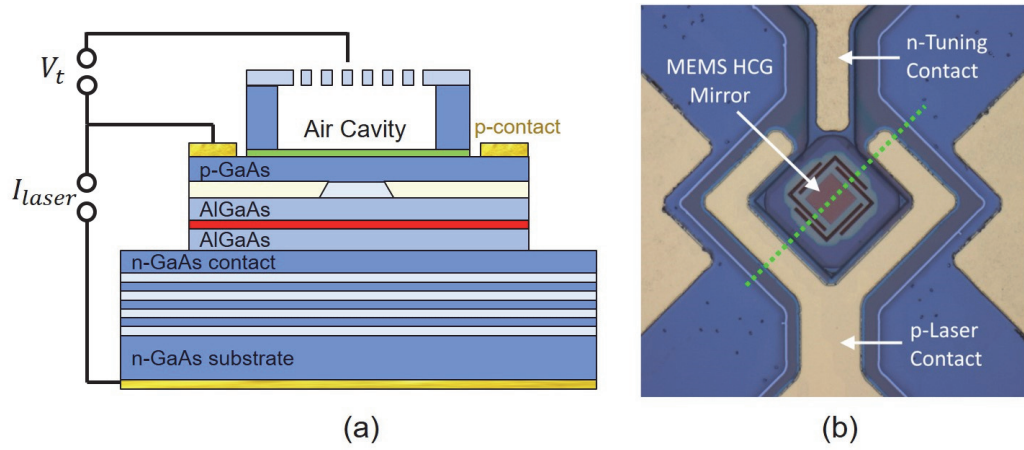
Fig. 4.5 Result of device fabrication. (a) Schematic of cross section of the wavelength tunable HCG VCSEL. Current source I_{laser} is driving the laser diode, the voltage V_t is applied to the MEMS HCG mirror to change the length of the cavity and tune the emission wavelength of the laser. (b) Micrograph of the fabricated device. The green dotted line indicates the position of the cross section.

4.4 Experimental results

The wavelength tuning range and light current curve of the devices was measured and the results are presented in this section. Fig. 4.6 (a) shows laser spectra for DC voltages 0 – 15.7 V applied between MEMS HCG reflector and p-contact. At 0 V tuning voltage the HCG mirror is at its original position and the laser emits 1001 nm wavelength. For higher tuning voltages the electrostatic force pulls the MEMS HCG mirror downwards and the air cavity is shortened. As a result, the Fabry-Perot mode of the VCSEL shifts blue for higher tuning voltages. At 15.7 V applied tuning voltage the wavelength of the laser reaches 945 nm, demonstrating a continues tuning range of 56 nm, covering almost the entire free spectral range of 59 nm. Over the entire tuning range, the VCSEL emits at room temperature under continues wave stimulus in a single mode with side mode suppression ratio (SMSR) > 25 dB. Part (b) of the graphic shows the LIV curve of the device measured towards the center of the tuning range with 14 V applied tuning voltage and the VCSEL emitting at 968 nm wavelength. A maximum power of 0.7 mW was achieved and a threshold of ~1mA. Because of the Ti-Au n-contact that acts a Schottky barrier, the device has an unusually high turn on voltage, to mitigate this problem a different contact metallurgy has to be chosen. Among others eutectic Ge-Au with Ni has been reported as a suitable choice to make ohmic n-contact on GaAs [34].
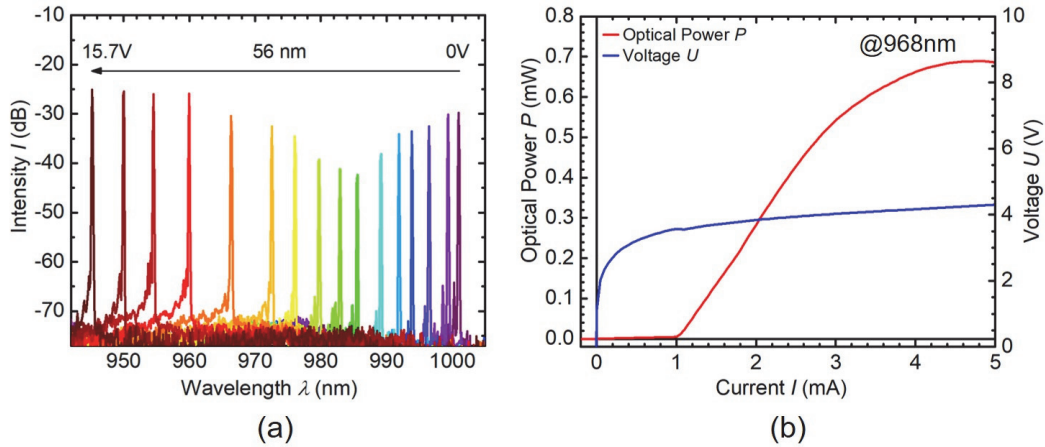
Fig. 4.6 Laser characteristics. (a) Spectra showing continues wavelength tuning under application of static tuning voltages from 0-15.7 V. Emission is single mode with SMSR >25 dB over a range of 56 nm. (b) LIV curve of the near the center of the tuning range at 968 nm with maximum power of 0.7mW and 1 mA threshold.

4.5   Air Cavity Dominant Characteristic

Although theoretically predicted by Qiao et al. [25] using transfer matrix calculations, the ACD tuning characteristic has not been explicitly studied in experiment. Since the fabricated devices in this work show an almost complete coverage of the tuning range by application of a static tuning voltage, it is possible to obtain the experimental tuning characteristic of the VCSEL, meaning the dependency of observed laser wavelength as a function of air cavity length and compare this data to the same characteristic obtained by simulation based on the transfer matrix method. The present section describes the method used to determine the experimental tuning characteristic based on a simple harmonic oscillator model for the MEMS structure. The results are compared to prediction by transfer matrix simulation. As a first step the spectrum of the tunable VCSEL is measured for tuning voltages of 0 – 15V. This data is plotted in Fig. 4.7 (a). Three longitudinal modes of the VCSEL cavity are visible in the wavelength range of 920 – 1020 nm. As the lasing mode tunes from ~1000 nm to ~947 nm wavelength with increasing tuning voltage, the mode on the blue side initially at ~940 nm decreases in intensity and shift blue out of the observed spectral range. At higher tuning voltage a mode at the red edge of the observed spectral range emerges and shifts as well. When plotting the peaks of the three observed modes as a function of the corresponding applied tuning voltages one obtains the plot in part (b) of the graphic. It is apparent that for lower values of the tuning voltage the wavelength shifts are small. For tuning voltages in the range of 10 – 15 V the observed wavelength change accelerates quickly. This behavior is the result of two separate mechanisms: (1) Displacement of the MEMS reflector for a given voltage. (2) The change of wavelength of the laser for a given length of the air cavity.
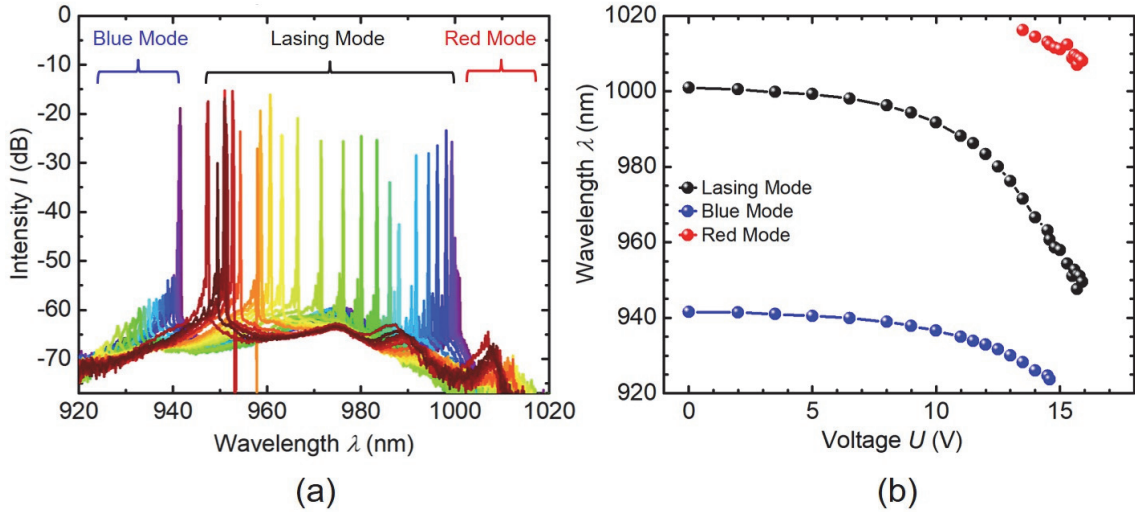
Fig. 4.7 Static tuning characteristic. (a) Spectra for a range of static voltages applied to the tuning diode. Three different longitudinal modes of the laser can be observed. (b) Emission peak of the three modes plotted as function of the applied tuning voltage.

In the following the first aspect is calculated by assuming a harmonic oscillator model for the MEMS reflector. Once the displacement of the top reflector for a given voltage is known the change of wavelength as function of the air cavity length can be determined, which is characteristic for the coupling regime of semiconductor and air cavity, namely SCD, EC or ACD type coupling. In order to model the MEMS mirror movement its resonance frequency has to be determined. A small AC signal of constant amplitude is applied to the MEMS reflector and the time averaged laser spectrum is measured while the frequency of the AC signal is step wise increased from 20 kHz to 2 MHz. The spectra for the different AC frequencies driving the MEMS reflector can be seen in Fig. 4.8 (a). For an AC voltage of constant amplitude and different frequencies the spectra display varying sweep ranges in the emission wavelength. Part (b) shows the normalized wavelength change of the sweep as function of the frequency of the AC voltage driving the MEMS mirror. A MEMS resonance frequency of $f_R = 345$ kHz and a -3dB-frequency of $f_{-3dB} = 687$ kHz is found. Next the force constant k of the MEMS HCG mirror was calculated with $k = m \, (2\pi f_R)^2$, assuming a harmonic oscillator. The mass m of the mirror was calculated based on the geometry and the density of the AlGaAs alloy of the MEMS HCG mirror.
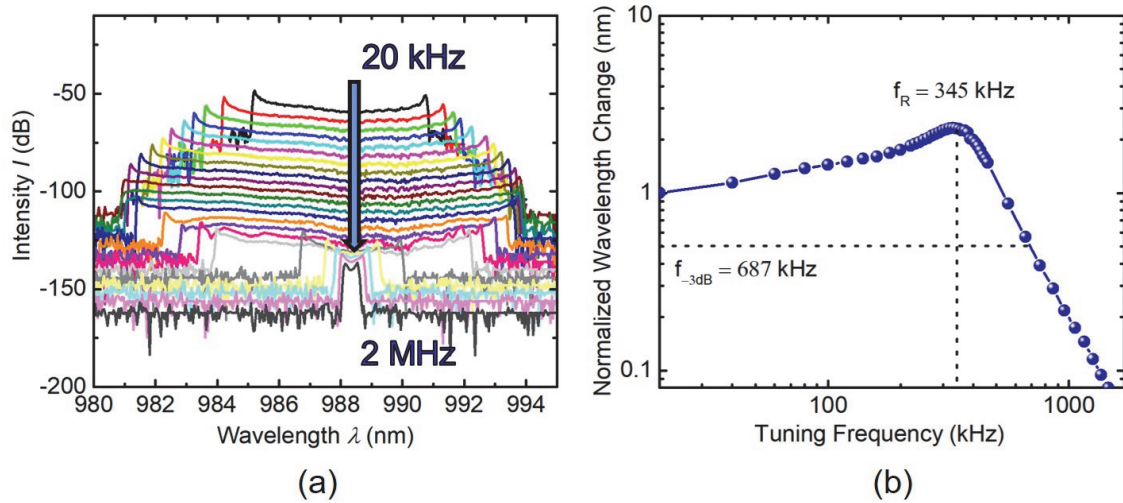
Fig. 4.8 Measurement of the resonance frequency of the MEMS HCG reflector. (a) Laser spectra for different frequencies of AC voltage applied MEMS mirror. (b) Tuning bandwidth as function of the applied MEMS frequency (extracted from a). Measured resonance frequency f_R and -3 dB frequency f_{-3dB} of the MEMS HCG reflector are indicated.

The air cavity length d was calculated as function of the applied tuning voltage V, based on the equilibrium point of electrostatic force F_{el} and spring force F_{MEMS} acting on the MEMS mirror. This situation is shown in the schematic in Fig. 4.9 (a), where the d_0 denotes the length of the air cavity at 0V tuning voltage. From equating the electrostatic and spring force one obtains the following expression:

$$\frac{\epsilon_0 A V^2}{2d^2} = k(d_0 - d) \qquad \text{Eq. 4.1}$$

As solution to this nonlinear equation one obtains the length of the air cavity d as function of the applied tuning voltage V as plotted in Fig. 4.9 (b). At zero applied voltage the length of the air cavity is d_0 as expected. With rising voltage, the decrease in the length of the air cavity accelerates until a pull in point is reached at ~16 V, here the MEMS mirror collapses and the air cavity length becomes zero. The calculated pull-in voltage is in excellent agreement with the experimentally observed pull-ins of the measured devices. The bullets of the plot correspond to the values of the tuning voltages at which the spectra shown in Fig. 4.7 (a) where measured.

(a) (b)
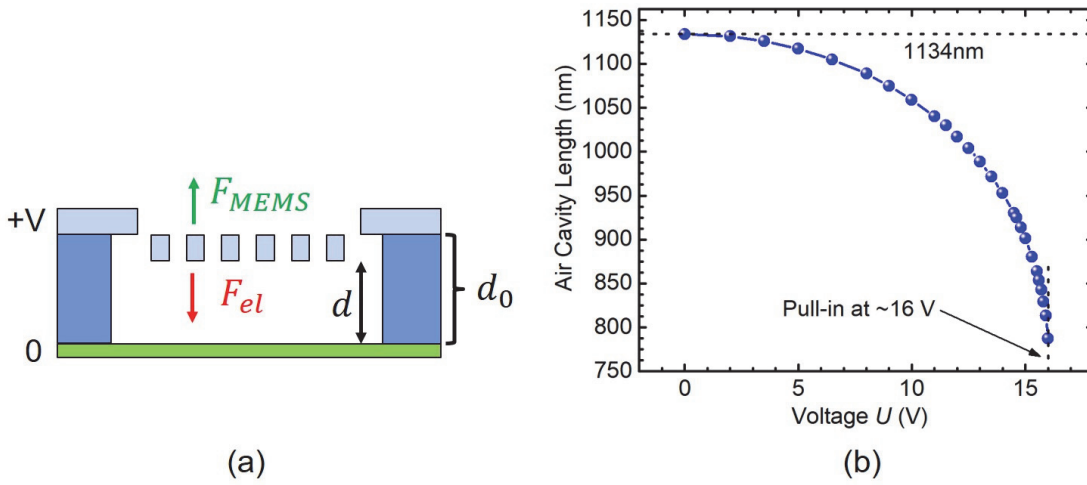
Fig. 4.9 Harmonic oscillator model of the MEMS HCG reflector. (a) Equilibrium of spring force and electrical force crated by voltage V across the reverse biased tuning diode leading to length of the air cavity d. (b) Calculated length of air cavity as a function of the applied tuning voltage. At 0 V the cavity length equals to d_0, at voltages ~16 V the MEMS mirror collapses.

Combining the information of Fig. 4.7 and Fig. 4.9 (b) one finally obtains the emission wavelength of the laser as a function of the air cavity length as plotted in Fig. 4.10 (a). The bullets show the experimental data and the lines the tuning characteristic obtained by transfer matrix simulation as reference. Both shape and absolute position of the experimentally obtained tuning curves are in good agreement with the characteristic predicted by simulation. Typical for the air cavity dominant design the tuning efficiency of the laser is greatest at the center of the tuning range, here at about 970 nm wavelength. Towards the edge of the tuning range the tuning efficiency decreases for the ACD design. Additionally, the separation between adjacent Fabry-Perot modes (FSR) is largest at the edge of the tuning range and smallest at the center. In comparison to this result, devices with SCD characteristic as published by K. Li [23] where analyzed in an equivalent way. The result is shown in part (b) of the graphic. This tunable laser shows a transverse mode hop at an air cavity length of ~

47

1040 nm, which marks the edge of the continues tuning range. The center of the tuning range is located at an air cavity length of ~1300 nm. Although not the entire tuning range of this device was accessible by applying an electrostatic bias, one can clearly see the fundamental difference of the tuning characteristic in comparison to the ACD device. While the tuning efficiency at the center of the continues tuning range at ~1085 nm is lowest it increases towards the edges of the continues tuning range where the mode hop takes place, namely at ~1065 and ~1095 nm wavelength. This is characteristic for the SCD coupled cavity regime. In summary wavelength tunable MEMS HCG VCSELs both with ACD as well as SCD coupled cavities have been investigated in this section and the experimentally derived tuning characteristics in both cases correspond well to the predictions made by transfer matrix simulation.
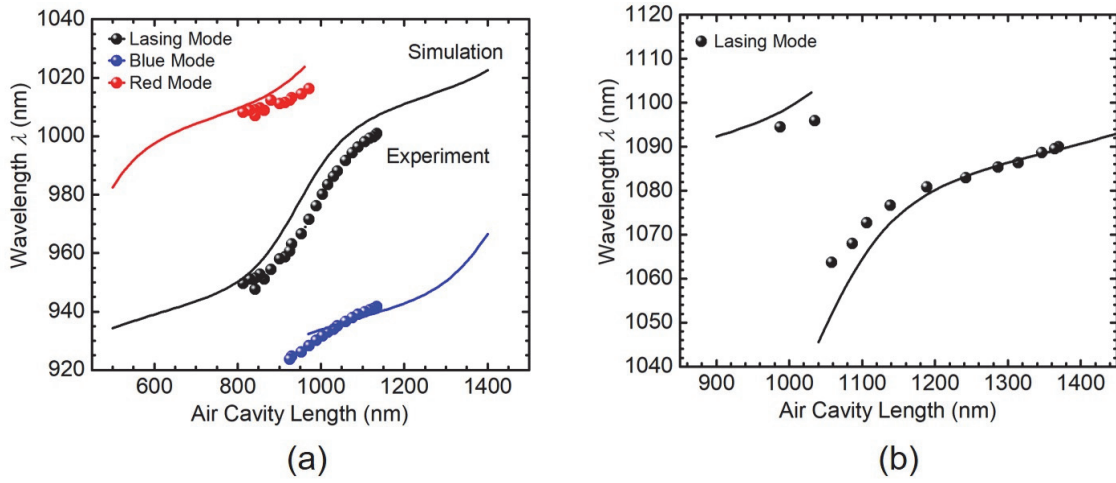
Fig. 4.10 Comparison between experimental data (bullets) and transfer matrix simulation (solid lines) (a) for a device with air cavity dominant tuning characteristic and (b) for a device with semiconductor dominant tuning characteristic.

4.6 Thermal Characterization of the HCG VCSEL

In this section the thermal properties of the MEMS-HCG VCSEL are investigated. Operation in an environment of elevated temperature is tested and the thermal resistance is determined from the spectral shift of the lasing mode with changing temperature of the heat sink and under varying operation current. All measurements in this section were obtained at 0 V tuning voltage. In Fig. 4.11 (a) the light current voltage (LIV) characteristic of the laser is shown for heatsink temperatures from 20 – 50°C. While the voltage shows no significant change with temperature both optical power decreases and threshold of the devices rises until the laser no longer reaches threshold above 50°C. In part (b) of the graphic this observation is plotted explicitly. The sharp rise in threshold current with rising temperature indicates that the off-set between the maximum of the gain spectrum and the cavity mode can be increased in order to improve the laser characteristics at elevated temperature as well as under high current operation. Because the gain spectrum of the QW shows a faster red shift with rising temperature then the cavity mode in a VCSEL the gain peak is designed blue shifted with respect to the cavity mode at room temperature. As the temperature rises (either due to elevated external temperature or internal heating) the maximum of the gain peak gets to match the wavelength of the cavity mode and the optimum operation point of the VCSEL is reached. Thus, our analysis suggests to increase the gain offset in order to improve the VCSELs performance.
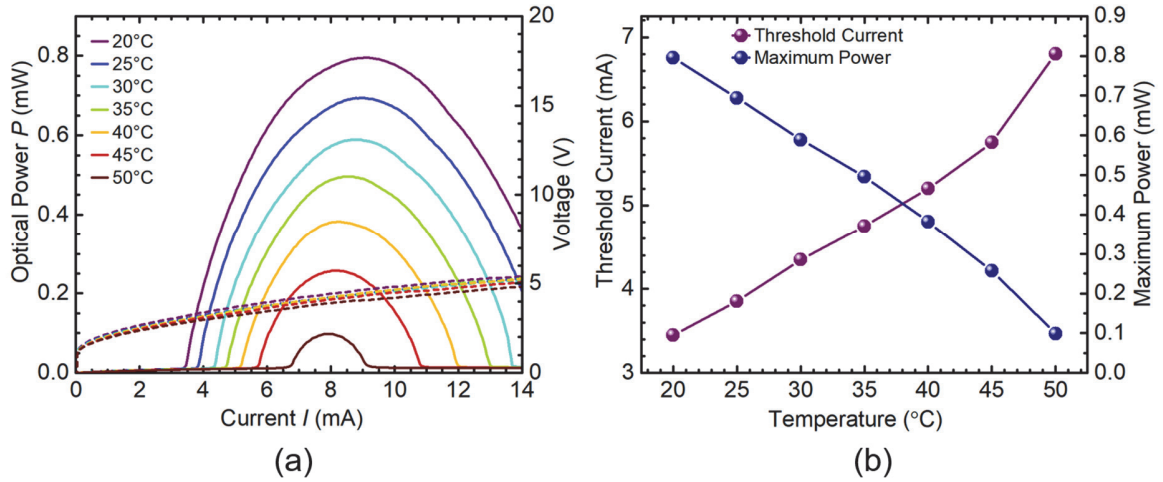
Fig. 4.11 (a) LIV measurement of the wavelength tunable HCG VCSEL for heatsink temperatures of 20 – 50°C. (b) Threshold current increases and maximum power decreases with rising temperature.

An important measure for the thermal characteristic of the VCSEL is its thermal resistance R_{th}. The value describes how much the device temperature increases or decreases (ΔT) in response to a given change of dissipated thermal power ΔP. Thus, the smaller the thermal

resistance of the device the lower its temperature rise at high current operation. The thermal resistance is calculated as follows:

$$R_{th} = \frac{\Delta T}{\Delta P} = \frac{\Delta \lambda}{\Delta P} \frac{\Delta T}{\Delta \lambda} \qquad \text{Eq. 4.2}$$

Eq. 4.2 presents a convenient way how to experimentally determine the thermal resistance by measuring the wavelength shift $\Delta \lambda$ of a given laser mode in response to (1) a change in the temperature of the laser and (2) a change in dissipated thermal power inside the device. The results of both measurements are presented below. For the first, the VCSEL is operated at a constant current (and voltage) and the temperature of the heat sink is systematically changed. Fig. 4.12 shows the spectra measured at heatsink temperatures of 20 – 50°C. The inset in the top left corner of the graph describes how the wavelength of the lasing modes changes as function of the heat sink temperature. A slope of the shift of $\Delta \lambda / \Delta T = 0.077$ nm/K is obtained by linear fit. This value fits well in the range of 0.06 – 0.08 nm/K reported in literature [15].
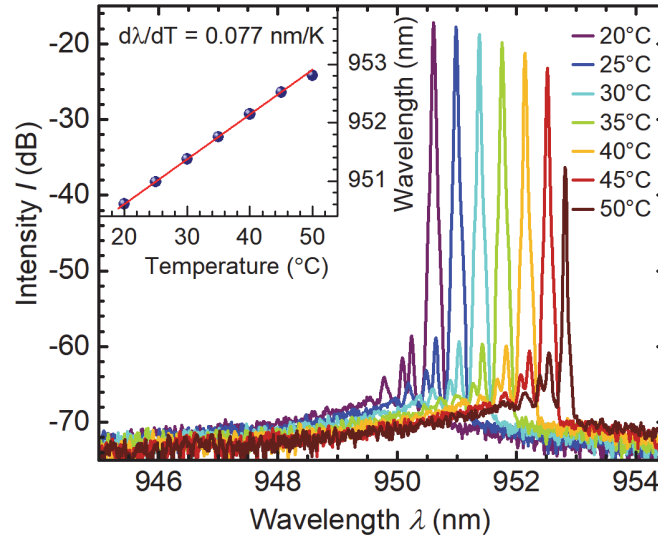
Fig. 4.12 Laser spectra of the wavelength tunable HCG VCSEL at heatsink temperatures from 20 – 50°C. The wavelength of the laser emission shifts red with 0.077 nm/K for rising temperatures.

The second measurement is conducted at constant heat sink temperature of 20°C. The laser current is increased step wise from 3 mA to 14 mA and the emission spectra are measured with an optical spectrum analyzer. The results of this measurement are shown in Fig. 4.13. When the wavelength of the optical mode is plotted as a function of the dissipated thermal power (current multiplied by the corresponding bias voltage minus the optical power) a linear relationship is found. This is shown in the inset in the top left corner of the graph. As the slope of a linear fit $\Delta \lambda / \Delta P = 0.095$ nm/mW was determined. Thus, the thermal resistance of the MEMS HCG VCSEL is 1.23 K/mW. This value is lower compared to typical oxide

50

confined VCSEL with aperture diameter of ~4 - 5µm [35][36], but higher compared to the results of the SCD MEMS HCG VCSELs measured by K. Li. et al. [23] The low thermal resistance of the device may be a result of the substitution of the top DBR by the HCG mirror and the presence of a 2λ thick binary GaAs layer under the active region. As binary GaAs material has a much higher thermal conductivity compared the ternary AlGaAs alloys used in DBRs [37].
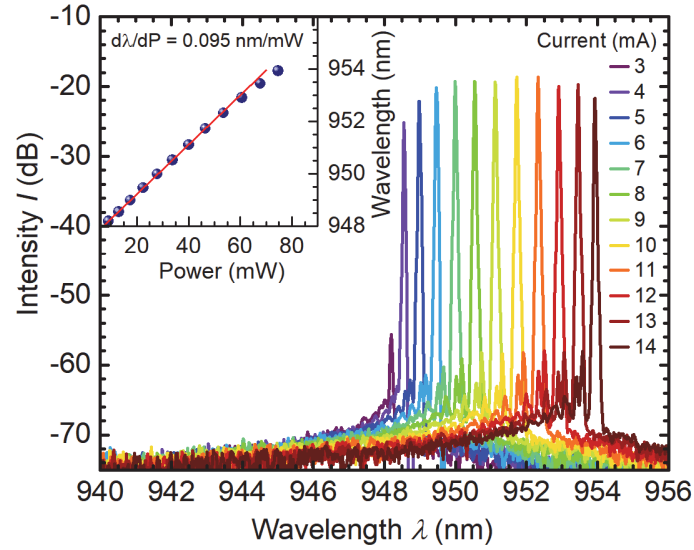
Fig. 4.13 Laser spectra of the wavelength tunable HCG VCSEL for driving currents from 3 – 14 mA. The increased internal heating for larger currents results in a red shift of the laser emission of 0.095 nm/mW. The measured thermal resistance of the device is therefore 1.23 K/mW.

5 Tunable HCG VCSEL with Buried InGaP Aperture

VCSELs with native oxide current confining aperture [38] as described in the previous sections of this thesis are the working horse for both devices for short range data communication as well as optical sensing. For applications in both areas VCSELs emitting in a single gaussian transverse mode could provide significant performance improvements. These devices show a narrower beam divergence, narrower spectral widths and allow for faster modulation speed and transmission of data through optical fibers over longer distances compared to multimode devices [39]. Single mode, continuously tunable devices can be applied as sources for swept-source OCT. The main limiting factor for single mode devices is their lower optical power. In oxide VCSELs the optical mode is confined by the strong index contrast provided by the oxidation aperture. To guarantee single transverse mode emission the aperture diameter of the VCSEL must be kept small [40][41] and to weaken the optical confinement a single thin oxide layer is placed in the node of the electric field inside the VCSEL. As a result of the requirement for a small current aperture, the resistance of single mode VCSELs is higher and their optical output power lower than multimode devices with larger aperture diameters. This section introduces a device with a buried InGaP aperture defined by photolithography and a MEMS HCG top reflector that allows for wavelength tuning. The lower refractive index contrast of the InGaP aperture material allows single mode emission of devices with larger current apertures. This makes the approach promising for single mode VCSELs with higher optical power. A second advantage is that reliability concerns related to the porous aluminum oxide in conventional VCSELs are avoided by using InGaP semiconductor as aperture material. The use of InGaP as current confinement layer also promises devices with low thermal resistance. Finally, by using a lithographically defined current apertures optimum control of the aperture shape is possible and aperture arrays with high density and freedom of design can be expected.

5.1 Epitaxial Regrowth Process

The buried InGaP current aperture is created by a regrowth process as described in Fig. 5.1. During the first MOCVD growth step shown in part (a) of the graphic the active region was grown on commercial n-doped DBR substrate. After selective desorption of the GaAsP cap layer of the substrate [19] the n-doped GaAs buffer layer is grown. Next, the active region with three InGaAs/GaAsP strain balanced MQWs and $Al_{30}GaAs$ claddings is realized and concluded with a layer of p-doped GaAs. Finally, the n-doped InGaP aperture layer is grown which concludes the first growth step. To define the current apertures, photolithography and a wet chemical etch based on HCL was used to remove the InGaP layer selectively over GaAs. This is shown by the cross section (b) in the figure. After cleaning the sample thoroughly, the top part of the cavity is regrown on the aperture pattern. First, a p-doped GaAs contact layer is deposited followed by an InGaP etch stop. After the etch stop the sacrificial GaAs layer that will be removed to form the air cavity of the tunable laser and the AlGaAs HCG layer are

grown. As indicated in Fig. 5.1 (c) the regrowth of the top layer did follow the topology of the etched apertures in a conformal way. As a result, the HCG reflector has a convex shape in the area of the current aperture.
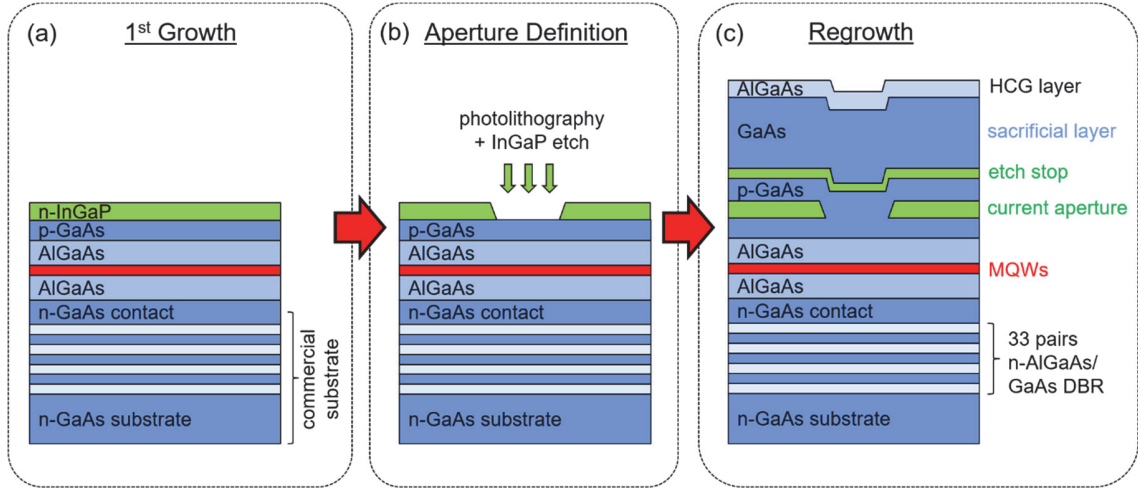
Fig. 5.1 Epitaxial regrowth concept of the HCG VCSEL with current aperture defined by a buried InGaP heterostructure. (a) In the first growth n-GaAs contact, active region and n-InGaP current aperture layer are created. (b) The current apertures are patterned by photolithography and HCL based wet chemical etch. (c) Regrowth of the p-GaAs contact layer, an InGaP etch stop, the sacrificial GaAs layer and the AlGaAs HCG layer is performed.

In any epitaxial regrowth process the crystal quality of the regrown material is of primary concern. The presented structure has the advantage that the active region, which has the highest requirement in terms of material quality, was grown during the first growth step and thus its material quality is not influenced by the regrowth process. Never the less transmission electron microscopy (TEM) was used to examine the regrowth interfaces in the aperture region. The cross-sectional images obtained by TEM are shown in Fig. 5.2. The left side of the graphic shows the cross section of the aperture region at large. High resolution details of the two regrowth interfaces are presented on the right-hand side of the graphic, both the GaAs-GaAs and the GaAs-InGaP interfaces are shown. In both images the regrown GaAs material shows a uniform, regular crystal lattice without any dislocation defects, testifying the high crystal quality of the regrowth material. The ~5 nm thick faint, bright line along the GaAs-GaAs regrowth interface was analyzed by EDX and was found to contain indium and phosphorous traces. This may be explained by the presence of a composition gradient at the InGaP-GaAs interface grown during the first growth step. However, this did not negatively influence the regrowth quality.
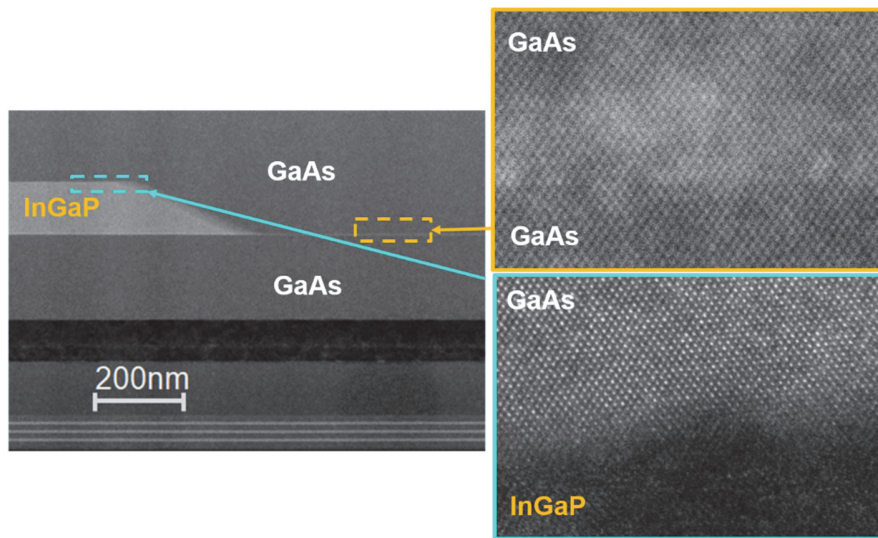
Fig. 5.2 Transmission electron microscope (TEM) pictures showing the cross section of the current defining InGaP aperture. Detailed high-resolution images of the regrowth interfaces GaAs-InGaP (light blue) and GaAs-GaAs (yellow) show a regular crystal lattice free of dislocations.

5.2   VCSEL Fabrication

After regrowth of the top part of the laser cavity on the InGaP aperture pattern wavelength tunable MEMS VCSEL were fabricated. The fabrication process used was mostly similar to the one for the devices described in 4.3. However, a few differences were made. The process started with the definition of dumbbell shaped HCG mesa by photolithography and piranha based etch, which was aligned to the regrown aperture pattern. The etch InGaP etch stop was removed by an HCL dip. Hereafter, the main mesa was patterned. In contrast to the procedure for the tunable VCSEL of chapter 4 a three-step wet chemical etch procedure had to be used. First, the p-GaAs contact layer was etched by diluted piranha, then the InGaP aperture layer was etched using HCL, finally dilute piranha was used again to complete the mesa etch down to the n-contact GaAs layer. Since the aperture of the device was lithographically defined by the buried InGaP aperture no oxidation process was necessary. Next, bilayer resist was patterned for lift-off after the evaporation of the Ti-Au front and backside contacts. After completing the described steps, the devices were tested as LEDs to confirm the electrical properties of the buried heterostructure aperture (results shown in the next section 5.3). After the measurements the VCSEL processing was continued with the patterning of the MEMS HCG mirror. Since the HCG patterns needed to be aligned to the aperture pattern by electron beam lithography and metal alignment marks created during the contact evaporation steps provide higher visual contrast then the alignment marks of the regrown pattern, this step was done after the contacts for the buried aperture of devices. As the last processing step the sacrificial GaAs layer was removed in the area underneath the HCG patterns to create the air cavity. Critical point drying was employed to prevent the MEMS from collapse. In Fig. 5.3 the results of the fabrication process are shown. Part (a) shows a schematic of the cross section of the device along the green dotted line in the micrograph in part (b) of the graphic. Fig. 5.3 (c) Shows a 30° tilt view image of the RIE etched HCG pattern before the release of the MEMS.
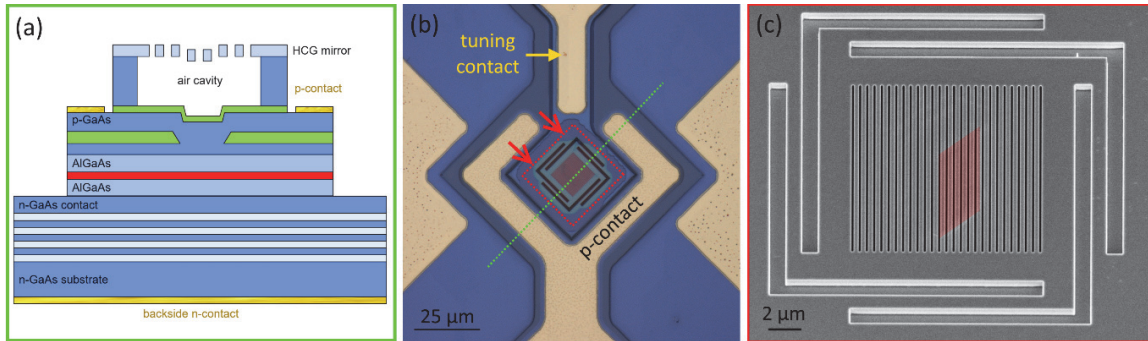
Fig. 5.3 Result of the device fabrication. (a) Cross section of the wavelength tunable HCG VCSEL with buried InGaP aperture. (b) Micrograph of the device. The green dotted line indicates the position of the cross section in a, the red dotted square indicates the area and direction of view of the detail in c. (c) Scanning Electron Microscope (SEM) image acquired under 30° tilt, showing the HCG region of

55

the same device before etch of the sacrificial layer. Highlighted in red is the depressed area of the HCG mirror due to regrowth.

The red highlighted area on the HCG in the SEM image indicates the location of the buried aperture, which leads to the depressed topology of the HCG mirror. The same is faintly visible in the micrograph in (b). Here the red dotted box indicates the area of the SEM image in (c) and the two red arrows the direction of the tilt view.

5.3   Current confinement properties of the buried InGaP aperture

To test the current confining properties of the buried InGaP heterostructure the devices were measured as LEDs before the MEMS HCG mirror was fabricated. Results of these measurements are shown in this section. Fig. 5.4 shows the LIV characteristic of one LED device with buried InGaP aperture obtained by contacting the p-top contact and the n-backside contact of the device. On the left side of the graphic micrographs of the device are shown. The top image is taken at 0 mA current stimulus. The small spot in the center of the device is due to the depressed topology in the area above the regrown aperture. Under 5 mA current stimulus bright electroluminescence is visible in this aperture area indicating effective confinement of the current by the buried InGaP aperture. The light current voltage curve is shown on the right side of the graphic. At 5 mA the LED reaches a measured output power of 12 μW and at a voltage of 2.5 V. Considering the non-ideal choice of Ti-Au as metal for the n-contact that results in the presence of a Schottky barrier, this measured voltage is reasonable.
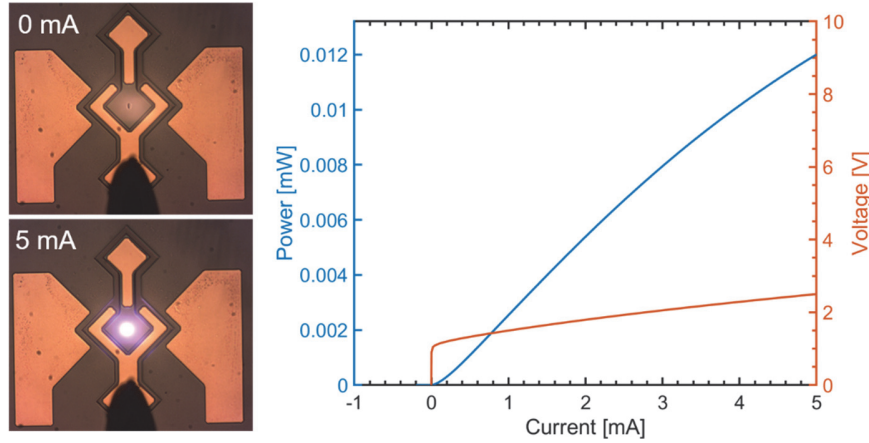
Fig. 5.4 Current confinement by InGaP buried heterostructure (BH). (Left) Microscope images of the LED device (based on the VCSEL structure before the HCG had been) demonstrating the confinement of current by localized electroluminescence in the aperture region. (Right) LIV curve showing operating voltage ~2.5 V and spontaneous emission of the LED.

Besides the low resistance in the aperture region the current blocking by the reverse biased InGaP-GaAs junction is tested. A device without etched aperture was measured to obtain this

characteristic. As can be seen in the current voltage curve of Fig. 5.5, in the device without etched current aperture the n-doped InGaP heterostructure serves as an effective current barrier. Under forward bias of the LED junction (0 – +10V) the current though the entire area of the main mesa does not exceed 1 μA up to a voltage of 10 V and no electroluminescence was observed. Since the LED with aperture presented earlier in this section operates at a voltage of ~2.5 V, the current leakage through the InGaP current confining layer is not expected to exceed 1 nA. Thus, it can be concluded that the lithographic current aperture based on the InGaP buried heterostructure is an effective method of confining the current in a VCSEL device.
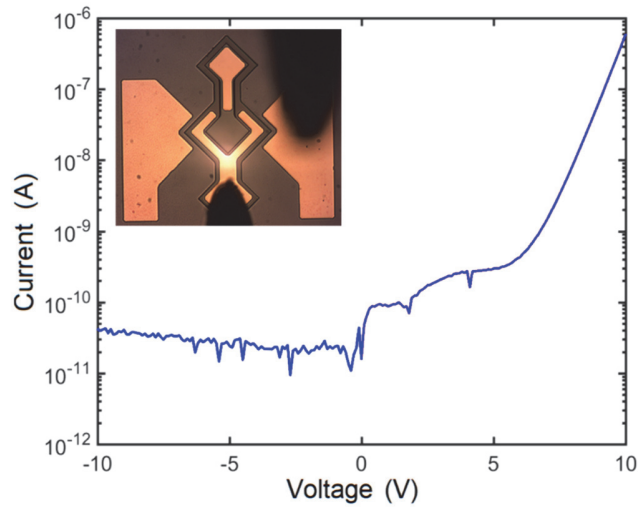
Fig. 5.5 Current blocking characteristic of the InGaP buried heterostructure. A device (based on the VCSEL structure before the HCG had been fabricated) without etched aperture region shows leakage currents < 1μA under forward bias of the (laser) diode.

5.4 Sigle mode wavelength tunable VCSEL with large aperture

In the following the results of the wavelength tunable MEMS HCG VCSEL with buried InGaP heterostructure as current aperture are discussed. Fig. 5.6 shows the basic laser characteristics. This device was designed with square 6 μm diameter aperture and the data was taken at 14 V tuning voltage. The spectrum in part (a) of the figure shows single transverse mode emission with side mode suppression ratio (SMSR) ~37 dB and was obtained at 13 mA continues wave current and heatsink at room temperature. The corresponding LIV characteristic is presented in exhibit (b). The voltage is on the high side as a result of the non-ideal Ti-Au backside n-contact. The device shows a high threshold of 6.7 mA and reaches an output power of ~0.1 mW. The low power and high threshold of the devices is plausibly related to the scattering loss that results from the convex topology of the HCG reflector in the aperture region. An indication of this explanation is the prominent broad emission in the spectrum and the visible subthreshold optical power stemming from spontaneous emission leaking through the corrugated top reflector. This feature can be avoided by optimizing the regrowth condition do allow for a higher rate of lateral diffusion during the regrowth and as a result a higher lateral growth rate. Another approach could be to split the micron size aperture into multiple smaller apertures so the lateral distance to be covert to reach planarization during regrowth is smaller. Initial experiments of regrowth on grating patterns with gaps of ~400 nm showed promising results with respect to planarization.
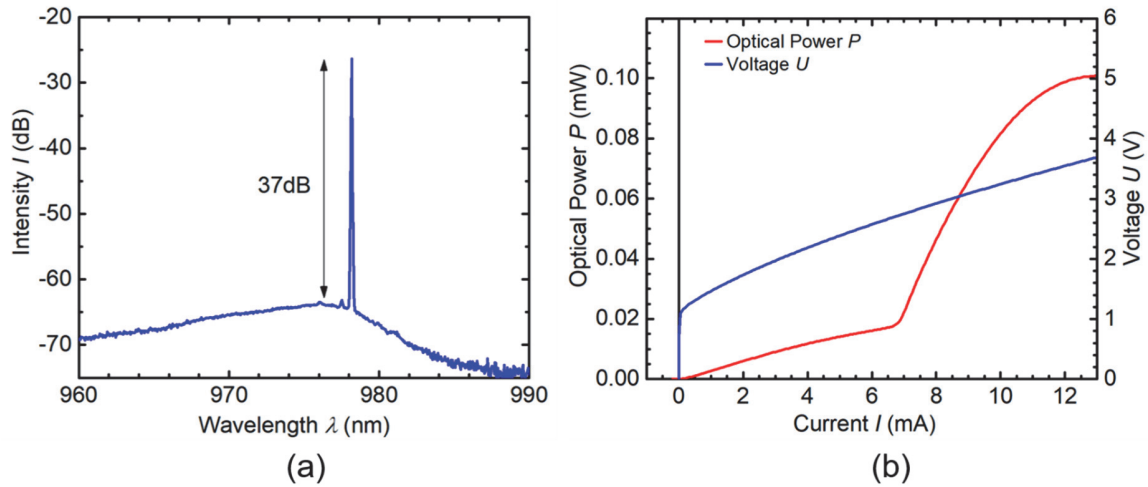
Fig. 5.6 LIV and Spectrum of a HCG VCSEL with buried InGaP aperture. (a) Single mode lasing spectrum with side mode suppression ratio (SMSR) of 37 dB. (b) LIV curve of the same laser with 6.7 mA threshold and ~0.1mW output power obtained at room temperature continues wave operation.

Different aperture shapes and sizes where studied with regards to their single mode emission characteristic. Single mode emission of devices with large apertures and excellent SMSR was demonstrated. In particular devices with triangular, circular, rectangular, square and diamond

58

shape apertures where fabricated. Devices with all aperture shapes did show lasing emission and apertures as large as 5-7 μm showed single mode lasing emission. The spectra and aperture shapes and sizes of the corresponding devices are shown in Fig. 5.7. The wide spread of lasing wavelength observed results from the inhomogeneity and edge effects of the epitaxy on the 1x1 cm sized chip as well as the variety of HCG designs that were used for the devices. In summary, it can be said that the low refractive index contrast of the buried InGaP aperture promotes single mode lasing emission for large aperture devices, proving this approach potentially promising for higher power single mode VCSELs.
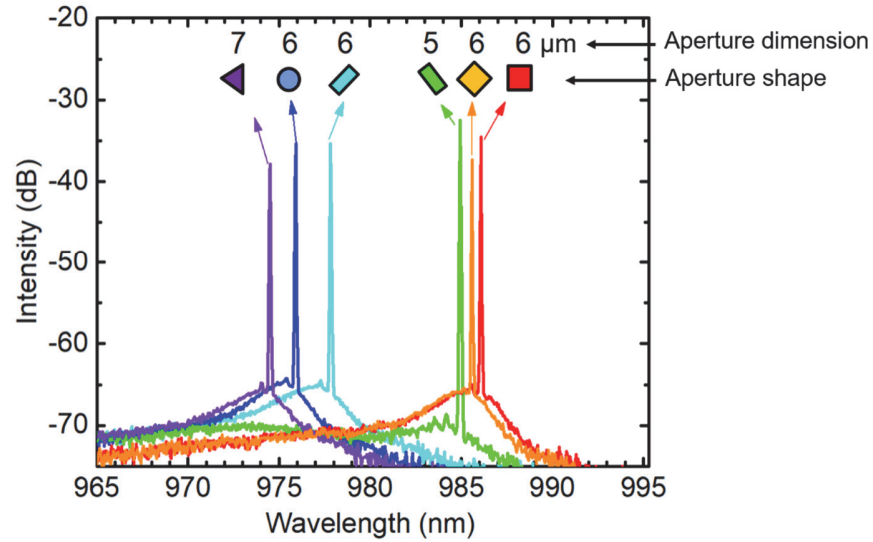
Fig. 5.7 Single mode lasing spectra obtained at room temperature continues wave operation from a series of HCG VCSELs with buried InGaP apertures of the various indicated aperture geometries and sizes.

As the fabricated lasers featured a MEMS HCG mirror for electrostatic wavelength tuning, different voltages (0 – 15 V) were applied to the tuning contact and the laser spectrum was measured. The results can be seen in Fig. 5.8.. The laser starts to emit on the blue edge of the tuning range and with increasing tuning voltage from 0 V to 10 V the wavelength of the lasing mode shifts further blue and the device stops lasing. At higher voltages of 14 – 15 V the next cavity mode with longer wavelength starts lasing and a continues tuning range of 6.6 nm is observed with SMSR > 25dB. The tuning range of this device in contrast to the earlier discussed tunable VCSEL of chapter 4 is not limited by the free spectral range. The main limiting factor instead here is that the laser fails to reach threshold as a result of the large scattering loss through the corrugated top mirror. With a planar top mirror, it can be expected that the device shows continues, single transverse mode wavelength tuning covering the full free spectral range.
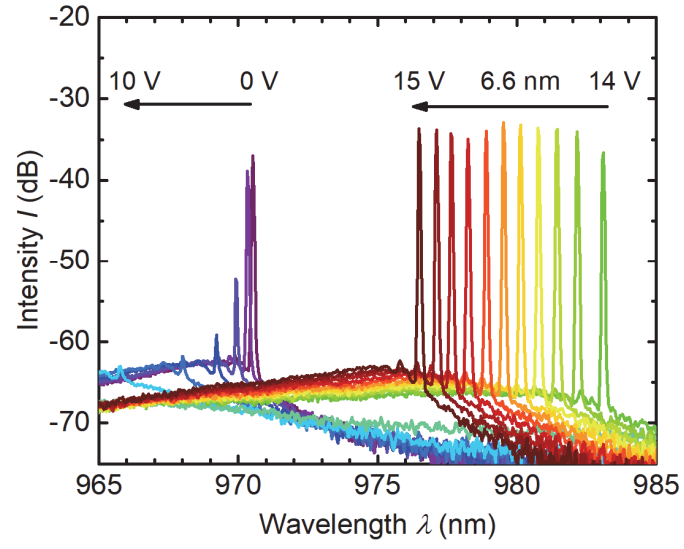
Fig. 5.8 Continues wavelength tuning of the HCG VCSEL with buried InGaP aperture over a spectral range of 6.6 nm. Single mode lasing with SMSR > 25dB is achieved by electrostatic actuation of the MEMS HCG mirror by the indicated voltages.

5.5 Thermal Characterization of Buried InGaP Aperture VCSEL

Compared to an oxide confined VCSEL of comparable architecture the devices with buried InGaP current aperture are expected to show a smaller thermal resistance due to the larger thermal conductivity of the semiconductor InGaP compared to the porous aluminum oxide. Before the thermal resistance is determined later in this section the LIV characteristic was measured at elevated temperatures. Fig. 5.9 summarizes the results. In Part (a) of the graphic the light current curves show the expected decline in optical power from ~0.13 mW at 20°C until the device stops lasing at 45°C. The current voltage curves do not show a significant change for the different temperatures. Exhibit (b) summarizes the temperature trend of threshold current and peak power. The rapidly increasing threshold current for rising temperatures suggest that the gain offset of the laser was designed too small. By offsetting the gain to the blue side of the cavity resonance the overlap of gain and current peak is reached at higher temperature which allows for higher operation current and/or better performance at elevated temperatures as explained earlier in section 4.6 of this work.
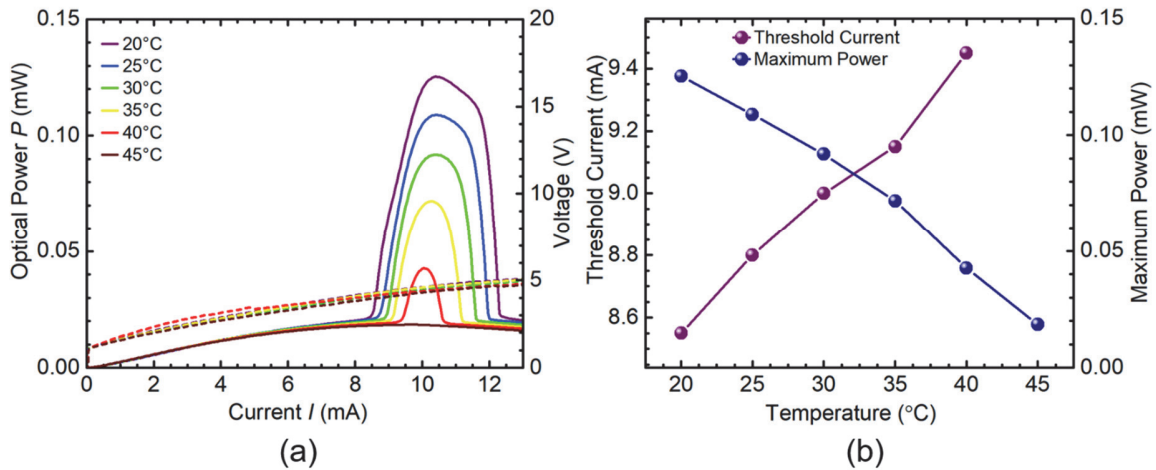
Fig. 5.9 (a) LIV measurement of the buried heterostructure HCG VCSEL for heatsink temperatures of 20 – 45°C. (b) Threshold current increases and maximum power decreases with rising temperature.

In the following the thermal resistance of the buried InGaP aperture device is determined. The analysis is equivalent to that presented in section 4.6. Again, the thermal resistance is calculated from the wavelength change of the lasing mode with the temperature of the external heat sink and the wavelength change with increasing internal heat dissipation. The thermal resistance is calculated according to Eq. 4.2 (p.50) by dividing those two numbers. The spectra of the at heatsink temperatures of 20 – 45°C are presented in Fig. 5.10 and show a systematic red shift with increasing temperature. This can be seen from the inset in the top left corner of the plot where the wavelength of the lasing peak is plotted as a function of the temperature of the heatsink. The blue bullets represent the experimental data and the red line a

linear fit determining the temperature induced shift of the cavity mode $d\lambda/dT = 0.093$ nm/K. This value is relatively high for a GaAs based laser as typical values ae reported in the range of $0.06 - 0.08$ nm/K [15]. However, our value exceeds this range by only 16%.
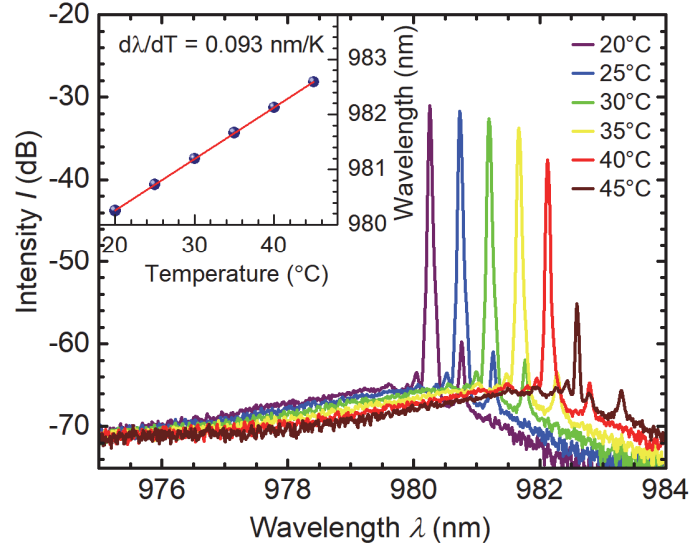
Fig. 5.10 Laser spectra of the buried heterostructure HCG VCSEL at heatsink temperatures from 20 – 45°C. The wavelength of the laser emission shifts red with 0.093 nm/K for rising temperatures.

For the same device spectra at different currents where measured for values from $8 - 12$ mA at 20°C heatsink temperature and are shown in Fig. 5.11. As a result of the internal heating in of the device the laser wavelength shifts red for higher current values. The wavelength of the lasing peak extracted from the spectra is again plotted in the inset in the top left corner of the graph. The linear fit revels a wavelength shift of $d\lambda/dP = 0.11$ nm/mW. Combined with the obtained wavelength shift as response to a change in heatsink temperature a thermal resistance of 1.16 K/mW is obtained. In comparison to the device presented in chapter 4 with oxidized aperture the device with buried InGaP heterostructure based aperture presented in this chapter has the expected lower thermal resistance. The difference between the thermal resistances of the two architectures found here however is small and only constitutes a relative improvement of 5.7%. One factor that could have contributed to this result is the high threshold current of the devices with InGaP aperture leading to significant internal heating, which can affect the accuracy of this measurement method. To limit the effect of internal heating during the measurement of the wavelength shift for different heat sink temperatures a pulsed measurement could have been be used instead of the CW current stimulus.
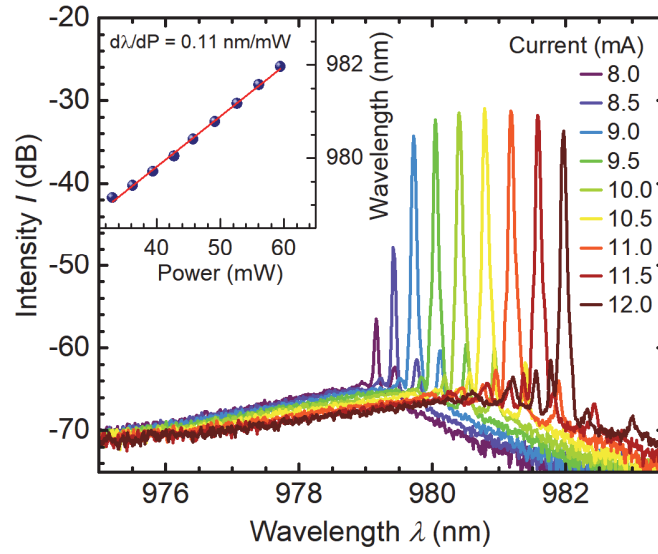
Fig. 5.11 Laser spectra of the buried heterostructure HCG VCSEL for driving currents from 8 – 12 mA. The increased internal heating for larger currents results in a red shift of the laser emission of 0.11 nm/mW. The measured thermal resistance of the device is therefore 1.16 K/mW.

6 HCG VCSEL with Buried Tunnel Junction

The concept of a lithographically defined aperture in not confined to the specific architecture presented in the previous chapter. Lithographic apertures with current blocking based on selective fermi level pinning [42] or reverse biased p-n-junctions [43] and transverse mode confinement based on a phase shifting mesa have been demonstrated. These device have shown thermal resistances lower than comparable oxide confined VCSELs [44], because the thermal conductivity of the GaAs/AlGaAs/AlAs semiconductor is in the range of $10 - 90$ W/mK (depending on the alloy composition) [37][45], while the thermal conductivity of the aluminum oxide aperture material is significantly lower ~0.7 W/mK [46]. Yet another approach to realize lithographic apertures is to use a tunnel junction. VCSELs with tunnel junctions have been demonstrated in great variety. Planar tunnel junctions have been employed in long wavelength InP based devices in combination with metamorphic DBRs [47] and in an architecture with ting (HCG) mirror [24]. One major goal of the tunnel junction in these devices is to switch the doping polarity from p to n to avoid the use of a p-doped DBR and minimize associated material loss. Buried tunnel junction (BJT) with current confining properties have also been investigated before. Devices with at 1550 nm with dielectric DBRs [48] and at 1.3 µm with HCG mirror [49][50] have been demonstrated. Both devices used the InP material system. In this section a VCSEL with buried tunnel junction as lithographically defined current aperture in the GaAs material system will be introduced. The top reflector of the device is a high contrast grating on a selectively oxidized aluminum oxide spacer layer [51]. In contrast to the devices presented in chapters 4 and 5 the VCSEL presented in this chapter emits at a fixed wavelength as its top reflector is designed as static. The presented current confinement scheme has great application potential for the realization of VCSEL arrays with very high density, superior thermal resistance and aperture uniformity as well as for the realization of coherently coupled arrays. From the use of an HCG as top mirror, polarization controlled laser emission can be expected [24] and the epitaxial growth time and material cost will be reduced, as the HCG and spacer layer together are merely 500 nm thick. On the other hand, an integration of the here presented buried tunnel junction aperture with a traditional DBR top reflector is expected to be possible.

6.1 Epitaxial Regrowth Process

To create the buried tunnel junction aperture an epitaxial regrowth process is employed. As with the devices in the previous chapters commercial n-doped DBR substrate was used as bottom mirror. The substrate also included a n-doped GaAs layer on top of the DBR and a GaAsP cap layer designed for selective desorption at the beginning of the first inhouse growth step [19]. The method of regrowth to obtain the buried tunnel junction aperture is detailed in Fig. 6.1. During the first growth step a n-doped GaAs buffer and the active region with four InGaAs/GaAsP strain compensated QWs is grown. The claddings of this lambda cavity are formed by layers of $Al_{30}GaAs$. P-doped GaAs is then grown on top of the active region.

Finally, the tunnel junction layers of highly doped p^{++}-GaAs and n^{++}-GaAs are deposited. The cross section showing the sample after the first growth step is shown in part (a) of the graphic. Next the sample is micro processed to define the current confining apertures. Photolithography was used to expose the area where the tunnel junction had to be etched and current blocking was to be created. A diluted piranha solution with controlled etch rate was used to etch ~80 nm deep through the tunnel junction layers and create the current conducting apertures. Before regrowth the photoresist was thoroughly stripped and a final deoxidation etch was performed. The sample cross section after these steps is shown in Fig. 6.1 (b). During regrowth the top part of the VCSEL cavity is created. It starts with an n-GaAs current supplying and contact layer which is concluded with an InGaP etch stop. Then the top mirror is grown consisting of the oxidizable AlGaAs spacer layer and a final GaAs layer that will be structured during device fabrication to become the HCG reflector. As indicated in cross section (c) the topology of the regrowth was largely conformal to the etched pattern of the buried tunnel junction.
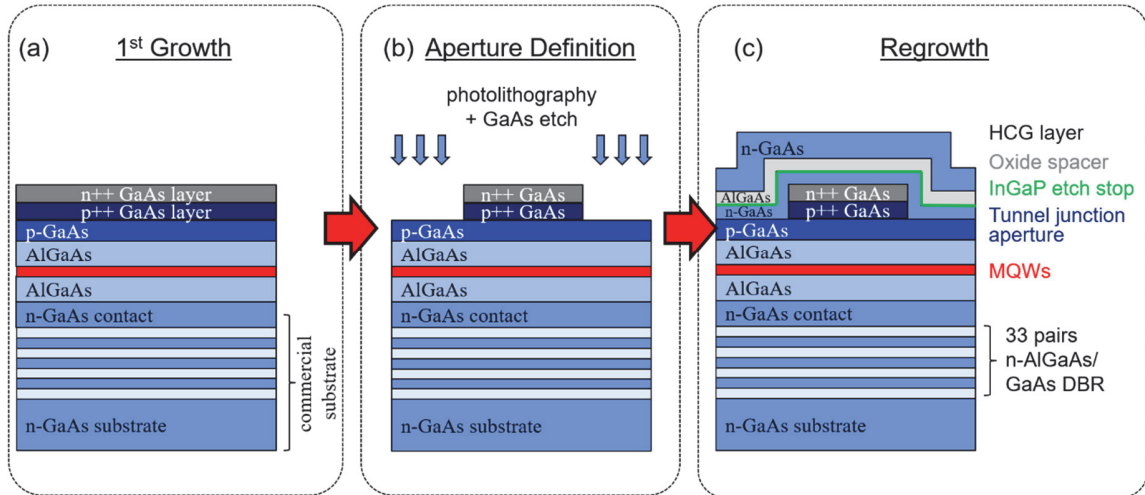
Fig. 6.1 Epitaxial regrowth concept of the buried tunnel junction (BTJ) VCSEL device. (a) In the first growth n-GaAs contact, active region and tunnel junction are grown. (b) The BTJ apertures are patterned by photolithography and dilute Piranha etch. (c) Regrowth of the n-contact current spreading layer, the oxidizable spacer and the GaAs HCG layer is performed.

6.2 Current Confinement by the Buried Tunnel Junction

To test the current confining properties of the buried tunnel junctions, LEDs with apertures were fabricated using the regrowth method described. The LED structure was grown on regular n-doped GaAs substrate, did not contain the InGaP etch stop, oxidizable spacer layer and HCG layer and instead growth was terminated after the n-GaAs cap layer. Thus, omitting the top and bottom reflector in contrast to the VCSEL structure described in the previous section. The LED devices where fabricated in two simple lithography steps. First, diamond shaped mesas where defined by wet chemical, Piranha based etch to insulate individual

devices. Second, contacts where deposited by electron beam evaporation on front and back side of the chip and the top contacts were patterned in a lift off process. The fabrication result is shown by the micrographs of the device in Fig. 6.2 (a). On the bottom the completed device is shown after fabrication. In the center of the diamond shaped mesa the perimeter of the current aperture is faintly visible due to the conformal regrowth. Around the current aperture the semi ring contact is located and contacted by a probe on the bottom edge. The top image shows a corresponding micrograph of the same device under injection of 30 mA continues wave current. The bright electroluminescence is confined to the current conducting buried tunnel junction aperture. Part (b) shows the light current and light voltage characteristic of the LED device. The voltage of the ~13 µm aperture device at 40 mA current is ~3.2 V and thus promisingly low for a first attempt. Both layer thickness and doping of the tunnel junction layers have to be carefully optimized to reach the lowest possible resistance. To evaluate the current blocking properties of the reverse biased p-n-junction in the area where the tunnel junction had been etched, devices without any tunnel junction aperture where fabricated together with the LED devices during the same process on the same chip. The current voltage curve of such a device is presented in graph (c) of the figure. At negative voltages the p-i-n-structure of the active region is biased in reverse and the current flow is very low. At positive voltages the regrown p-n-junction is biased in reverse. The junction restricts the current to less than 1 µA at voltages <2.3V and to less than 1mA at a voltage of 4.5 V. As a typical VCSEL is operated at voltages between 2-3 V the current blocking of the junction is sufficient to effectively confine the current to the low resistance aperture area.
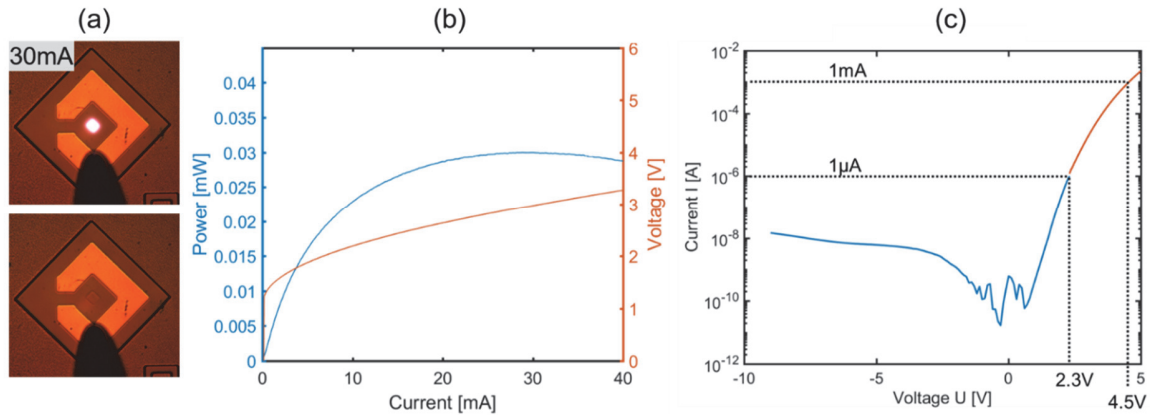
Fig. 6.2 Current confinement and blocking in an LED with BTJ aperture. (a) Micrographs showing an LED with 12 µm square BTJ aperture. Luminescence is confined in the area of the aperture (top). (b) LIV curve of the LED with aperture. (c) IV characteristic of a device with entirely etched BTJ, demonstrating the current blocking properties of the area, with removed tunnel junction.

6.3 Epitaxial Design

In oxide confined VCSELs the current aperture is placed close to and ideally directly at the position of a node of the electrical field [41]. The main reason for this is to minimize optical

absorption in the highly doped aperture layer on the one hand and limit the scattering on the current aperture on the other hand [52], [53]. In the VCSEL with buried tunnel junction aperture the considerations for placing the aperture in the minimum of the electrical field due to scattering are similar [43]. Additionally, since the doping in the tunnel junction layers is very high, the strong free carrier absorption especially in the p-doped part of the tunnel junction has to be minimized by placing the BTJ in the node of the electrical field. In Fig. 6.3 the electrical field (blue) simulated by transfer matrix and refractive index profile (red) are shown along the vertical axis of the VCSEL device. The position of the two highly doped layers of the buried tunnel junction (BJT) (n^{++}-GaAs in grey and p^{++}-GaAs in dark blue) in the node of the E-field is indicated. At approximately 0 μm z-position the four multi quantum wells are visible in the refractive index profile. Here it is important to note that the position of the MQWs should be overlapping with a maximum of the electric field in order to maximize the confinement factor in the VCSEL. As one can see this was done in the presented device.
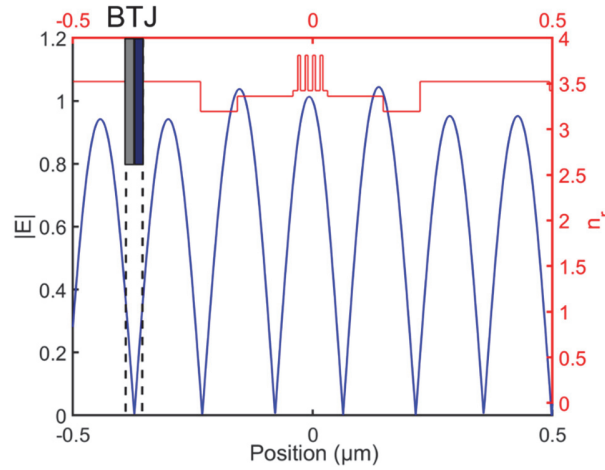
Fig. 6.3 Epitaxial design of the VCSEL at the buried tunnel junction and active region. Absolute of the electric field is plotted in blue and refractive index of the epitaxial layers is plotted in red along the vertical axis of the VCSEL. The tunnel junction is placed in a minimum of the electric field to limit free carrier absorption. The MQWs are positioned to overlap with a maximum of the electric field to maximize the optical confinement factor (courtesy of Jipeng Qi).

67

6.4 HCG VCSEL with Buried Tunnel Junction

The fabrication of the BJT VCSEL device is described in the following. The designs of the four lithographic steps of the process are shown in Fig. 6.4. Part (a) of the schematics shows solely the diamond shaped current aperture in the center. The pattern was created before regrowth as described in section 6.1 and features apertures of sizes 6, 8, 10 and 12 μm diameter. In addition to the apertures, alignment marks where patterned during this step. After regrowth a pattern of diamond shaped mesas as shown in (b) where aligned to the alignment marks of the aperture layer. This was done by photolithography. Piranha based etch was used to etch through HCG and oxidizable spacer layer and stop on the InGaP etch stop. This InGaP layer was removed selectively by a HCL dip and a second piranha etch was used to complete the mesa etch down to the n-GaAs buffer layer on which the active region had been grown. Next the HCG pattern was written by electron beam lithography, where new alignment marks created during the mesa etch where used, since the regrowth pattern was not visible in the SEM image of the lithography tool. The HCG was pattern shown in white color in (c) overlapped with the aperture area. After lithography the HCG layer was etched by RIE so that the oxidizable spacer layer was exposed in the area of the grating gaps. This high aluminum containing spacer layer was then oxidized with water vapor to from an oxide spacer and provide the high refractive index contrast underneath the HCG mirror. Lastly, the Ti/Au contacts of the VCSEL where evaporated. The top n-contact as shown in Fig. 6.4 (d) was patterned by a lift-off process after exposing the n-GaAs contact layer under the InGaP etch stop, while the n-contact on the back of the chip was shared by all devices.

Aperture	Mesa	HCG	Laser p-contact
(a)	(b)	(c)	(d)
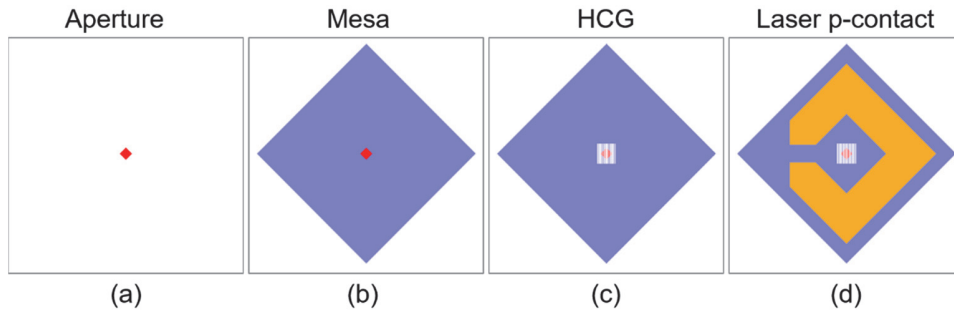
Fig. 6.4 Lithography steps of the BTJ HCG VCSEL. (a) The aperture is formed before regrowth. (b) Diamond shaped mesas are aligned to the apertures. (c) E-beam lithography defines the HCGs covering the aperture area. (d) The top n-contact is formed in a lift-off process.

The result of the fabrication process can be seen in Fig. 6.5. Part (a) of the figure shows the schematic of the completed device as indicated by the green dashed line in the micrograph of the VCSEL. The schematic shows the conformal nature of the regrown layers and as a result the area of the aperture is higher than the surrounding area. The topology of the HCG mirror was thus imaged by atomic force microscopy (AFM) as shown in (c) and indicated in the microscope image (b) by the red dashed line. The AFM measurement reveals how the HCG bars follow the topology of the layer structure. The shift in the reflector was measured to be of

the height of the underlaying aperture pattern, ~80 nm in the presented sample. Additionally, on the left top edge of the aperture a crystal plane dependent regrowth effect is visible that corrugates the HCG mirror. To enhance the planarization of the mirror and to minimize scattering on the buried aperture the thickness of the buried tunnel junction apertures should be decreased. Additionally, careful optimization of the regrowth conditions is necessary to prevent the crystal plane dependent parasitic growth as visible on the top left edge of the aperture in (c).
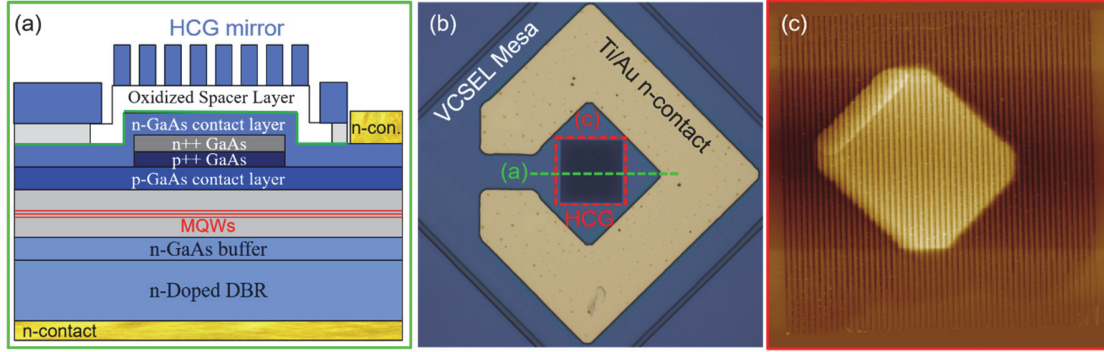
Fig. 6.5 BTJ HCG VCSEL device. (a) Schematic of the cross-section of the finished device in the region of the BTJ aperture as indicated by the green dashed line in b. (b) Micrograph of the device showing the mesa, the top n-contact and the HCG covering the aperture region in the center of the device. (c) AFM-detail of the aperture region as indicated in b (courtesy of Kevin Cook).

Light current characteristic and spectra were analyzed for devices with BJT apertures of sizes 6 – 12 μm. The results are shown in Fig. 6.6. All measurements where performed at room temperature and continues wave current stimulus. As expected, both threshold and maximum power of the devices increase with aperture size. Sub-milliamp thresholds where observed for the devices with 6 and 8 μm apertures, while the threshold of the 12 μm device was observed at 2.5 mA. A maximum optical power of 1.4 mW was demonstrated by the device with the 12 μm aperture. The slope efficiency of the devices with smaller aperture was clearly lower than for the devices with larger apertures. This could be the result of the parasitic regrowth effect at the edge of the aperture area. For smaller apertures this scattering source covers a larger proportion of the aperture area, thus a larger penalty on the laser power is expected for these devices. An additional factor for the limited performance of the devices is clearly their high voltage. Devices of all examined aperture sizes show operating voltages of up to 8 V. Both turn on voltage of ~3 V as well as ohmic resistance have to be improved. As devices with smaller apertures show significantly higher resistances, it must be concluded that the BTJ aperture is the main contributing factor to the high series resistance. Thus, doping level and thickness of the tunnel junction layers need to be carefully optimized to obtain an improved series resistance. The choice of tellurium and carbon as dopants for the GaAs tunnel junction as used in this work is reported to achieve low resistances of 12.5 mΩ/cm^2 and ohmic tunneling [54]. The spectra of devices with different aperture sizes are shown in Fig. 6.6. The

spectra in graph (b) were measured at 1.1 I_{th} and the spectra in graph (c) at the maximum optical power. Although the apertures used in this experiment are 6 µm and larger, the spectra show only a few lasing modes. This can be attributed to two effects. First the HCG mirror is known to suppress higher order modes because of its angle depended reflectivity characteristic and defined polarization. Second the BJT aperture does not present a strong optical confinement in contrast to the oxide aperture in oxide confined VCSELs. The optical confinement the presented device does however depend on the phase shift between aperture region and surrounding. By minimizing the height of the BJT aperture an even weaker optical confinement can be expected. Thus, the presented HCG VCSEL with BTJ aperture is a promising architecture to realize large aperture, high power, polarization controlled, single mode VCSELs.
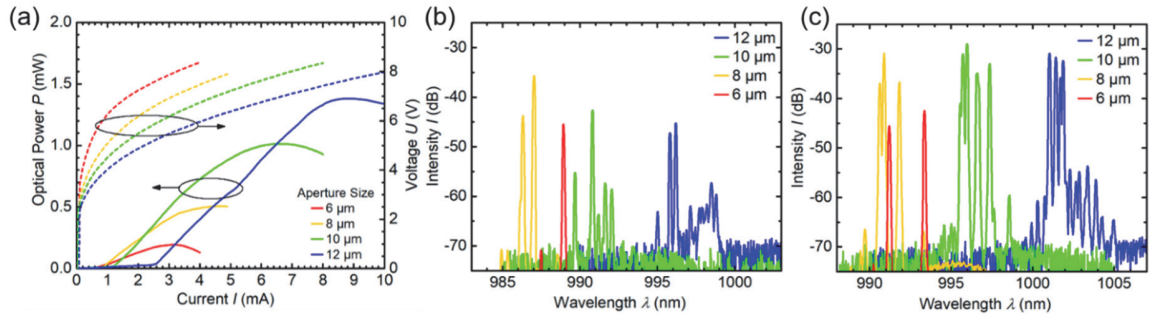
Fig. 6.6 VCSEL characteristics for square apertures 6-12 µm. (a) LIV curves showing the expected trends of higher thresholds, higher powers and lower voltages towards larger apertures. Spectra at 1.1 I_{th} (b) and peak power (c) for the same devices.

6.5   Thermal Characterization of the HCG VCSEL with BJT

As for the device architectures introduced in chapter 4 and 5 in this section the thermal properties of the VCSEL with BJT current aperture are investigated. All results are shown in Fig. 6.7. The light current characteristic of the BJT device is presented for temperatures of 17 – 47°C in part (a) of the figure. The peak optical power decreases for higher temperatures and the rollover is reached at a lower current. In contrast to the devices from the earlier chapters however, the threshold current of the BJT device decreases with rising temperature and the decline in maximum power is less severe. This indicates that the offset of the peak of the gain spectrum from the cavity resonance is larger in the device here resulting in a better high temperature performance of the BJT device. This is despite a high expected internal heating from the non-optimized, high resistance tunnel junction that is apparent in the >6 V operation voltage. In graph (b) the spectra of the same VCSEL are presented for the temperatures of 17 – 47°C. The main lasing mode shifts its peak wavelength with temperature at a rate of $d\lambda/dT = 0.08$ nm/K. This value fits well the range reported in literature (for oxide confined VCSELs) [15] and is comparable to the values obtained from the devices reported in the previous sections. Spectra for a range of laser currents are shown in graph (c). From the

spectral shift of the individual modes the wavelength shift as a function of dissipated power in the laser can be extracted and is fitted to be $d\lambda/dP = 0.098$ nm/mW. As a result, the thermal resistance of the device was calculated by using Eq. 4.2 (p.50) to be $R_{th} = 1.21$ K/mW. This value is slightly better than the result obtained from the oxide confined widely tunable VCSEL in chapter 4, but not as good as the result from obtained by the VCSEL with buried InGaP heterostructure as aperture. The difference could originate from the lack of the thick GaAs sacrificial layer which is present in the tunable VCSEL architecture in contrast to the thinner, partially oxidized top layers in the oxide spacer architecture used for the tunnel junction device. The result here also underperforms the results by Demir. et al. [44] obtained with VCSELs featuring a lithographic aperture. The referenced work however, utilized a binary n-DBR that contributes a higher thermal conductivity.
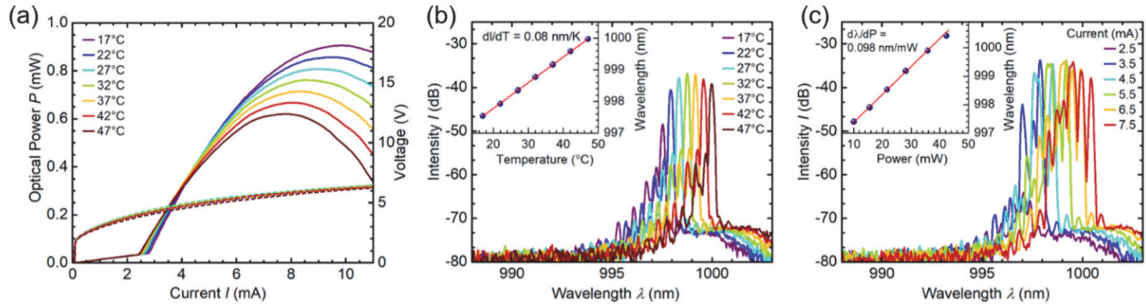
Fig. 6.7 Thermal characteristics of one BTJ VCSEL device. (a) LIV curves at heat sink temperatures 17-47°C. (b) Laser spectra at those different temperatures and observed shift in wavelength as function of temperature, $d\lambda/dT = 0.08$ nm/K. (c) Spectra for different laser currents and extracted change of wavelength of the laser modes as function of the dissipated thermal power. A thermal resistance of 1.21 K/mW was calculated.

7 Fabrication of High Power VCSEL Arrays

Two dimensional high power VCSEL arrays have been pioneered in the 1990s [55], [56] to overcome the power limit of single aperture VCSEL devices [57]. To achieve higher output power the idea is to integrate a large number individual VCSEL emitters with uniform properties into an array. In the described arrangement and in the work presented in the following the individual emitters, share electrical contacts (except ref. [56]) and are thermally coupled, but the individual VCSEL elements of the array are not coupling optically. Thus, this type of array is referred to as incoherently coupled array in contrast to a system in which individual emitters couple optically and the lasing modes extend over multiple or all elements of the array. The later type is referred to as quasi-coherently coupled array or simply coherently coupled VCSEL array depending on the extend of the optical coupling. These types of systems also have been extensively studied [58], but the discussion here shall be confined to the incoherently coupled VCSEL arrays. Although already investigated in the 1990s, VCSEL arrays are currently experiencing a real boom, as multiple consumer applications have been developed for which VCSEL arrays are the ideal light sources. These applications are 3D imaging in general, facial recognition in particular and proximity sensing which use structured light and time of flight detection schemes. An additional application VCSEL arrays are developed for is time of flight sensing for LIDAR in autonomous vehicles. In the following initial results of VCSEL arrays are presented. The first part of this chapter describes VCSEL arrays emitting at 850 nm wavelength and the comparison of two different fabrication architectures. The first architecture uses a planarizing passivation layer of benzocyclobutene (BCB) polymer and the second uses a layer of silicon nitride which serves both as passivation as well as anti-reflection coating. The second half of the chapter introduces an improved design of the VCSEL array realized in 940 nm epitaxy.

7.1 850 nm VCSEL Array with BCB and SiN Passivation

This section describes two different fabrication processes for the realization of VCSEL arrays. The first uses BCB as planarization layer, the second uses silicon nitride. For each method arrays of 1, 2, 4, 8, 16, 32, 64 and 128 elements where fabricated and their performance under continues wave current stimulus evaluated.

7.1.1 Fabrication of BCB and SiN Passivated VCSEL Arrays

For the fabrication of the VCSEL arrays emitting at 850 nm wavelength commercial epitaxy was used. The layer structure of this oxide confined VCSEL contained the following elements: The n-doped bottom DBR was formed by 34 pairs of graded $Al_{12}GaAs$ and $Al_{90}GaAs$ $\lambda/4$-layers. The top DBR featured 22 pairs of p-doped material with the same alloy composition. The oxidizable aperture layer was comprised of 30 nm thick $Al_{98}GaAs$ and 30.5 nm $Al_{90}GaAs$ and the active region consisted of 3 GaAs quantum wells with $Al_{30}GaAs$ barriers. The claddings were AlGaAs graded from 30 – 60% Al content from the MQWs towards the DBR mirrors. All layers were grown on GaAs substrate. The epitaxy was cleaved

into chips of 1x1cm size and fabricated into VCSEL arrays with 1 – 128 elements per array. All elements were arranged on a square lattice. Arrays with element numbers of 1, 4, 16, 64 had a pitch of 40 μm and arrays with 2, 8, 32, 128 elements had a pitch of ~28 μm. The cross section through one element of the VCSEL array for major steps of the fabrication process for BCB and SiN architecture is shown in
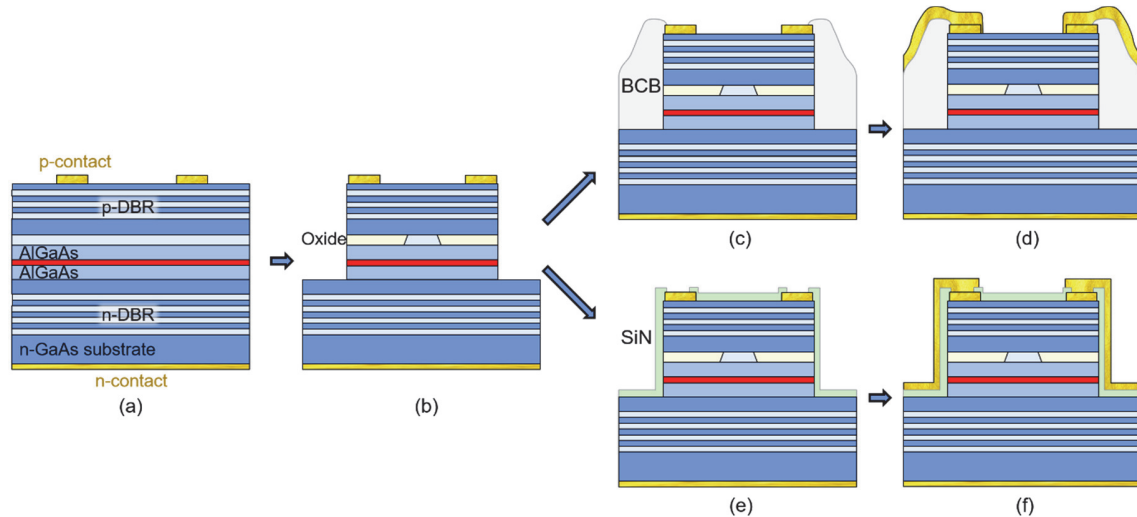
Fig. 7.1. As the first step p- and n-side titanium/gold ohmic contacts where deposited on the wafer and the p-top contact was patterned in a lift-off process as shown in part (a) of the graphic. Then the trenches were defined by photolithography and subsequent RIE etch. This defined the individual elements of the array and electrically insulated the p-contact in the area of the array from the remaining chip. After stripping the resist and cleaning the sample selective oxidation of the dedicated high aluminum content layer was done to define the current apertures of the individual VCSEL elements. At the same time the high temperature of 435°C during the oxidation process was used to anneal the ohmic contacts. The cross section after trench etch and oxidation is shown in (b). At this stage in the process the VCSEL array could already be tested. In order to achieve uniform distribution of the current to all elements and to protect the laser from damage passivation and planarization with BCB and SiN was tested. Part (c) and (d) of the figure show the process used to apply the BCB passivation. First, photoactive BCB was spin coated onto the sample and exposed in the areas where the passivation was necessary. In the unexposed areas on contacts and on the laser apertures the BCB was removed during development. The result is shown in (c). Finally, an additional layer of Ti/Au was evaporated to connect the individual VCSEL elements among each other across the trenches and to form metal pads for probing. Again, a lift-off process was used to pattern

the metal
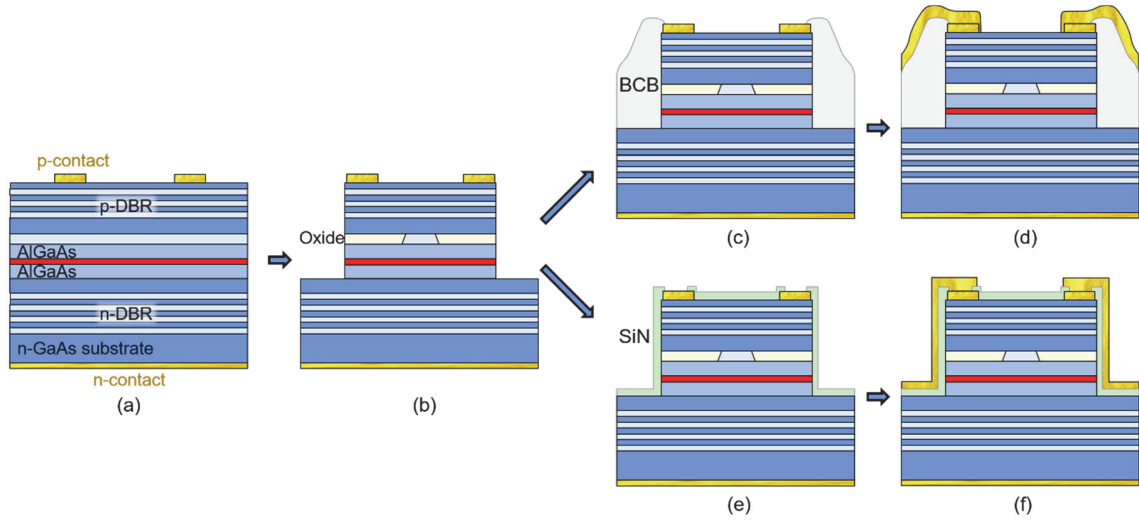
Fig. 7.1 (d). As indicated in the cross section the BCB covers the steep slopes of the trenches created by RIE etch effectively and partially planarizes the sample topology.
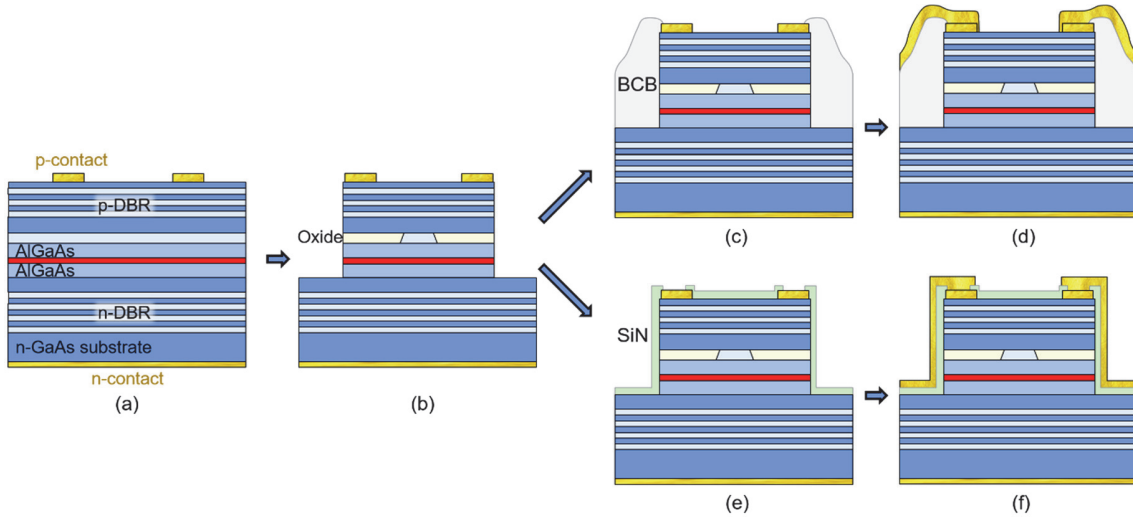
Fig. 7.1 Cross sectional schematic of the fabrication of 850 nm VCSEL arrays. (a) p- and n-contact definition. (b) Reactive ion etch to define trenches and oxidation to define the current apertures of individual VCSEL elements. (c, d) Planarization using BCB and contact pad evaporation. (e, f) Passivation and antireflection coating with SiN and contact pad evaporation.

Thus, the evaporated pad metal covers the BCB film uniformly and provides efficient current distribution between the elements of the array. As second fabrication method SiN was tested as shown in the cross sections part (e) and (f). As indicated in cross section (e) the SiN film conformally covers the sample surface. As a result, it has a negligible planarizing function. Just as the BCB however, it provides an insulating layer on which the pad metal can be applied. After deposition of the PECVD SiN contact vias were patterned by photolithography and subsequent wet chemical etch with buffered

oxide etchant to expose the underlying contacts of the array elements. Finally, Ti/Au pad metal was evaporated to improve the current flow between adjacent VCSEL elements and create the metal pads for probing. The cross section after the final metallization is shown in part (f) of
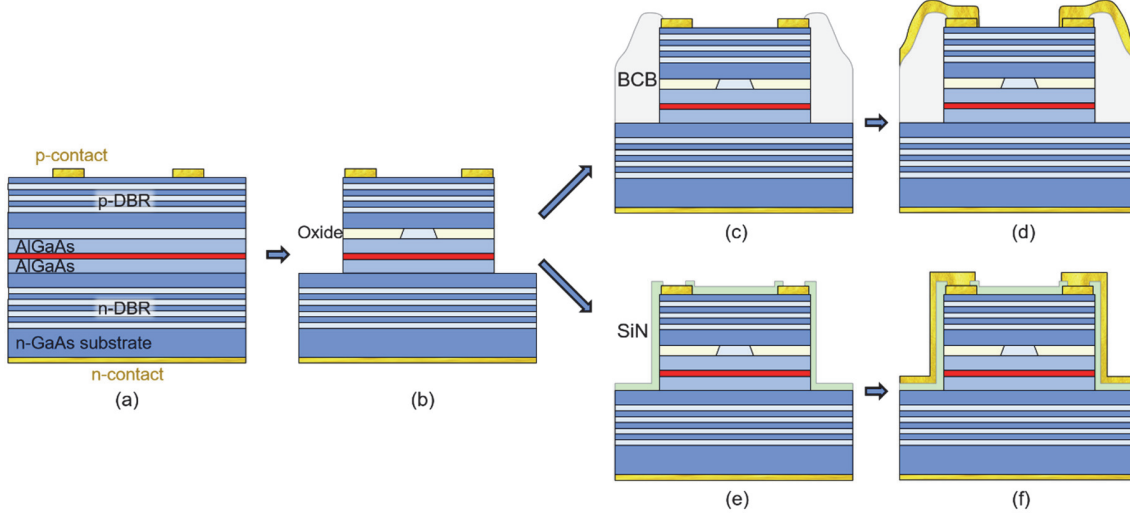
Fig. 7.1. While it is apparent that the SiN passivation provides insufficient planarization it also has an advantage. In this architecture the SiN layer can be designed as anti-reflection coating to lower the reflectivity of the top facet of the VCSEL and allow a greater portion of the light to be emitted. In the described case this was achieved by depositing ~110 nm of SiN with refractive index of 2.

7.1.2 Single Device Performance

The performance of single devices with BCB planarization and SiN anti-reflection coating was compared. A direct comparison of light current characteristic as well as efficiency and differential resistance is shown in Fig. 7.2. Both devices were chosen with comparable aperture sizes and tested with continues wave current of 0 – 20 mA at room temperature. While the threshold of the BCB device of 0.7 mA (turquoise curve in graphic (a)) is clearly lower than that of the SiN coated device of 1.8 mA (blue curve) the maximum optical power of the SiN coated device (11.5 mW) is more than twice as high as the maximum power of the BCB device (4.4 mW). This result fits the initial expectation as the SiN anti reflection coating lowers the top mirrors reflectivity in a favorable way. The experiment shows that the epitaxy with 22 top DBR pairs was designed rather conservatively in the sense that the reflectivity of the top DBR was clearly too high to achieve the optimum optical power. As result of the higher optical powers enabled by the SiN antireflection coating the SiN architecture also reaches a higher slope efficiency of close to 0.95 W/A while the slope efficiency of the device with BCB peaked at only 0.48 W/A at a current of ~6 mA. The corresponding maximum wall plug efficiencies were 26.9% and 12.4% The resistance of the of the BCB coated device in this measurement is clearly higher than that of the SiN passivated device this difference however was caused by an alternative n-metal contact that was tested on the BCB device. The

difference in resistance thus is not due to the BCB architecture. Because both p- and n-contact of the BCB and SiN devices where created in the beginning of the process in the same way. It is expected that originally there are only minor differences in the resistances (and differential resistances) between the two devices. The micrograph of the SiN passivated device can be seen in the inset in graph (a) and shows the electroluminescence below lasing threshold in the region of the aperture. From this image the aperture size was measured to be 7.5 µm.
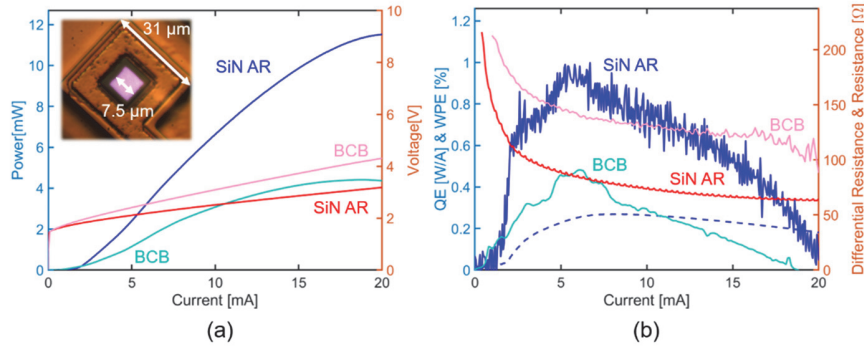
Fig. 7.2 Comparison of single device performance of BCB and SiN passivated 850 nm VCSELs. (a) Comparison of LIV curves and micrograph of the SiN passivated device. (b) Comparison of differential quantum efficiency and differential resistance.

Based on the size of the square aperture multi-mode emission of the laser is expected. To confirm this the spectrum of the laser was measured above lasing threshold at current stimulus of 3, 5, 10, 15 and 20 mA. The results of this measurement for the single device with SiN anti-reflection coating are shown in Fig. 7.3 (a). Just above threshold at 3 mA (red) the spectrum shows a single lasing mode dominating the spectrum, but additional modes are visible. At higher currents more lasing modes emerge in the spectrum on the blue side of the original lasing mode while the entire spectrum shifts red from 853 nm to 859 nm as a result of the internal heating of the laser. Images (b-f) of the graphic show the near field images of the VCSEL corresponding to the 5 spectra. At current values above 5 mA the near field pattern shows a complicated pattern resulting from the multitude of coexisting higher order lasing modes.
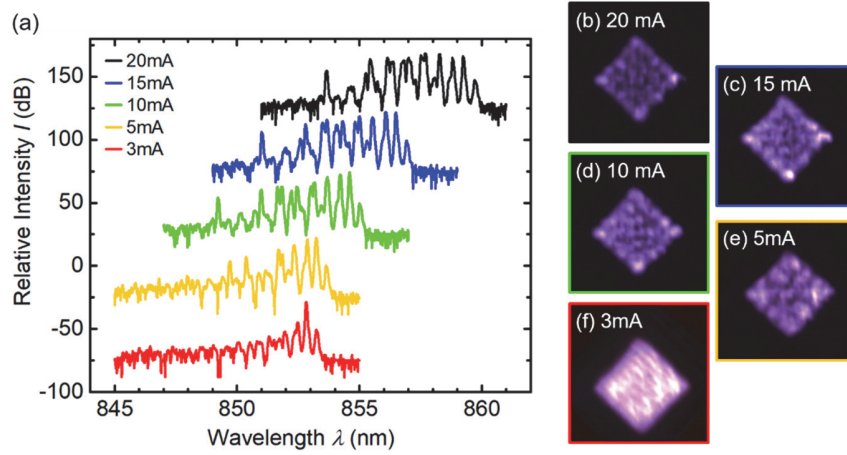
Fig. 7.3 (a) Spectra of the SiN passivated 850 nm VCSEL at currents from 3 – 20 mA, showing multimode emission. (b-f) images of the near field emission of the laser at corresponding currents.

7.1.3 Array performance

After the characterization of the single VCSEL element this section discusses the properties and performance of the fabricated arrays. Again, a comparison between the devices with BCB and SiN passivation is made where the larges array with 128 elements is used to illustrate the array specific effects on the LIV characteristic and the spectrum. Fig. 7.4 (a) shows the light current voltage curves of BCB and SiN based architectures. The inset of the graphic shows a micrograph of the array with 128 elements and BCB passivation. In the center the VCSEL elements are located on a square grid, on the left and right side of the image two contact pads are visible. To measure the LIV curves the array was contacted with two probe needles on either side of the array and continues wave current was supplied from 0 mA to 900 mA. Similar to the result of the single devices the peak power of 371 mW of the array with SiN antireflection coating is significantly higher compared to a peak power of 201 mW for the BCB passivated device. At the same time the threshold of the BCB device was reached at 100 mA and thus earlier than that of 250 mA of the array with SiN antireflection coating. This fits the expectation of the anti-reflection coating to lower the reflectivity of the top DBR. The current voltage curves of the two arrays are very similar as expected from their common contact fabrication steps. The slightly higher voltage of the BCB device may result from a small difference in aperture sizes or a difference in the contact from chip to chuck on the measurement setup. One additional differentiation of the two arrays is the shape of the lasing threshold. While the threshold of the BCB passivated device is sharp, the SiN passivated array shows a rather gradual threshold. This may be the result of the better current distribution between the individual elements that is expected from the planarization provided by the BCB architecture allowing all elements to reach threshold at the same current. Since no planarization was provided by the SiN passivation the side walls of the trenches are barely covered by metal and the current distribution in the arrays is worse. As a result, elements

closer to the current supplying probe tips reached threshold earlier and the threshold in the LIV curve of the entire array appears gradual. In Fig. 7.4 (b) the corresponding efficiencies of the two array architectures are plotted as function of the current. The array with BCB passivation reached a maximum slope efficiency of 0.39 W/A and a wall plug efficiency (WPE) of 8.1 %, while the array with SiN anti-reflection coating demonstrated a maximum slope efficiency of 0.91 W/A and a maximum WPE of 17.1 %. Spectrum and nearfield of the SiN passivated device are shown in part (c) of the graphic. The near field above threshold as shown in the inset of (c) appears uniform and all observed emitters of the array are functional. The spectrum of the entire array was measured for a current of 1.1 I_{th} (blue curve) and close to maximum power (red curve). As expected, the emission spectrum of the array is shifted red at higher current due to internal heating of the array. Additionally, the width of the spectrum at higher current is broader as a result of the higher order mode emission in every single one of its elements. Despite this effect the -8.5 dB width of the spectrum is ~4 nm.
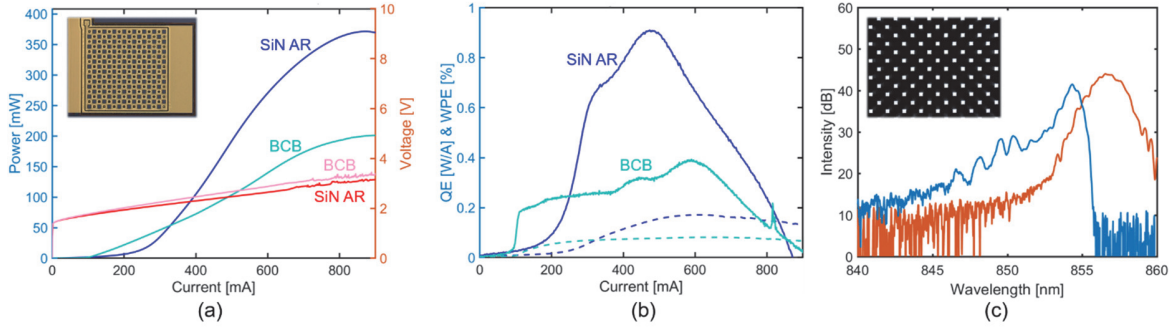
Fig. 7.4 Comparison of the performance of BCB and SiN passivated 850 nm VCSEL arrays with 128 elements. (a) Comparison of LIV curves and micrograph of the BCB passivated device. (b) Comparison of differential quantum efficiency and wall-plug efficiency. (c) Spectra of the SiN passivated 128 element array at 1.1 I_{th} (blue) and peak power (red) with inset showing the near field image of the device.

If one compares the efficiencies obtained from the single device with those of the 128 element arrays one finds that the array efficiencies of both architectures underperform the single element values. This has two possible reasons. First, it is expected that the array has a certain element to element variation in performance, as a result all elements may not operate at their optimum efficiency point at the supplied current (or better voltage, since they are in a parallel arrangement). This type of variation however can be minimized by a thoroughly developed fabrication process. The second more important reason for the discrepancy in performance is due to the thermal coupling of the array elements. This coupling results in an effectively greater thermal resistance of every single element placed in the array [59], [60] and additionally a variation of effective thermal resistance between elements at the corner, the edge and the center in the array [61]. The severity of the thermal penalty is even greater at the maximum power point. The drop in peak power per element with rising size of the array is

shown in Fig. 7.5 for BCB (blue) and SiN architecture (red). The measured peak power per element is plotted in the form of circles as function of the number of elements of the array.
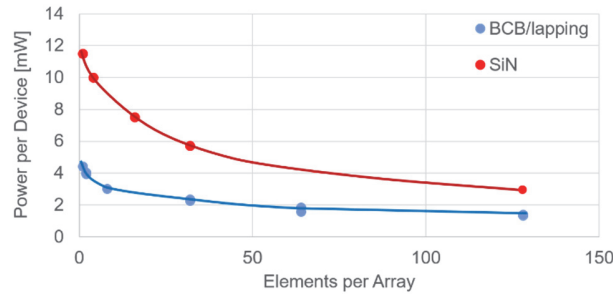
Fig. 7.5 Optical power per laser element for the BCB and SiN passivated devices based on the measurement of VCSEL arrays with 1, 2, 4, 8, 16, 32, 64, 128 elements. The power per element decreases for larger arrays primarily due to strong heating effects in the larger arrays.

A trendline is plotted as a guide to the eye of the reader. As a result of the strong thermal crosstalk between the array elements the power of the peak power per device quickly drops as the number of elements in the array increases. Compared to the single element power the power per element drops by 3x for the SiN device. The chip of the BCB planarized devices was thinned down to increase the thermal coupling to the heatsink by lapping the substrate to a thickness of 150 - 200 μm. As a result, the relative drop in power per element for the 128-element array compared to the single device is smaller in this case and closer to 2.5x, but still very significant. This result shows the amplified importance of thermal design for VCSEL arrays.

7.2 940 nm VCSEL Array with SiN Antireflection Coating

Under consideration of the results obtained from the 850 nm arrays a second improved generation of devices was designed fabricated at the wavelength of 940 nm. This wavelength is preferred for many of the mentioned consumer applications, as an absorption line of water reduces the intensity of sun light in this wavelength range, resulting in an increased signal to noise ratio of the measurement system due to the lower amplitude of parasitic back ground light.

7.2.1 Epitaxy and Fabrication Architecture

Several changes were made to the epitaxy of the 940 nm VCSEL array compared to the 850 nm epitaxy. The bottom n-DBR was designed with 36 pairs of graded GaAs/AlAs λ/4 layers. The binary alloys where chosen to improve the thermal conductance of the bottom mirror. The optimization of the thermal resistance although already important for a single VCSEL is absolutely crucial in VCSEL arrays. Specifically the thermal conductance in transverse direction of the bottom DBR is the most important factor for the thermal resistance of the

array [61]. GaAs and AlAs have bulk thermal conductivities of 0.45 and 0.91 W/cm K respectively [62][37]. Their ternary alloys in contrast have thermal conductivities as low as 0.1 W/cm K depending on composition [63], due to alloy scattering of phonons. For this reason, the choice of binary alloys is expected to improve the thermal conductivity of the bottom DBR significantly. It has to mentioned however that the thermal conductivity of the DBR structure is expected to be lower than the average of that of the bulk materials, as interface scattering in this superlattice contributes strongly to its overall thermal resistance. Such thermal effects in superlattices have been investigated in several publications [64][65][66]. The active region of the 940 nm VCSEL array had four InGaAs/GaAsP strain balanced quantum wells and $Al_{30}GaAs$ claddings and was separated from the bottom DBR by a 2λ thick GaAs layer. This layer served dual purpose. It improves thermal conductance close to the active region and at the same time was necessary for the fabrication as it served as a spacer layer to prevent the mesa etch to reach the binary bottom DBR. The oxidation layer was 28 nm thick of $Al_{98}GaAs$ next to 50 nm of $Al_{90}GaAs$. In the p-doped top DBR the number of pairs was reduced to 18 pairs and the alloys of GaAs and $Al_{90}GaAs$. Bring the compositions closer to the extreme of the binary materials enhances the refractive index contrast and thus lowers the number of DBR pairs required. Besides optical and thermal considerations the electrical properties of the DBR must be carefully designed [67] and graded interfaces and interface doping where used to limit electrical resistance and voltage drop of the DBRs. After growth of the epitaxy design by a commercial foundry the fabrication of single VCSEL elements and VCSEL arrays is described in the following. First a protective layer of photoresist is applied to the entire wafer. This layer protects the wafer surface from dust particles created while dicing the wafer into 1x1 cm chips for further fabrication. As the first step the wafer is then cleaned by stripping the protective resist in a high-pressure lift-off tool. It is important to mention that for arrays with large number of elements low defect densities in both fabrication and epitaxy are of increased importance compared to the fabrication of single VCSELs. Accordingly, the fabrication routine was improved by adding yield improving steps such as removal of edge beat before lithography, descum and ash of photoresist (PR) in oxygen plasma, deoxidation in dilute HCL before oxidation and the before mentioned high pressure strip and lift-off routine to remove surface particles. Cross section schematics of the VCSEL array are shown after each major fabrication step in Fig. 7.6. As first step after the initial clean round mesas on a hexagonal lattice were defined by RIE etch (a). After strip of the (PR) the sample underwent oxidation with water vapor at 435 C°. The oxidized mesas were passivated by 5 nm of Al_2O_3 deposited by atomic layer deposition. As electrical insulation layer and anti-reflection coating PECVD silicon nitride was deposited (b). In an experiment on single devices with simplified device architecture SiN thicknesses from 70 – 120 nm were tested and 105 nm think SiN showed the highest wall plug efficiency.
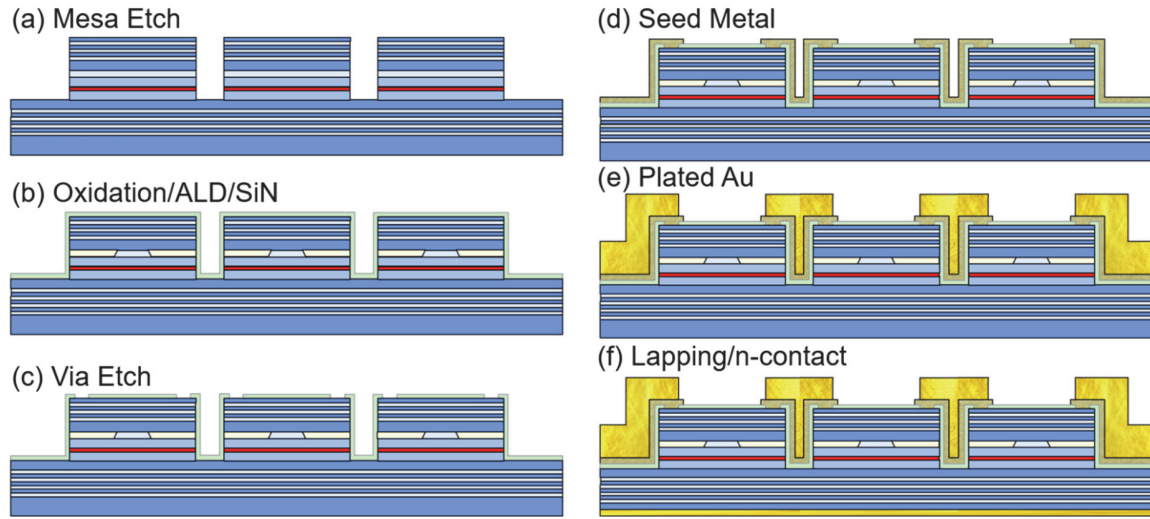
Fig. 7.6 Cross sectional schematic of the 940 nm VCSEL Array fabrication. (a) Mesa definition by RIE etch (b) Oxidation of the current apertures and passivation with ALD Al_2O_3 and SiN. (c) Etch of the passivation in the areas of the ohmic contacts. (d) Evaporation of p-contact and seed metal layer. (e) Electroplating of Gold. (f) Lapping of the substrate and evaporation of the back-side n-contact.

After the passivation vias were etched through ALD aluminum oxide and SiN using BOE wet chemical etch to expose a ring surrounding the emitter area on each mesa (c). A seed metal layer of Ti/Au was evaporated on to the passivated mesas to contact the VCSEL elements through the vias. Lift-off was used to pattern this layer (d). Since the SiN passivation does not planarize the step side walls electroplating was used to deposit micrometer thick gold onto the seed metal layer. In this way the current delivery across the array was improved (e). Finally, to lower the thermal resistance of the array the substrate was thinned down to 100 μm by lapping before the n-contact was evaporated (f). Ni/GeAu/Ni/Au was used as metal to form ohmic contact to the n-doped GaAs substrate [68][69]. Before testing the sample was annealed at 350°C in nitrogen atmosphere for one minute.

7.2.2 Single device performance

Before results of the VCSEL array are presented in the following section the performance of a device with a single element is discussed in this section. LIV curve and efficiency are presented in Fig. 7.7. The data was measured under continues wave current at 20°C heat sink temperature on a VCSEL with ~8 μm aperture size. The light current curve in part (a) of the graphic shows a threshold of 1 mA and maximum power of 17.7 mW. The voltage of the device reaches 3 V at 20 mA. The resulting efficiencies showed maxima at 0.77 W/A (slope) and 36.2 % (WPE). Compared to the 850 nm device the 940 nm design shows thermal role over at higher currents indicating the better thermal design of the structure. Additionally, the wall plug efficiency was improved significantly and a lower threshold of 1 mA was achieved despite the application of the anti-reflection coating. This fact indicates that a further

reduction of the number of top DBR pairs can be made to lower the reflectivity of the top mirror. In exchange the SiN passivation should then be designed optically invisible at a thickness of multiple of $\lambda/2$.
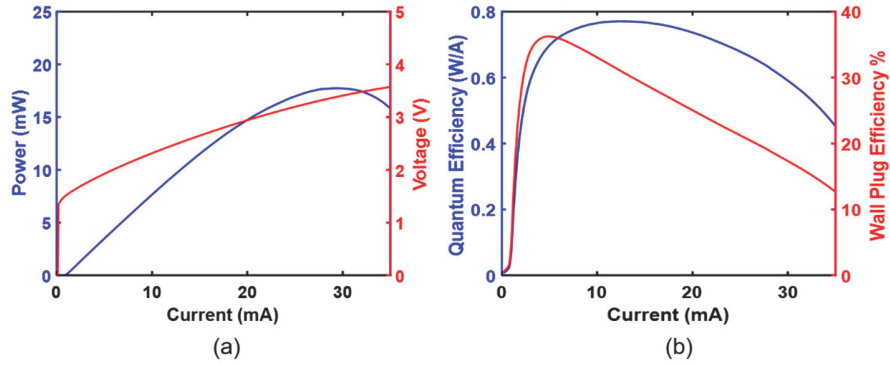
Fig. 7.7 Performance of the 940 nm VCSEL single device. (a) LIV curve of the laser with 1 mA threshold current and 17.7 mW peak optical power. (b) Quantum efficiency and wall-plug efficiency with maxima at 0.77 W/A and 36.2% respectively.

7.2.3 940nm High Power VCSEL Array

Finally, the performance of the 940 nm emitting VCSEL array was measured and the results are shown in Fig. 7.8. The array measured had 68 elements and aperture diameters of 18 μm. The pitch of the array of 70 μm was designed larger than that of the 850 nm design to reduce the density of the thermal power dissipation. CW current of up to 1.5 A was used to measure the LIV curve of the array and the temperature of the heat sink was lowered to 11°C. A threshold of 160 mA was observed and a peak optical power of 642 mW (see graphic (a)). This corresponds to an average threshold of 2.35 mA and an average power of 9.4 mW per emitter. While the larger threshold is due to the increased aperture size compared to the single device from the previous section the lower output power of the devices again arises from the higher effective thermal resistance of the emitters in a large array. Accordingly, maximum slope efficiency and wall plug efficiency of 0.57 W/A and 22.6% are demonstrated as shown in graphic (b). Spectra of the entire array where taken at 2 I_{th}, 5 I_{th} and peak power point. For the latter two conditions -8.5 dB widths of 3.3 nm and 4.25 nm were measured. Thus, the spectral width of the 940 nm array is nearly comparable to that of the 850 nm array. The slightly wider spectrum can be expected from the larger oxide apertures, which promote multi-mode emission. Although the 940 nm array clearly demonstrates an improved power and wall plug efficiency compared to the 850nm array. A high degree of emitter nonuniformity and a high emitter failure rate was observed. This was primarily caused by local spiking in the RIE etch depth and resulting parasitic oxidation of the binary bottom DBR pairs leading to high resistance and scattering loss in the effected devices. Additionally, non-circular oxidation apertures were observed that may result from strain effects created by the thick 28 nm $Al_{98}GaAs$/50 nm $Al_{90}GaAs$ oxidation layer.
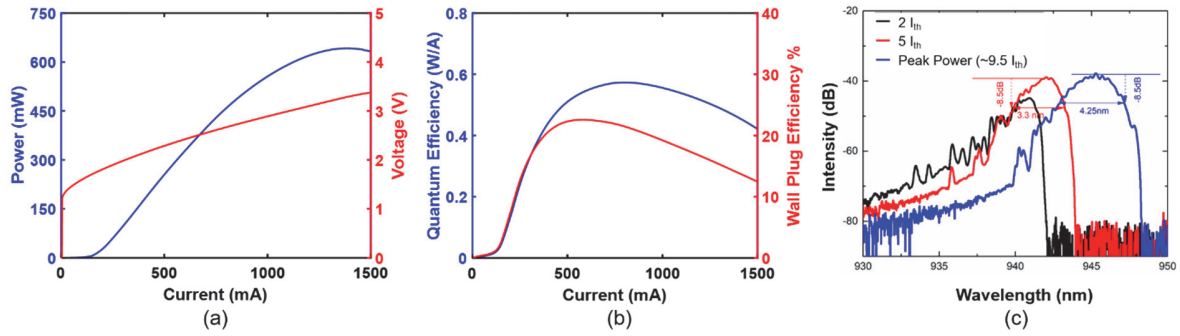
Fig. 7.8 Performance of the 940 nm VCSEL 68 element array. (a) LIV curve of the array with threshold current of 160 mA and 642 mW peak optical power. (b) Quantum efficiency and wall-plug efficiency with maxima at 0.57 W/A and 22.6% respectively. (c) Spectra of the array at 2 I_{th}, 5 I_{th} and peak power with spectral width at the -8.5 dB point.

8   Conclusion and Outlook

In summary, this work examined a selection of architectures of vertical cavity surface emitting lasers (VCSELs) that are promising to improve performance in emerging sensing applications. Realizing a VCSEL requires both epitaxial growth and microfabrication capability. Since a standing epitaxial routine was initially not available, chapter 2 outlines the major milestones that were taken to develop epitaxial growth of VCSEL material. Those were the following: (1) The demonstration of highly efficient active material in this case the strain compensated InGaAs/GaAsP multi quantum well, (2) the calibration of doping densities for n- and p-dopant species (tellurium and carbon) in various compositions of GaAs and AlGaAs and the assembly of active material and doped layers into a light emitting diode, (3) the quantitative measurements of material gain and loss from edge emitting lasers of different cavity length and (4) the assembly of active material and doped DBR mirrors into a VCSEL structure, which requires precise alignment of the peak wavelength of the gain spectrum relative to the cavity resonance. Although VCSEL epitaxy is commercially available, certain structures (i.e. active regions with high number of quantum wells) are not commercially available, while others require inhouse regrowth. Further, the high cost and long lead time of commercial epitaxy would severely limit the innovation cycle.

Wavelength tunable VCSELs with MEMS actuated high contrast grating (HCG) top reflector were then examined in chapter 3 under optical excitation and chapter 4 and 5 electrically pumped. These light sources are being developed for swept source optical coherence tomography (SS-OCT) a measurement technique with a growing field of application in medical imaging of eyes, skin and colon. Here (chapter 4) we demonstrated a VCSEL with HCG as sole top reflector achieving single mode emission over a continues tuning range of 56 nm at room temperature and continues wave operation. A corresponding device (chapter 5) with lithographically defined buried InGaP heterostructure as current confining aperture

showed excellent single mode emission with ~37 dB side mode suppression ratio for a large aperture size of 6 μm diameter.

In contrast to the native oxide confined current aperture, which is the state of the art in today's GaAs based VCSELs, lithographic apertures that utilize semiconductor material (chapter 5 and 6) have advantages in reliability and thermal conductance. Furthermore, the regrowth based lithographic aperture eliminates the need for mesas of individual VCSEL elements, which enables ultra-dense and highly uniform emitter arrays and potentially coherently coupled arrays. The weak optical confinement achievable with such apertures paves the road for large aperture, single mode devices with narrow divergence in the far field. The architecture of the fixed wavelength VCSEL in chapter 6 combines a lithographic aperture based on a tunnel junction with a high contrast grating (HCG) top mirror. Careful study of the tunnel junction parameters and the epitaxial regrowth conditions are crucial to the device performance. Both aspects where not exhaustively optimized in this work and are worth further efforts.

Finally, VCSEL arrays were fabricated from commercial epitaxy in chapter 7 and devices emitting at 850 nm and 940 nm wavelength were demonstrated. This type of device although subject of research for more than the last 20 years is currently experiencing a boom in demand as high volume consumer applications are adopting 3D sensing capabilities. In 3D sensing VCSEL arrays with hundreds of elements are used as illumination sources for structured light and time of flight measurements. Most important for the performance of arrays with a large quantity of emitters is their thermal design. High wall plug efficiency and low thermal resistance are necessary to limit the thermal power created in the device and to effectively remove it from the VCSEL. In this work single devices with up to 36.2 % and arrays with up to 22.6% wall plug efficiency were achieved. Further drop of the reflectivity of the top DBR has been found necessary to promote higher extraction efficiency and the doping profiles of both DBRs need optimization to lower the voltage of the devices. For the fabrication process improvements in yield and uniformity are most critical to narrow the gap in efficiency between the single emitter and the array with the goal to reach wall plug efficiencies above 40 %.

Beyond the above, incorporation of lithographically defined apertures with low electrical and thermal resistance as well as weak optical confinement seems promising to further improve performance metrics of VCSEL arrays.

9 References

[1] B. Tell, K. F. Brown-Goebeler, R. E. Leibenguth, F. M. Baez, and Y. H. Lee, "Temperature dependence of GaAs-AlGaAs vertical cavity surface emitting lasers," *Appl. Phys. Lett.*, vol. 60, no. 6, pp. 683–685, Feb. 1992.

[2] M. Agustin *et al.*, "50 Gb/s NRZ and 4-PAM data transmission over OM5 fiber in the SWDM wavelength range," in *Vertical-Cavity Surface-Emitting Lasers XXII*, 2018, vol. 10552, p. 1055202.

[3] D. D. John *et al.*, "Wideband electrically pumped 1050-nm MEMS-tunable VCSEL for ophthalmic imaging," *Journal of Lightwave Technology*, vol. 33, no. 16, pp. 3461–3468, 2015.

[4] V. Jayaraman *et al.*, "Room-temperature continuous-wave mid-infrared VCSEL operating at 3.35 μm," in *Vertical-Cavity Surface-Emitting Lasers XXII*, 2018, vol. 10552, p. 105520B.

[5] V. J. Kitsmiller, M. Dummer, K. Johnson, and T. D. O'Sullivan, "Tunable vertical cavity surface emitting lasers for use in the near infrared biological window," in *Optical Fibers and Sensors for Medical Diagnostics and Treatment Applications XVIII*, 2018, vol. 10488, p. 104880L.

[6] S. L. Chuang, *Physics of photonic devices*, vol. 80. John Wiley & Sons, 2012.

[7] S. Birner *et al.*, "nextnano: General Purpose 3-D Simulations," *IEEE Transactions on Electron Devices*, vol. 54, no. 9, pp. 2137–2142, Sep. 2007.

[8] A. R. Adams, "Strained-Layer Quantum-Well Lasers," *IEEE Journal of Selected Topics in Quantum Electronics*, vol. 17, no. 5, pp. 1364–1373, Sep. 2011.

[9] M. Kamp, "Halbleiterbauelemente - Bandstrukturen." .

[10] Y. P. Varshni, "Temperature dependence of the energy gap in semiconductors," *Physica*, vol. 34, no. 1, pp. 149–154, Jan. 1967.

[11] R. C. Miller, D. A. Kleinman, W. A. Nordland, and A. C. Gossard, "Luminescence studies of optically pumped quantum wells in GaAs-Al$_x$Ga$_{1-x}$As multilayer structures," *Phys. Rev. B*, vol. 22, no. 2, pp. 863–871, Jul. 1980.

[12] D. L. Rode and S. Knight, "Electron Transport in GaAs," *Phys. Rev. B*, vol. 3, no. 8, pp. 2534–2541, Apr. 1971.

[13] D. L. Rode, "Chapter 1 Low-Field Electron Transport," in *Semiconductors and Semimetals*, vol. 10, R. K. Willardson and A. C. Beer, Eds. Elsevier, 1975, pp. 1–89.

[14] Y.-M. Houng and T. S. Low, "Te doping of GaAs and AlxGa1- xAs using diethyltellurium in low pressure OMVPE," *Journal of Crystal Growth*, vol. 77, no. 1–3, pp. 272–280, 1986.

[15] L. A. Coldren, S. W. Corzine, and M. L. Mashanovitch, *Diode lasers and photonic integrated circuits*, vol. 218. John Wiley & Sons, 2012.

[16] W. T. Tsang, "A graded-index waveguide separate-confinement laser with very low threshold and a narrow Gaussian beam," *Applied Physics Letters*, vol. 39, no. 2, pp. 134–137, 1981.

[17] S. D. Hersee, M. Baldy, P. Assenat, B. de Cremoux, and J. P. Duchemin, "Very low threshold GRIN-SCH GaAs/GaAlAs laser structure grown by OM-VPE," *Electronics Letters*, vol. 18, no. 20, pp. 870–871, Sep. 1982.

[18]   S. Y. Hu, D. B. Young, S. W. Corzine, A. C. Gossard, and L. A. Coldren, "High-efficiency and low-threshold InGaAs/AlGaAs quantum-well lasers," *Journal of Applied Physics*, vol. 76, no. 6, pp. 3932–3934, Sep. 1994.

[19]   J. Wang, J. Kapraun, E. Kolev, J. Qi, K. T. Cook, and C. J. Chang-Hasnain, "Precise Two-step Growth of 940-nm VCSEL on a GaAsP-capped DBR Wafer," in *Conference on Lasers and Electro-Optics (2018), paper STu3Q.3*, 2018, p. STu3Q.3.

[20]   V. Jayaraman *et al.*, "Rapidly swept, ultra-widely-tunable 1060 nm MEMS-VCSELs," *Electronics letters*, vol. 48, no. 21, pp. 1331–1333, 2012.

[21]   V. Jayaraman, G. D. Cole, M. Robertson, A. Uddin, and A. Cable, "High-sweep-rate 1310 nm MEMS-VCSEL with 150 nm continuous tuning range," *Electronics letters*, vol. 48, no. 14, pp. 867–869, 2012.

[22]   C. J. Chang-Hasnain and W. Yang, "High-contrast gratings for integrated optoelectronics," *Advances in Optics and Photonics*, vol. 4, no. 3, pp. 379–440, 2012.

[23]   K. Li, C. Chase, P. Qiao, and C. J. Chang-Hasnain, "Widely tunable 1060-nm VCSEL with high-contrast grating mirror," *Opt. Express, OE*, vol. 25, no. 10, pp. 11844–11854, May 2017.

[24]   C. Chase, Y. Rao, W. Hofmann, and C. J. Chang-Hasnain, "1550 nm high contrast grating VCSEL," *Opt. Express, OE*, vol. 18, no. 15, pp. 15461–15466, Jul. 2010.

[25]   P. Qiao, K. T. Cook, K. Li, and C. J. Chang-Hasnain, "Wavelength-Swept VCSELs," *IEEE Journal of Selected Topics in Quantum Electronics*, vol. 23, no. 6, pp. 1–16, 2017.

[26]   M. S. Wu, E. C. Vail, G. S. Li, W. Yuen, and C. J. Chang-Hasnain, "Tunable micromachined vertical cavity surface emitting laser," *Electronics Letters*, vol. 31, no. 19, pp. 1671–1672, 1995.

[27]   G. M. Yang, M. H. Macdougal, V. Pudikov, and P. D. Dapkus, "Influence of mirror reflectivity on laser performance of very-low-threshold vertical-cavity surface-emitting lasers," *IEEE Photonics Technology Letters*, vol. 7, no. 11, pp. 1228–1230, 1995.

[28]   D. I. Babic and S. W. Corzine, "Analytic expressions for the reflection delay, penetration depth, and absorptance of quarter-wave dielectric mirrors," *IEEE Journal of Quantum Electronics*, vol. 28, no. 2, pp. 514–524, 1992.

[29]   C. Gierl *et al.*, "Surface micromachined tunable 1.55 μm-VCSEL with 102 nm continuous single-mode tuning," *Optics Express*, vol. 19, no. 18, pp. 17336–17343, 2011.

[30]   C. Gierl *et al.*, "Surface micromachined MEMS-tunable VCSELs with wide and fast wavelength tuning," *Electronics letters*, vol. 47, no. 22, pp. 1243–1244, 2011.

[31]   T. Ansb\a ek, I.-S. Chung, E. S. Semenova, and K. Yvind, "1060-nm tunable monolithic high index contrast subwavelength grating VCSEL," *IEEE Photonics Technology Letters*, vol. 25, no. 4, pp. 365–367, 2013.

[32]   T. Ansb\a ek, I.-S. Chung, E. S. Semenova, O. Hansen, and K. Yvind, "Resonant mems tunable vcsel," *IEEE Journal of Selected Topics in Quantum Electronics*, vol. 19, no. 4, pp. 1702306–1702306, 2013.

[33]   J. Kapraun *et al.*, "Air-Cavity Dominated HCG-VCSEL with a Wide Continuous Tuning," in *CLEO: Science and Innovations*, 2018, p. STu3Q–5.

[34]   N. Braslau, J. B. Gunn, and J. L. Staples, "Metal-semiconductor contacts for GaAs bulk effect devices," *Solid-State Electronics*, vol. 10, no. 5, pp. 381–383, May 1967.

[35]   A. N. Al-Omari, G. P. Carey, S. Hallstein, J. P. Watson, G. Dang, and K. L. Lear, "Low thermal resistance high-speed top-emitting 980-nm VCSELs," *IEEE Photonics Technology Letters*, vol. 18, no. 11, pp. 1225–1227, 2006.

[36]   B. Weigl *et al.*, "High-performance oxide-confined GaAs VCSELs," *IEEE Journal of Selected Topics in Quantum Electronics*, vol. 3, no. 2, pp. 409–415, 1997.

[37]   M. A. Afromowitz, "Thermal conductivity of Ga1- x Al x As alloys," *Journal of Applied Physics*, vol. 44, no. 3, pp. 1292–1294, 1973.

[38]   D. L. Huffaker, D. G. Deppe, K. Kumar, and T. J. Rogers, "Native-oxide defined ring contact for low threshold vertical-cavity lasers," *Applied Physics Letters*, vol. 65, no. 1, pp. 97–99, 1994.

[39]   U. Fiedler, G. Reiner, P. Schnitzer, and K. J. Ebeling, "Top surface-emitting vertical-cavity laser diodes for 10-Gb/s data transmission," *IEEE Photonics Technology Letters*, vol. 8, no. 6, pp. 746–748, 1996.

[40]   B. Weigl, M. Grabherr, R. Michalzik, G. Reiner, and K. J. Ebeling, "High-power single-mode selectively oxidized vertical-cavity surface-emitting lasers," *IEEE Photonics Technology Letters*, vol. 8, no. 8, pp. 971–973, 1996.

[41]   M. Grabherr, R. Jager, R. Michalzik, B. Weigl, G. Reiner, and K. J. Ebeling, "Efficient single-mode oxide-confined GaAs VCSEL's emitting in the 850-nm wavelength regime," *IEEE Photonics Technology Letters*, vol. 9, no. 10, pp. 1304–1306, 1997.

[42]   J. Ahn, D. Lu, and D. G. Deppe, "All-epitaxial, lithographically defined, current- and mode-confined vertical-cavity surface-emitting laser based on selective interfacial fermi-level pinning," *Appl. Phys. Lett.*, vol. 86, no. 2, p. 021106, Jan. 2005.

[43]   D. Lu, J. Ahn, H. Huang, and D. G. Deppe, "All-epitaxial mode-confined vertical-cavity surface-emitting laser," *Applied physics letters*, vol. 85, no. 12, pp. 2169–2171, 2004.

[44]   A. Demir, G. Zhao, and D. G. Deppe, "Lithographic lasers with low thermal resistance," *Electronics Letters*, vol. 46, no. 16, pp. 1147–1149, Aug. 2010.

[45]   M. S. Abrahams, R. Braunstein, and F. D. Rosi, "Thermal, electrical and optical properties of (In,Ga)as alloys," *Journal of Physics and Chemistry of Solids*, vol. 10, no. 2, pp. 204–210, Jul. 1959.

[46]   M. Le Du, D. Massoubre, J.-C. Harmand, and J.-L. Oudar, "Thermal conductance of laterally-wet-oxidised GaAs/AlxOy Bragg reflectors," *Electronics Letters*, vol. 42, no. 18, pp. 1060–1062, 2006.

[47]   J. Boucart *et al.*, "Metamorphic DBR and tunnel-junction injection. A CW RT monolithic long-wavelength VCSEL," *IEEE Journal of selected topics in quantum electronics*, vol. 5, no. 3, pp. 520–529, 1999.

[48]   M. Ortsiefer, R. Shau, G. Böhm, F. Köhler, and M.-C. Amann, "Low-threshold index-guided 1.5 μm long-wavelength vertical-cavity surface-emitting laser with high efficiency," *Appl. Phys. Lett.*, vol. 76, no. 16, pp. 2179–2181, Apr. 2000.

[49]   W. Hofmann *et al.*, "Long-Wavelength High-Contrast Grating Vertical-Cavity Surface-Emitting Laser," *IEEE Photonics Journal*, vol. 2, no. 3, pp. 415–422, Jun. 2010.

[50]   W. Hofmann *et al.*, "Long-wavelength BTJ-VCSEL with high-contrast grating," in *CLEO/QELS: 2010 Laser Science to Photonic Applications*, 2010, pp. 1–2.

[51]   K. T. Cook, J. Qi, J. Wang, N. Cabello, and C. J. Chang-Hasnain, "Novel Oxide Spacer High-Contrast Grating VCSELs," in *Conference on Lasers and Electro-Optics (2018), paper STu3Q.6*, 2018, p. STu3Q.6.

[52]   A. E. Bond, P. D. Dapkus, and J. D. O'brien, "Aperture placement effects in oxide-defined vertical-cavity surface-emitting lasers," *IEEE Photonics Technology Letters*, vol. 10, no. 10, pp. 1362–1364, 1998.

[53]   A. E. Bond, P. D. Dapkus, and J. D. O'Brien, "Aperture dependent loss analysis in vertical-cavity surface-emitting lasers," *IEEE Photonics Technology Letters*, vol. 11, no. 4, pp. 397–399, 1999.

[54]   H. Sodabanlu, K. Watanabe, M. Sugiyama, and Y. Nakano, "Effects of various dopants on properties of GaAs tunneling junctions and p–i–n solar cells," *Japanese Journal of Applied Physics*, vol. 56, no. 8S2, p. 08MC11, 2017.

[55]   D. Francis, H.- Chen, W. Yuen, G. Li, and C. Chang-Hasnain, "Monolithic 2D-VCSEL array with >2 W CW and >5 W pulsed output power," *Electronics Letters*, vol. 34, no. 22, pp. 2132–2133, Oct. 1998.

[56]   K. D. Choquette, H. Q. Hou, K. M. Geib, and B. E. Hammons, "Uniform and high power selectively oxidized 8x8 VCSEL array," in *1997 Digest of the IEEE/LEOS Summer Topical Meeting: Vertical-Cavity Lasers/Technologies for a Global Information Infrastructure/WDM Components Technology/Advanced Semiconductor Lasers and Application*, 1997, pp. 11–12.

[57]   T. Wipiejewski, M. G. Peters, B. J. Thibeault, D. B. Young, and L. A. Coldren, "Size-dependent output power saturation of vertical-cavity surface-emitting laser diodes," *IEEE Photonics Technology Letters*, vol. 8, no. 1, pp. 10–12, Jan. 1996.

[58]   J. M. Catchmark, L. E. Rogers, R. A. Morgan, M. T. Asom, G. D. Guth, and D. N. Christodoulides, "Optical characteristics of multitransverse-mode two-dimensional vertical-cavity top surface-emitting laser arrays," *IEEE Journal of Quantum Electronics*, vol. 32, no. 6, pp. 986–995, Jun. 1996.

[59]   Y. Ohiso, Y. Kohama, and T. Kurokawa, "Thermal interference in a 0.85 mu m 8*8 two-dimensional vertical-cavity surface-emitting laser array," *Electronics Letters*, vol. 30, no. 18, pp. 1491–1492, Sep. 1994.

[60]   W. Nakwaski and M. Osinski, "Thermal resistance of top-surface-emitting vertical-cavity semiconductor lasers and monolithic two-dimensional arrays," *Electronics Letters*, vol. 28, no. 6, pp. 572–574, 1992.

[61]   T. Wipiejewski, D. B. Young, B. J. Thibeault, and L. A. Coldren, "Thermal crosstalk in 4 x 4 vertical-cavity surface-emitting laser arrays," *IEEE Photonics Technology Letters*, vol. 8, no. 8, pp. 980–982, 1996.

[62]   S. Adachi, "AlAs, and Al (x) Ga (1-x) As: Material parameters for use in research and device applications‖ Journal of Applied Physics, vol. 58, pp," *R1-R29*, 1985.

[63]   S. Adachi, *Properties of aluminium gallium arsenide*. IET, 1993.

[64]   J. Piprek, T. Troger, B. Schroter, J. Kolodzey, and C. S. Ih, "Thermal conductivity reduction in GaAs-AlAs distributed Bragg reflectors," *IEEE Photonics Technology Letters*, vol. 10, no. 1, pp. 81–83, 1998.

[65]   T. Yao, "Thermal properties of AlAs/GaAs superlattices," *Applied Physics Letters*, vol. 51, no. 22, pp. 1798–1800, 1987.

[66]   X. Y. Yu, G. Chen, A. Verma, and J. S. Smith, "Temperature dependence of thermophysical properties of GaAs/AlAs periodic structure," *Applied Physics Letters*, vol. 67, no. 24, pp. 3554–3556, 1995.

[67]   R. F. Nabiev and C. J. Chang-Hasnain, "Voltage drop in n-and p-type Bragg reflectors for vertical-cavity surface-emitting lasers," *IEEE photonics technology letters*, vol. 7, no. 7, pp. 733–735, 1995.

[68]   M. Murakami, K. D. Childs, J. M. Baker, and A. Callegari, "Microstructure studies of AuNiGe Ohmic contacts to n-type GaAs," *Journal of Vacuum Science & Technology B: Microelectronics Processing and Phenomena*, vol. 4, no. 4, pp. 903–911, Jul. 1986.

[69]   Y. Shih, M. Murakami, E. L. Wilkie, and A. C. Callegari, "Effects of interfacial microstructure on uniformity and thermal stability of AuNiGe ohmic contact to n-type GaAs," *Journal of Applied Physics*, vol. 62, no. 2, pp. 582–590, Jul. 1987.